

Dissertation

Study of atomic structure and catalytic property of

Ni_2P and related surfaces

by photoelectron diffraction spectroscopy

Hirosuke Matsui

March , 2014

Graduate School of Materials Science

Nara Institute of Science and Technology

Contents

Chapter 1. General Introduction	1
1.1 Background	1
1.1.1 Graphene	2
1.1.2 Ni ₂ P catalyst for hydrodesulfurization reaction	4
1.2 Details of atomic level characterization method	6
1.2.1 Photoelectron diffraction	6
1.2.2 Display-type spherical mirror analyzer	13
1.3 Purpose of this dissertation	20
Chapter 2. Local atomic configuration of graphene, buffer layer and precursor layer on SiC(0001) by photoelectron holography	29
2.1 Introduction	30
2.2 Experimental details	33
2.3 Results and discussion	35
2.4 Conclusion	53
Chapter 3. Disentanglement of site selective X-ray absorption spectra of catalytic Ni₂P surface by photoelectron diffraction spectroscopy	62
3.1 Introduction	63
3.2 Experimental details	65
3.3 Results and discussion	67
3.4 Conclusion	79

Chapter 4. Surface atomic structure and catalytic property of Fe modified	
Ni₂P surface by photoelectron diffraction	84
4.1 Introduction	85
4.2 Experimental details	87
4.3 Results and discussion	89
4.4 Conclusion	97
Chapter 5. Atomic structure and catalytic activity of W-Ni₂P surface alloy	
by photoelectron diffraction and spectroscopy	101
5.1 Introduction	102
5.2 Experimental details	104
5.3 Results and discussion	106
5.4 Conclusion	114
Chapter 6. Atomic structure analysis of catalytic poly-crystalline Ni₂P sur-	
face by microscopic photoelectron diffraction	121
6.1 Introduction	122
6.2 Experimental details	126
6.3 Results and discussion	128
6.4 Conclusion	135
Chapter 7. Summary	140
Accomplishments	143
1 Papers	143

2 Honors and Awards 145

Acknowledgements 147

Chapter 1. General Introduction

1.1 Background

Catalysts are indispensable for the chemical industry. The discovery of for new catalyst are a foundation of the new chemical industry. Catalysts are used not only for the efficient synthetic purposes but also for the reduction of harmful by-products which causes environmental pollution. The importance of catalyst is increasing.

Atomic level catalyst characterization reveals the catalytic mechanisms and clarifies how the molecules activate and react to the catalyst. This knowledge is the basis of the development of new catalytic materials and improving the catalytic properties. Understanding the active structure on the surface and its local electronic state is the key for realizing the ideal catalyst which greatly contributes to environmental and economic problems. However, analysis methods for acquiring the localized surface and interface structures, which relate to the physical and chemical properties, are not established.

In this dissertation, I will demonstrate the applied usage of photoelectron diffraction, spectroscopy and X-ray absorption spectroscopy using our originally developed analysis method for catalyst characterization. Among the materials, I have studied two state-of-the-art materials expected to become next generation devices and catalysts, graphene and Ni_2P , because the fundamental physical and chemical properties of these materials are not known. As a result, I achieved new findings in five topics through my Ph.D study.

1.1.1 Graphene

A. K. Geim and K. Novoselov of University of Manchester succeeded in the isolation of monolayer graphite by exfoliating crystalline graphite using Scotch tapes in 2004, and won the Nobel prize in 2010 within several years of the discovery. The existence of monolayer graphite had been predicted and named as “graphene”, which is a combination of graphite and the suffix “-ene”. Graphene has been attracting much interest (44,000 hits when searching the word, “graphene” in THOMSON REUTERS, “web of knowledge” as of December 18, 2013) because of its distinctive band structure, Dirac cone and physical properties. Recently, the usage of graphene is expected as a substrate for catalysts by supporting metal nano-particle. The investigation of the surface and interface structures, which have distinctive physical properties, are crucial areas.

The size of exfoliated graphene is limited to small sizes of less than $1000 \mu m^2$, because the films are produced mostly by exfoliating graphite, which is not scalable technique. However, the electron mobility shows the highest value as more than $150,000 \text{ cm}^2/\text{Vs}$. Graphene has also been synthesized by a surface precipitation process of carbon in some transition metals such as Cu and Ni. However, the mobility remains at only $4,000 \text{ cm}^2/\text{Vs}$. The most preferential method in industrial processes is heat decomposition of SiC substrate under low pressure. The desorption of Si from SiC surface produces epitaxial-graphene with dimensions dependent upon the wafer size. The termination of the SiC surface, Si- or C-faces, and the interaction with the interface structure highly influenced the physical properties, electron mobility and growing process at earlier stages. However, the subsurface atomic structure is still controversial.

Photoelectron from a localized core-level is an excellent element-selective probe for surface structure analysis. In this dissertation, I have characterized each stage of thermal graphitization of the 4H-SiC(0001) substrate by photoelectron diffraction.

1.1.2 Ni₂P catalyst for hydrodesulfurization reaction

The development of new catalysts plays an important role in the discovery and improvement of processes for the conversion of energy, the production of chemicals and the elimination of harmful materials from industrial products. In the past decades, there have been great advances in the areas of automotive emission control, fine chemical production, syn-gas conversion and oxidative transformations, thanks to the development of new catalysts [1, 2].

One of the most considerable advances in the last 10 years of catalyst development is hydroprocessing. This reaction has been the result of stricter global environmental laws for the allowed sulfur content in petroleum feedstock. The catalysts help to decrease the exhausting of sulfide and nitrogen oxides, which are the reasons for acid rainfall and atmosphere pollution [3, 4]. These trends have led to worldwide research along the development of better catalysts for hydrodesulfurization (HDS) and hydrodenitrogenation (HDN) reactions [5]. Figure 1.1 shows the typical HDS reaction of thiophene, (C₄H₄)-S. These sulfides are separated into

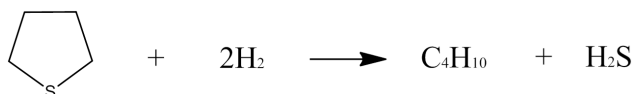


Fig. 1.1. The scheme of typical hydrodesulfurization reaction of thiophene.

carbon hydride and H₂S in the petroleum processing. However, this process is heavy burden for efficient industrial production because enormous amounts of catalysts and time are necessary. Hence, a new series of catalysts, which will solve economic and environmental problems, are necessary.

Current approaches include the improvement of conventional sulfide catalysts such as Ni-MoS and CoMoS and the investigation of new compounds such as bimetallic carbides [6],

nitride [7], and noble metals such as Pt and Pd [8]. These studies report on a novel class of catalyst materials which promise to be the next generation of catalysts. The materials are transitional metal phosphides (TMPs), a group of stable, sulfur-resistant, metallic compounds that have a remarkable hydroprocessing properties. Recent studies have revealed that MoP [9–12], WP [13], Ni₂P and Co₂P [14–16] are highly active for HDS and HDN of petroleum feedstocks. Among the TM phosphides studied so far, Ni₂P has been found to have outstanding performance in simultaneous HDN and HDS with higher activity than existing promoted sulfides [17]. As a prelude to future investigations of the chemical properties of model Ni₂P surfaces, characterization studies using single-crystalline Ni₂P surfaces must be undertaken.

1.2 Details of atomic level characterization method

1.2.1 Photoelectron diffraction

A knowledge of the atomic identities, positions, and bonding mechanisms within several layers of the surface, which plays a fundamental role in the understanding of surface properties for catalyst and device usages, has been essential so far. This implies knowing the atomic arrangements, including bond directions, bond distances, site symmetries, coordination numbers, and the degree of both short-range and long-range periodicity present in the surface terminated region. A number of surface structure analyses have been developed and conducted in recent years in an attempt to provide this information. Each of these methods has certain unique advantages and disadvantages, and they are often complementary to one another.

When the light is incident into the material, photoelectron is emitted from the surface under the vacuum atmosphere. By analyzing the kinetic and photon energies of the photoelectron, photoelectron spectroscopy (PES) spectra are obtained. In the one electron approximation, PES spectra are considered as the density of states. Therefore, one can obtain the surface chemical state and its reactivity from the PES spectra. According to the energy conservation theorem, the photon energy $h\nu$, the binding E_B and the kinetic E_k energies of the photoelectron are defined as the following,

$$h\nu = E_k + E_B + \Phi \tag{1}$$

where Φ indicates the work function of the analyzer. In this thesis, this model was used for

understanding the process of PES.

Photoelectron diffraction (PED) is a local atomic structure analysis method which involves exciting a core-hole photoelectron from an atom in a single-crystalline environment and then observing modulations in the resulting peak intensities that are due to final-state scattering from the scatterer atoms neighboring the emitter atom. The photoelectron direct wave Ψ_0 exhibits interference from various scatterer waves Ψ_s , and this interference pattern, photoelectron intensity angular distribution (PIAD), is analyzed to derive structural information. As shown in the schematic diagram of photoelectron diffraction (Fig. 1.2), the higher-order diffraction rings (DRs) appear around the 0th diffraction, the forward focusing peak (FFP). The phenomena of photoelectron diffraction $|I(\theta, \phi)|^2$ is described as,

$$|I(\theta, \phi)|^2 = |\Psi_0 + \Psi_s|^2 = |\Psi_0|^2 + |\Psi_0^* \Psi_s + \Psi_s^* \Psi_0| + |\Psi_s|^2 \quad (2)$$

where FFP and DR components are explained as $|\Psi_s|^2 + |\Psi_0^* \Psi_s + \Psi_s^* \Psi_0|$ and $|\Psi_0^* \Psi_s + \Psi_s^* \Psi_0|$, respectively. The opening angle θ of DR has the relation with the interatomic distance shown with the following equation,

$$kR(1 - \cos \theta_n) = 2\pi n + \Delta, \quad n = 1, 2, 3, \dots \quad (3)$$

where k , R and Δ are the wave number, the interatomic distance and the phase shift effect which was scattered by the atom. Thus the direction and distance of the surrounding atoms seen from the emitter atom can be directly deduced from the direction of FFP and the opening angle of DR, respectively. The advantages of PED is the element specific probe of short-range

by the selective detection of photoelectrons with the corresponding binding energy. Each type of local structures in a sample can be studied, and they have unique diffraction signatures associated with the neighboring atoms around it.

The first observations of strong diffraction effects in X-ray photoelectron emission from single-crystal substrates were achieved by Siegbahn *et al.* [18] and by C. Fadley and S. A. L. Bergstorm [19] in the 1970s using hard X-ray energies. The use of such effects at lower energies to determine surface structures was predicted by Liebsch. [20, 21] The quantitative experimental surface structure studies were initiated by Kono *et al.* [22, 23] Woodruff *et al.* [24], and Kevan *et al.* [25] in the late 1970s. The appearance of synchrotron radiation added the capability of varying the photon energy continuously and of studying the dependence of the diffraction on polarization in the 1980s [26]. The application of the various data acquisition modes to well-defined systems as well as to more complex overlayered structures is demonstrated. In particular, the potential of PED in structural determination of molecular adsorbate and multi-site overlayer systems[27] is emphasized. Thus, Nihei *et al* insisted that PIAD can be used in a “fingerprint” manner, when preferential substitution or adsorption of atoms occur. In the late 1980s, the first PED observation of Pt nano-particles on a single-crystalline TiO₂ substrate as a model catalyst was reported, and the structural model of Pt nano-particles based on the (111) surface of the face-centered cubic (fcc) crystal was clarified[28, 29]. PED has been becoming more widely used to study surface atomic geometries (2,035 hits when searching the word, “photoelectron diffraction” in THOMSON REUTERS, “web of knowledge” as of January 8, 2014).

The progress in our laboratory has been playing an important role in the study of PED. In 1993, Daimon *et al.* firstly observed the strong circular dichroism of photoelectron by

the circularly-polarized light excitation [30]. The FFP in the PIAD rotate clockwise and counterclockwise when the helicity of incident light is reversed. They also clarified the relation between the azimuthal rotational shift of FFP $\Delta\phi$ and the interatomic distance R [30, 31],

$$\Delta\phi = \tan^{-1} \frac{m}{kR \sin^2 \theta}. \quad (4)$$

This is the equation that shows the direction of the FFP for the photoelectron with an angular momentum m . This phenomenon is helpful to measure a three-dimensional surface structure directly because this pattern tells us the bond length as well as the direction through the FFP. As the actual example of application, Kato *et al.* clarified the B-dopant site in a superconductive diamond by PED [32]. This achievement insisted that PED has a possibility for applying to the diluted materials less than several percentages. Matsui *et al.* developed new analysis method “*diffraction spectroscopy*” for detecting the electronic structure which directly relates with the local site or surface structure [33]. This method insists that PED can also be applied the catalyst, magnetic and device related materials for the layer-resolved and site-selective electronic structure analysis. In this dissertation, I applied photoelectron diffraction spectroscopy method for catalyst characterization to observe the catalytic properties at the local atomic sites.

Theoretical calculations have been helpful in the interpretation of PIAD [23, 34]. To date, several kinds of simulation packages, such as “*Multiple Scattering Calculation of Diffraction (MSCD)*”, “*Electron Diffraction in Atomic Clusters (EDAC)*” [35], “*Yet Another Single sCattering program (YASC)*”, and *TMSP* [36–38] have been developed but their usage is complementary to each other. In this study, *TMSP* was used because this program has

higher accuracy than the others. Complex calculations including polarization dependency and infinite multiple-scattering are available. Figure 1.3 illustrates the kinetic energy dependence of the relevant elastic-scattering factors for the case of Ni-Ni bonding of 2.58\AA with curves of the plane-wave scattering amplitude $|I(\theta, \phi)|^2$ as a scattering polar angle θ and the kinetic energy of 50, 80, 90, 100, 600, and 1000 eV. The calculation was performed using the multiple scattering pattern code, *TMSP* developed by Dr. Matsushita [36–38]. For low energies below 100 eV, it is clear that there is high amplitude for scattering into all angles. For the intermediate energy at 600 eV, it is a reasonable approximation to only think of FFP at $\theta = 0^\circ$. However, at the highest energy, 1000 eV, the scattering amplitude is significant only in the forward direction, in which it is strongly peaked. The relation between the degree of FFP and kinetic energy was successfully reconstructed.

A three-dimensional atomic image reconstruction algorithm from electron holography based on Fourier transformation was proposed by Barton [39]. Atomic image reconstructions using an experimental electron hologram were also developed [40, 41]. However, Barton’s algorithm causes an atomic position shift because it ignores the strong phase shift effect [42] and forward focusing effect by electron scattering. I used the scattering pattern extraction algorithm using maximum entropy method (SPEA-MEM), which was not based on Fourier transform [36–38, 43, 44]. This algorithm used the scattering pattern function as a basis function and the maximum entropy method for the fitting procedure.

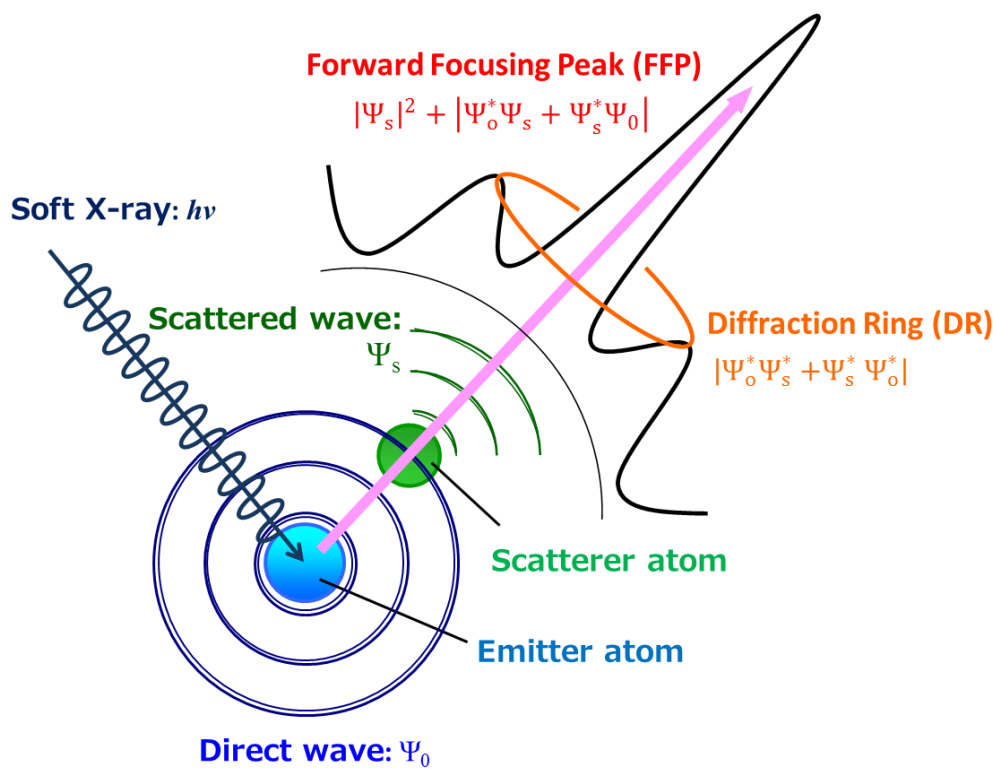


Fig. 1.2. The schematic diagram of photoelectron diffraction.

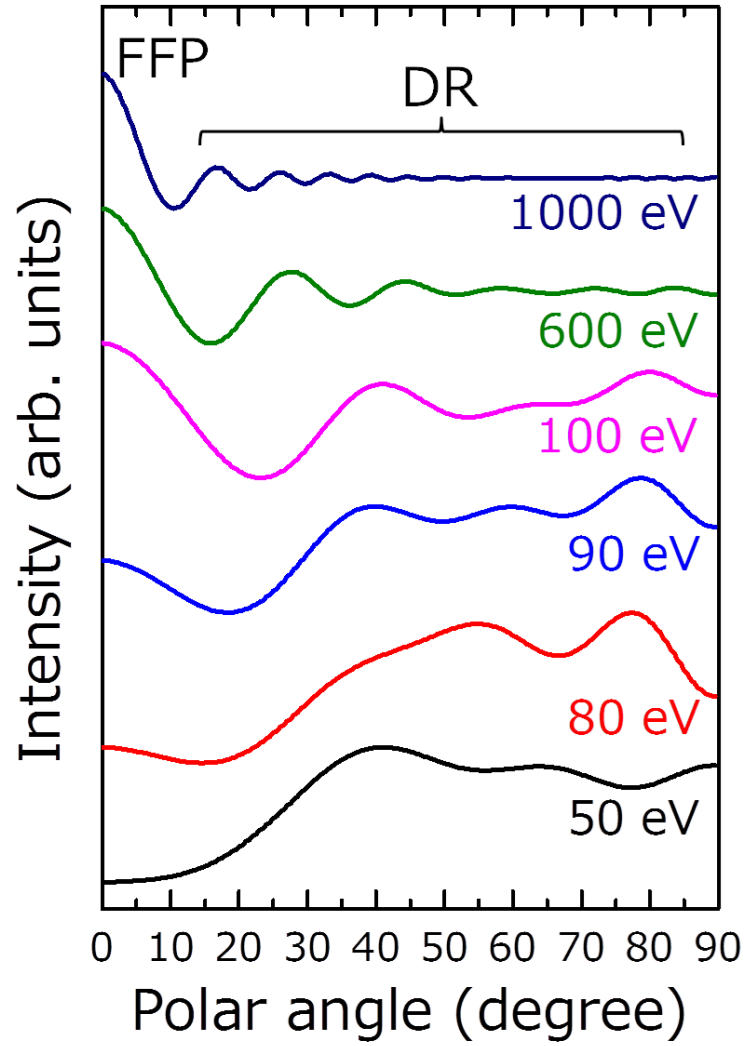


Fig. 1.3. Simulated polar angle dependence of scattering cross section for forward focusing peak (FFP) and diffraction ring (DR) excited at several kinetic energies by *TMSP*.

1.2.2 Display-type spherical mirror analyzer

Since establishing several kinds of spectroscopic analysis in solid surface physics, electron analyzers have been playing an important role. In fact, development of equipment directly relates to the progress of this area of study. There are three types of electron analyzers in general use for detecting solid angles, with each approach having its own set of advantages and disadvantages. The angle resolved type detects only a narrow range and measures the emission angle dependence. The angle integral type detects of a very wide range at one time and measures the density of electronic states. The two-dimensional display type measures the angular distribution of a very wide range at one time using a two-dimensional detector. Angle resolved and integral types most commonly use a concentric hemispherical analyzer (CHA) and cylindrical mirror analyzer (CMA), respectively. They achieve an efficient bright signal detection because double focusing of photoelectrons emitted from a wide area is realized.

The cylindrical mirror analyzer (CMA) has served as the analytical foundation for the majority of operation Auger electron spectrometers since its analytical utility was first described by Palmberg *et al.* in the last 1960s [45]. The CMA is used when it is not important that the highest resolution be achieved and when the highest throughput is desired. For example, CMA is routinely used if chemical state information is not required. The CMA design, with its compact size, high sensitivity, energy resolution better than $\Delta E/E=0.1\%$ [46], wide acceptance angle of 0.5π steradian [47], and convenient working distance, is advantageous as a standard Auger electron spectroscopy analyzer. However, it is not a suitable application for PED because CMA is not good for angle-resolved analysis.

The concentric hemispherical analyzer (CHA) is currently the most popular electron en-

ergy analyzer for electron spectroscopy. The analyzer consists of two concentric hemispheres capable of resolving the electron's energy momentum simultaneously. The CHA has a much better inherent energy resolution than any of the other analyzer designs. This can be an advantage for angle-resolved photoelectron spectroscopy measurements. The acceptance angle of the previous CHA was only $\pm 1^\circ$ (solid angle is 0.0003π steradian) to improve the angular resolution. However, the state-of-art CHA analyzer, R4000 Wide Angle Lens (WAL) produced by VG SCIENTA, improved the analytical efficiency such as a wider acceptance angle of $\pm 15^\circ$, the best angular resolution of 0.1° , and a convenient working distance of 34 mm [48]. PHOIBOS 150 WAL manufactured by SPECS also has cutting edge performance with a wide acceptance angle of 60° , fine angular resolution of 0.5° , and a convenient working distance of 27.75 mm [49]. The PED measurements consume a lot of time because the distribution is measured step-wise for each azimuthal θ and polar ϕ angle. In the PED measurement, a high angular resolution and wide acceptance angle are desired.

A display-type analyzer was first invented by Eastman *et al.* in 1980 [50], and the PIAD of a interest kinetic energy became visible with wide acceptance angle of $\pm 45^\circ$ (0.6π steradian) at the same time. The analyzer consists of an ellipsoidal grid, ellipsoidal mirror, and six spherical grids. In spite of its importance, the system is not popular at present because the its ellipsoidal structure is hard to construct. A computer-aided conversion process is necessary because the obtained PIAD is distorted.

In 1988, PIAD was efficiently measured by display-type spherical mirror analyzer (DIANA) which was invented by Daimon [51–53]. DIANA has several advantages for obtaining PIAD which improved on Eastman type. One important is that the angle of emission and detection of photoelectrons is exactly parallel, and PIAD is not distorted. Another is that

the acceptance angle is very wide. Hence, the PIAD obtained using DIANA can be analyzed directly without any computer-aided conversion processes. Figure 1.4 shows the schematic view of DIANA. It consists of a hemispherical grid (G), obstacle rings (Ob) and guard ring (Gd). The electronic field inside the electrodes G, Ob and Gd is spherically symmetric with respect to the center of the analyzer. The guard rings are used to correct possible fringe field. The orbit of the emitted electrons from the sample are subjected to this field after passing through G and converge exactly to the exit aperture (A) with keeping emission angle from the sample surface. A is located at the symmetric position of the sample with respect to the center of analyzer. Ob acts an essential role to cut unnecessary electrons which has higher kinetic energy than pass energy. An electron having a little outside locus and hit into the electrodes and absorbed or scattered and hardly passes A. Thus the Ob works as “low-pass filter”. On the other hand, retarding grid (R) works as a “high-pass filter” which retards the electrons having lower kinetic energies than the applied potential. The electrons passed through A and R are amplified by a pair of microchannel plates (MCPs) and converted by the fluorescent screen to the light pulses which can be detected by a CCD camera (Sensi cam-QE made by PCO imaging). Thus, the two-dimensional distribution without any distortion. The acceptance cone of the analyzer can cover the angular spread up to $\pm 80^\circ$, but the region covered by a MCP is limited to about $\pm 60^\circ$.

The performance of first version DIANA was not satisfactory with respect to the energy resolution and angular resolution to execute a highly accurate measurement. Therefore, the advanced DIANA [53] was constructed at a very high resolution soft x-ray beamline, BL25SU of SPring-8, Japan [54] in 2001. The size of the analyzer was twice enlarged from 150 mm of the radius of previous analyzer to 300 mm. Number of Ob rings were increased from 26 to

260, and the shaping accuracy was intended to be within $50 \mu\text{mm}$ because the radii of Ob is very sensitive to the energy resolution. The performance of present DIANA is that energy resolution, angle resolution and the acceptance angle of DIANA are 0.3%, $\pm 0.5^\circ$ and $\pm 60^\circ$, respectively.

The BL25SU of SPring-8 [54] supplies completely right or left circularly-polarized light on a common axis of a twin helical undulator to achieve the atomic stereography experiment [55]. A monochromator with varied-line-spacing plane grating is installed to cover the region below 1.5 keV. I used the Au-coating SiC-made grating with 300 slits by holographic processing to obtain the higher intensity than the others. A helicity modulation up to 10 Hz can be performed using kicker magnets. I used 0.1 Hz modulation because the several seconds of acquisition time is necessary for PED experiment.

These state of art facilities such as DIANA and circularly polarized soft X-ray are helpful for studying the PES experiment. I concentrated on the experiment and analysis.

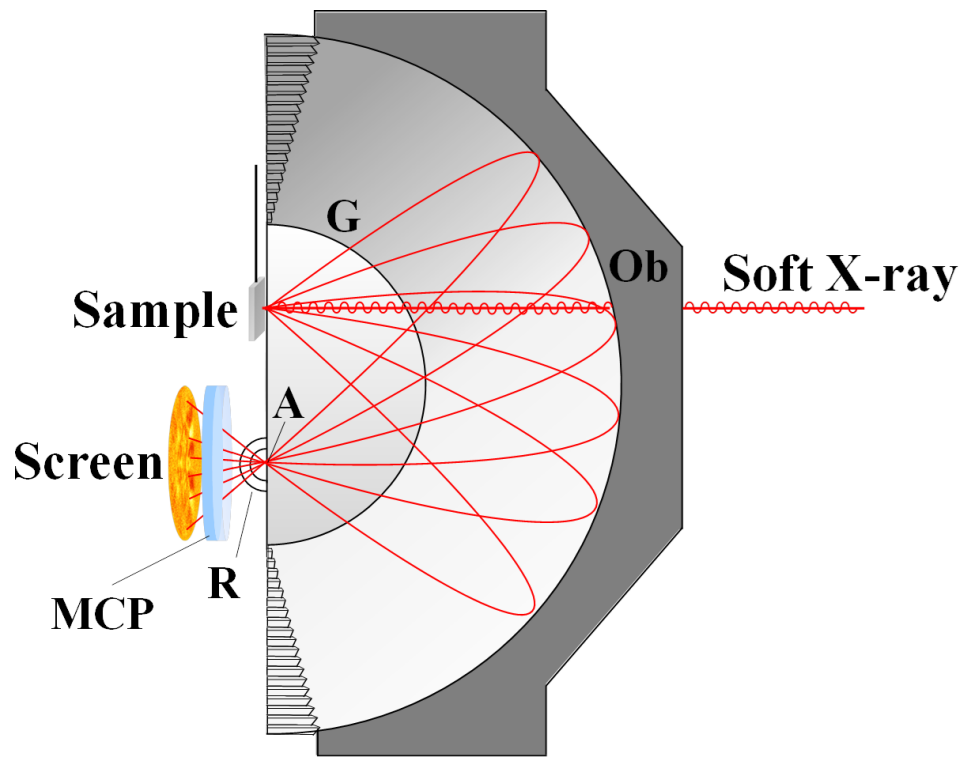


Fig. 1.4. The schematic diagram of display-type spherical mirror analyzer (DIANA). G, Ob, A, R and MCP indicate the hemispherical grid, obstacle rings, aperture and micro-channel-plate, respectively.

A two-dimensional photoelectron spectroscopy (2D-PES) station is shown in Fig. 1.5. A 2D-PES station is composed of three kinds of vacuum chambers for measurement, sample preparation, and load lock. Measurement and sample preparation chambers maintain an ultra-high vacuum condition of less than 3×10^{-8} Pa by using a turbo molecular pump (TMP), a dry pump (DP), an ion pump (IP) and a titan sublimation pump (TSP). The airlock chamber is evacuated by TMP and DP, and attached with differential pumping line to the main manipulator. The vacuum degree is evaluated using a nude ion gauge (NIG). The preparation chamber is equipped with two kinds of manipulators which are facing each other, a film thickness monitor, a RHEED system including electron gun and fluorescent screen, an evaporator, an ion gun for sputtering, and a gas line. Manipulators, equipped with our laboratory-made sample receptor, utilizes a set of current injection and K-type thermocoupling lines. Hence, fine controlled sample preparation including annealing and depositing are available.

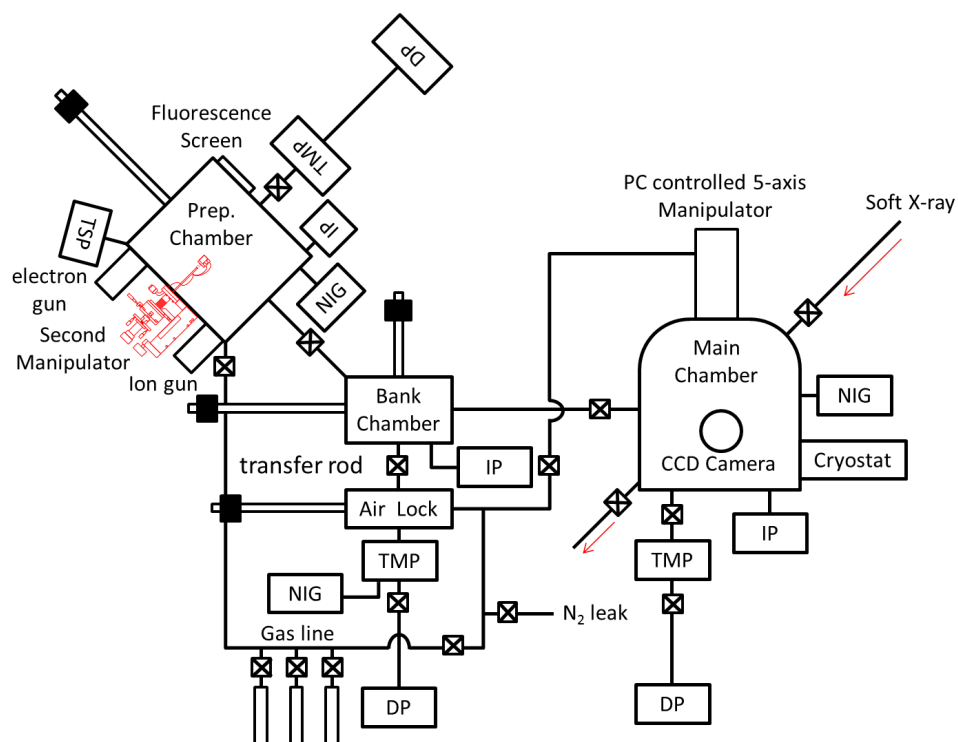


Fig. 1.5. The schematic diagram of a two-dimensional photoelectron spectroscopy (2D-PES) station. TMP, DP, IP, TSP, NIG indicate turbo molecular pump, dry pump titan sublimation pump and nude ion gauge, respectively.

1.3 Purpose of this dissertation

Photoelectron diffraction is an ideal technique for characterizing the surface structure with element and site selectivity. A number of catalyst surface structure analyses dependant on photoelectron diffraction has been reported but its usage has been limited for only structure analysis. Recently, our applied photoelectron diffraction, such as photoelectron holography and diffraction spectroscopy techniques, succeeded in analyzing the layer-resolved atomic structure analysis [56] and clarifying the relation between atomic and electronic structures [33]. Hence, the development of catalyst analysis dependant on photoelectron diffraction and a related technique using practical materials has the possibility to clarify the relation between the surface structure and catalytic properties.

This dissertation is composed of five chapters including the demonstration of photoelectron diffraction ability for catalyst characterization and application for newly developed surface phases which strongly relates to real catalyst studies. In chapter 1, I will demonstrate the effective photoelectron diffraction through layer-resolved atomic and electronic structure analysis at each stage of graphene formation on a SiC(0001) surface. Furthermore, new analytical routine for clarifying the relation between atomic and electronic structures will develop through the disentanglement of site specific X-ray absorption spectroscopy for a Ni₂P surface in chapter 2. Chapter 3 and 4 will be the applied usage for studying the surface structure and catalytic properties parallel to state-of-the-art research in real catalyst development through alloying. Finally, chapter 5 will reveal the future usage of photoelectron diffraction as a major catalyst characterization through the study of poly-crystalline surfaces which duplicated the real catalyst surface and the catalytic property at each crystal grain.

Green Sustainable Chemistry

Energy saving, Efficient use of resources, Removal of pollutants

Efficient reaction

- Reveal the catalyst and reaction mechanism
- Improve its catalytic activity

Discovery of new materials

- Graphene
- Ni₂P

Atomic level characterization is a key!

- Local structure
- Local electronic state

Surface sensitive
Local site selective
Element selective

Photoelectron diffraction has an ideal condition for catalyst characterization.

- New original analysis method
- Holography
 - Diffraction spectroscopy

Chapter 2,3

Applied usage of photoelectron diffraction for state-of-the-art catalyst characterization

Surface alloying

Chapter 4,5

Future usage of photoelectron diffraction

Polycrystalline surface

Chapter 6

Fig. 1.6. Flow chart of this dissertation. The purpose and the relation among each chapter are shown.

References

- [1] M. E. Davis. Ordered porous materials for emerging applications. *Nature* **417** (2002) 813–821.
- [2] A. König, G. Herding, B. Hupfeld, T. Richter and K. Weidmann. Current tasks and challenges for exhaust aftertreatment research. A viewpoint from the automotive industry. *Top. Catal.* **16** (2001) 23–31.
- [3] P. Greening. European vehicle emission legislation present and future. *Top. Catal.* **16** (2001) 5–13.
- [4] B. I. Bertelsen. Future US motor vehicle emission standards and the role of advanced emission control technology in meeting those standards. *Top. Catal.* **16** (2001) 15–22.
- [5] K. G. Knudsen, B. H. Cooper and H. Topsøe. Catalyst and process technologies for ultra low sulfur diesel. *Appl. Catal. A Gen.* **189** (1999) 205–215.
- [6] S. T. Oyama, C. Charles Yu and S. Ramanathan. Transition metal bimetallic oxycarbides: synthesis, characterization, and activity studies. *J. Catal.* **184** (1999) 535–549.
- [7] C. C. Yu, S. Ramanathan and S. T. Oyama. New Catalysts for Hydroprocessing: Bimetallic Oxynitrides M_I - M_{II} -O-N (M_I , M_{II} = Mo, W, V, Nb, Cr, Mn, and Co): Part i. Synthesis and Characterization. *J. Catal.* **173** (1998) 1–9.
- [8] Y. Yoshimura, H. Yasuda, T. Sato, N. Kijima and T. Kameoka. Sulfur-tolerant Pd-Pt/Yb-USY zeolite catalysts used to reformulate diesel oils. *Appl. Catal. A Gen.* **207** (2001) 303–307.

- [9] C. Stinner, R. Prins and T. Weber. Formation, structure, and HDN activity of unsupported molybdenum phosphide. *J. Catal.* **191** (2000) 438–444.
- [10] C. Stinner, R. Prins and T. Weber. Binary and ternary transition-metal phosphides as HDN catalysts. *J. Catal.* **202** (2001) 187–194.
- [11] D. C. Phillips, S. J. Sawhill, R. Self and M. E. Bussell. Synthesis, characterization, and hydrodesulfurization properties of silica-supported molybdenum phosphide catalysts. *J. Catal.* **207** (2002) 266–273.
- [12] P. Clark, X. Wang and S. T. Oyama. Characterization of Silica-Supported Molybdenum and Tungsten Phosphide Hydroprocessing Catalysts by ^{31}P Nuclear Magnetic Resonance Spectroscopy. *J. Catal.* **207** (2002) 256–265.
- [13] P. Clark, W. Li and S. T. Oyama. Synthesis and activity of a new catalyst for hydroprocessing: tungsten phosphide. *J. Catal.* **200** (2001) 140–147.
- [14] W. Robinson, J. Van Gestel, T. Korányi, S. Eijsbouts, A. V. d. Kraan, J. Van Veen and V. De Beer. Phosphorus promotion of Ni(Co)-containing Mo-free catalysts in quinoline hydrodenitrogenation. *J. Catal.* **161** (1996) 539–550.
- [15] X. Wang, P. Clark and S. T. Oyama. Synthesis, characterization, and hydrotreating activity of several iron group transition metal phosphides. *J. Catal.* **208** (2002) 321–331.
- [16] Y. Fukui and M. Murata. Living polymerizations of propylene and syntheses of atactic polypropylene-*block*-poly(ethylene-*co*-propylene) using metallocene catalyst systems. *Appl. Catal. A Gen.* **237** (2002) 1–10.

- [17] S. T. Oyama. Novel catalysts for advanced hydroprocessing: transition metal phosphides. *J. Catal.* **216** (2003) 343–352.
- [18] K. Siegbahn, U. Gelius, H. Siegbahn and E. Olson. Angular distribution of electrons in ESCA spectra from a single crystal. *Phys. Lett. A* **32** (1970) 221.
- [19] C. S. Fadley and A. L. Bergstrom. Angular distribution of photoelectrons from a metal single crystal. *Phys. Lett. A* **35** (1971) 375.
- [20] A. Liebsch. Theory of angular resolved photoemission from adsorbates. *Phys. Rev. Lett.* **32** (1974) 1203–1206.
- [21] A. Liebsch. Theory of photoemission from localized adsorbate levels. *Phys. Rev. B* **13** (1976) 544.
- [22] S. Kono, C. Fadley, N. Hall and Z. Hussain. Azimuthal anisotropy in deep core-level x-ray photoemission from an adsorbed atom: oxygen on copper (001). *Phys. Rev. Lett.* **41** (1978) 117.
- [23] S. Kono, S. Goldberg, N. Hall and C. Fadley. Azimuthal Anisotropy in Core-Level X-Ray Photoemission from $c(2 \times 2)$ Oxygen on Cu (001): Experiment and Single-Scattering Theory. *Phys. Rev. Lett.* **41** (1978) 1831.
- [24] D. Woodruff, D. Norman, B. Holland, N. Smith, H. Farrell and M. Traum. Diffraction of Photoelectrons Emitted from Core Levels of Te and Na Atoms Adsorbed on Ni (001). *Phys. Rev. Lett.* **41** (1978) 1130–1133.
- [25] S. Kevan, D. Rosenblatt, D. Denley, B.-C. Lu and D. Shirley. Normal photoelectron

- diffraction of the Se 3d level in Se overlayers on Ni (100). *Phys. Rev. Lett.* **41** (1978) 1565.
- [26] S. Kevan. Normal emission photoelectron diffraction studies at Stanford Synchrotron Radiation Laboratory. *Appl. Opt.* **19** (1980) 3974–3977.
- [27] Y. Nihei, M. Owari, M. Kudo and H. Kamada. Direct Atomic Site Determination of Foreign Atoms in a Crystal Surface Layer by X-Ray Photoelectron Diffraction. *Jpn. J. Appl. Phys.* **20** (1981) L420–L422.
- [28] K. Tamura, M. Kudo, M. Owari and Y. Nihei. X-Ray Photoelectron Diffraction (XPED) Studies of Platinum on Titanium Dioxide (110) Surface. *Chem. Lett.* **11** (1986) 1921.
- [29] K. Tamura, M. Owari and Y. Nihei. Structure of platinum particles deposited on titanium dioxide (110) surface studied by x-ray photoelectron diffraction. *Bullet. Chem. Soc. Jpn.* **61** (1988) 1539–1544.
- [30] H. Daimon, T. Nakatani, S. Imada, S. Suga, Y. Kagoshima and T. Miyahara. Strong circular dichroism in photoelectron diffraction from nonchiral, nonmagnetic material—direct observation of rotational motion of electrons. *Jpn. J. Appl. Phys* **32** (1993).
- [31] H. Daimon, T. Nakatani, S. Imada and S. Suga. Circular dichroism from non-chiral and non-magnetic materials observed with display-type spherical mirror analyzer. *J. Electron Spectrosc. Relat. Phenom.* **76** (1995) 55–62.
- [32] Y. Kato, F. Matsui, T. Shimizu, H. Daimon, T. Matsushita, F. Z. Guo and T. Tsuno. Dopant-site effect in superconducting diamond (111) studied by atomic stereophotography. *Appl. Phys. Lett.* **91** (2007) 251914–251914.

- [33] F. Matsui, T. Matsushita, Y. Kato, M. Hashimoto, K. Inaji, F. Z. Guo and H. Daimon. Atomic-Layer Resolved Magnetic and Electronic Structure Analysis of Ni Thin Film on a Cu(001) Surface by Diffraction Spectroscopy. *Phys. Rev. Lett.* **100** (2008) 207201.
- [34] P. Orders and C. Fadley. Single-scattering cluster calculations and Fourier-transform analyses of normal photoelectron diffraction. *Phys. Rev. B* **27** (1983) 781.
- [35] F. G. d. Abajo, M. Van Hove and C. Fadley. Multiple scattering of electrons in solids and molecules: A cluster-model approach. *Phys. Rev. B* **63** (2001) 075404.
- [36] T. Matsushita, Z. Guo, M. Suzuki, F. Matsui, H. Daimon and K. Hayashi. Reconstruction algorithm for atomic-resolution holography using translational symmetry. *Phys. Rev. B* **78** (2008) 144111.
- [37] T. Matsushita, F. Matsui, H. Daimon and K. Hayashi. Photoelectron holography with improved image reconstruction. *J. Electron Spectrosc. Relat. Phenom.* **178** (2010) 195–220.
- [38] T. Matsushita, F. Matsui, H. Daimon and K. Hayashi. Reconstruction Algorithm for Atomic Resolution Holography. *e-Journal of Surface Science and Nanotechnology* **9** (2011) 153–157.
- [39] J. J. Barton. Photoelectron holography. *Phys. Rev. Lett.* **61** (1988) 1356–1359.
- [40] L. Terminello, J. Barton and D. Lapiano-Smith. Holographic imaging of atoms using multiple-wave-number electron angular distribution patterns. *Phys. Rev. Lett.* **70** (1993) 599–602.

- [41] G. Harp, D. Saldin and B. Tonner. Scanned-angle x-ray photoemission holography with atomic resolution. *Phys. Rev. B* **42** (1990) 9199–9202.
- [42] S. Thevuthasan, G. Herman, A. Kaduwela, R. Saiki, Y. Kim, W. Niemczura, M. Burger and C. Fadley. Electron emission holography at keV energies: Estimates of accuracy and limitations. *Phys. Rev. Lett.* **67** (1991) 469.
- [43] T. Matsushita, F. Matsui, K. Goto, T. Matsumoto and H. Daimon. Element Assignment for Three-Dimensional Atomic Imaging by Photoelectron Holography. *J. Phys. Soc. Jpn.* **82** (2013).
- [44] T. Matsushita, A. Yoshigoe and A. Agui. Electron holography: A maximum entropy reconstruction scheme. *Europhys. Lett.* **71** (2005) 597.
- [45] P. Palmberg, G. Bohn and J. Tracy. High sensitivity Auger electron spectrometer. *Appl. Phys. Lett.* **15** (1969) 254.
- [46] D. Watson, P. Larson, D. Paul and R. Negri. High energy resolution Auger spectroscopy on a CMA instrument. *Surf. Interface Anal.* **44** (2012) 121–125.
- [47] V. Gorelik. Cylindrical mirror analyzer with entrance angles from 90.5° to 98.5° . *J. Electron Spectrosc. Relat. Phenom.* **185** (2012) 53–54.
- [48] See VG SCIENTA web page. http://www.vgscienta.com/_resources_File_R4000%20+%20Model%20overview%20data%20sheet%20v4.0%20web.pdf.
- [49] See SPECS web page. http://www.specs.de/cms/upload/PDFs/SPECS_Prospekte/2010_08_PHOIBOS_150_WAL_product_brochure_final_web.pdf.

- [50] D. Eastman, J. Donelon, N. Hien and F. Himpsel. An ellipsoidal mirror display analyzer system for electron energy and angular measurements. *Nucl. Instrum. Methods* **172** (1980) 327–336.
- [51] H. Daimon. New display-type analyzer for the energy and the angular distribution of charged particles. *Rev. Sci. Instrum.* **59** (1988) 545–549.
- [52] H. Daimon and S. Ino. Improvement of the spherical mirror analyzer. *Rev. Sci. Instrum.* **61** (1990) 57–60.
- [53] M. Kotsugi, Y. Miyatake, K. Enomoto, K. Fukumoto, A. Kobayashi, T. Nakatani, Y. Saitoh, T. Matsushita, S. Imada, T. Furuhashi, et al. Construction of two-dimensional photoelectron spectrometer at SPring-8. *Nucl. Instrum. Methods Phys. Res., Sect. A* **467** (2001) 1493–1496.
- [54] Y. Saitoh, H. Kimura, Y. Suzuki, T. Nakatani, T. Matsushita, T. Muro, T. Miyahara, M. Fujisawa, K. Soda, S. Ueda, et al. Performance of a very high resolution soft x-ray beamline BL25SU with a twin-helical undulator at SPring-8. *Rev. Sci. Instrum.* **71** (2000) 3254–3259.
- [55] H. Daimon. Stereoscopic Microscopy of Atomic Arrangement by Circularly Polarized-Light Photoelectron Diffraction. *Phys. Rev. Lett.* **86** (2001) 2034.
- [56] F. Matsui, T. Matsushita and H. Daimon. Photoelectron Diffraction and Holographic Reconstruction of Graphite. *J. Phys. Soc. Jpn.* **81** (2012) 114604.

Chapter 2. Local atomic configuration of graphene, buffer layer and precursor layer on SiC(0001) by photoelectron holography

The layer-specific atomic structure of the 4H-SiC(0001) surface at each stage of single-layer graphene formation was studied by photoelectron diffraction. 2π -steradian C 1s photoelectron intensity angular distributions (PIADs) excited by circularly-polarized soft X-ray were measured. Taking the photoelectron inelastic mean free path into account, we have separated C 1s PIADs for graphene overlayer together with interface buffer layer beneath it and precursor layer, $(6\sqrt{3} \times 6\sqrt{3})\text{-}R30^\circ$, from that of the SiC substrate. Clear diffraction rings due to the intra-layer C-C bond scattering of graphene were observed. The forward focusing peaks indicating the directions of the neighboring atoms seen from the C atoms directly bonded to the SiC substrate were observed for the case of the precursor and interface buffer layers. Furthermore, local atomic configuration of precursor layer and single layer graphene with buffer layer were reconstructed by photoelectron holography. The stacking registry of graphene on buffer layer was determined to be *AB* type. Core-level chemical shifts for each layer was deduced by taking an advantage of FFP as an excellent site selective probe.

2.1 Introduction

Graphene, a single-layer carbon network arranged in a honeycomb lattice, is expected to be a material for next generation device [1]. Epitaxial growth by the thermal decomposition of SiC substrate is a promising method for fabricating high quality and uniform graphene. To clarify the mechanism of graphene formation and determine the surface atomic arrangements at each stage, various kinds of surface analyses have been performed. Early studies have revealed that the SiC(0001) surface at graphitization precursor stage is terminated by graphite-like structure covalently bonded to the SiC substrate with $(6\sqrt{3} \times 6\sqrt{3})$ - $R30^\circ$ periodicity (hereafter the precursor layer) [2–5]. Further Si elimination leads to the formation of single-layer graphene (SLG) on C-rich buffer layer [4–7]. Interaction of the buffer layer with graphene as well as with the substrate greatly affects the electronic properties of graphene [8]. Characterization for the buried layer is a key for improving the performance of graphene device. However, the subsurface atomic structure of SLG has been still controversial.

Two neighboring C atoms of a crystalline graphite with Bernal (AB) stacking are inequivalent, which leads to the observations of a triangular lattice by scanning tunneling microscopy (STM) and three-fold symmetric low-energy electron diffraction (LEED) patterns. The STM atomic images [9–12] as well as LEED patterns [13, 14] of the bilayer graphene on the SiC(0001) surfaces are also three-fold symmetric suggesting that the two graphene sheets are in the relation of Bernal stacking. However, the observed STM images [9–12] and LEED patterns [13, 14] were six-fold symmetric in the case of SLG on the buffer layer. These observations have been regarded as the indication of SLG decoupled from the substrate. Riedl *et al.* demonstrated that the precursor and buffer layers can be decoupled from the sub-

strate and transformed to single and bilayer graphenes by hydrogen intercalation breaking Si-C bonds in reversible manner [15]. This demonstration suggests the conservation of the Bernal-like registry of SLG on graphite-like buffer layer, while some STM and LEED works proposed *AA* stacking model [12, 14]. Most of theoretical works assumed or predicted *AB* stacking model as the favorable structure for the registry of SLG on the graphite-like buffer layer [16–20], but the direct experimental determination is not yet achieved.

STM investigations have given insights into the lateral atomic arrangement of subsurface at precursor stage [21, 22]. Structures assigned to Si adatom and trimers were proposed at the buried interface. Hass *et al.* supported this Si adatom model based on the atomic density depth analysis of the graphene/4H-SiC(0001) interface by surface X-ray reflectivity (XRR) measurements [6]. Norimatsu *et al.* measured cross-sectional images of interface using high-resolution transmission electron microscopy (TEM). They proposed a C-terminated interface model in addition to bulk-SiC [23]. The local atomic configuration at interface strongly depend on the surface preparation applied and is still unclear, which is essential for understanding electronic properties. However, the subsurface information from TEM and XRR methods are averaged along beam incident direction or within lateral plane, respectively. Three-dimensional local atomic configuration has not been obtained.

Photoelectron from a localized core level is an excellent element-selective probe for surface structure analysis [24]. Forward focusing peaks (FFPs) appearing in the photoelectron intensity angular distribution (PIAD) indicate the directions of surrounding atoms seen from photoelectron emitter atom [25]. The atomic distance between the emitter and scatterer atoms can be deduced from the circular dichroism shift of FFP position [25–27] as well as from the opening angles of diffraction rings (DRs) appearing around the FFP [27, 28]. Roth

et al. have revealed the local corrugated subsurface boron nitride layer structure as well as the free-standing-like graphene overlayer on the Cu(111) surface using photoelectron diffraction (PED) [29]. We have demonstrated that the stacking orientations of exfoliated bilayer graphene flakes can be determined by using PED [30].

Recently, de Lima *et al.* have measured and separated C 1s PIADs from graphene and precursor layers on SiC(0001) by chemical-specific PED approach [31]. They evaluated long range order ripple amplitude of precursor layers and suggested just one type of hybridization for local buckling structure. Furthermore, they proposed rather flat structure model for the buffer layer. Actually, the buffer layer consists of various types of hybridization, *i.e.* sp^2 , sp^3 and the intermediates [15, 32, 33]. However, their detection range did not include any FFP, which is most sensitive signal for local structure.

Alternative approach for layer-resolved analysis is by differentiating a series of PED data at the subsequent graphitization stages. Matsui *et al.* have succeeded in the atomic-layer-resolved analysis of Ni thin film by differentiating a series of PED from wedged thickness film [34]. In this study, we have characterized each stage of thermal graphitization of the 4H-SiC(0001) substrate by the similar approach. Site-specific PIADs were deduced by considering emission angle dependence of escape depth and subtracting the substrate signal intensity. Furthermore, we succeeded in obtaining the local atomic arrangement images of SLG as well as buffer and precursor layers by photoelectron holography reconstruction.

2.2 Experimental details

A catalyst-referred etching (CARE) single-crystalline 4H-SiC(0001) wafer (N-doped, 0.02 $\Omega\cdot\text{cm}$) with an on-axis oriented Si face ($0\pm 0.5^\circ$ off) was used as the substrate [35, 36]. This wafer has an atomically flat and damage-free surface with a terrace width of 300-500 nm. Hattori *et al.* reported a recipe to obtain a large scale uniform graphene by annealing this substrate in ultrahigh vacuum (UHV) without using Si flux method during thermal epitaxial growth [37]. This specially treated sample is a solution for the graphene fabrication at much lower temperature than the conventional procedure without Si flux or Ar atmosphere. The systematic comparison of annealing effect by eliminating the Si flux procedure parameter during the epitaxial growth was achieved. The number of graphene layer on CARE-SiC can be easily controlled as function of annealing temperature and duration. They confirmed the changes of the surface structure on the CARE-SiC(0001) substrate from (1×1) to $(\sqrt{3}\times\sqrt{3})$ - $R30^\circ$ with increasing annealing temperature. The $(6\sqrt{3}\times 6\sqrt{3})$ - $R30^\circ$ precursor layer structure appeared at further 900°C annealing.

In this study, we also prepared the samples step by step in a same manner. All experiments were performed at the circularly-polarized soft-X-ray beamline BL25SU at SPring-8, in Japan [38]. The sample preparation chamber attached directly to two-dimensional display-type spherical mirror analyzer (DIANA) and is equipped with reflection high-energy electron diffraction (RHEED) system. The sample was annealed by direct current injection after installing into UHV chamber with a base pressure of less than 3×10^{-8} Pa. The surface structure was monitored by RHEED. When annealing temperatures were raised every 200°C from room temperature up to 600°C , (1×1) spots originated from the SiC surface remained.

The annealing at 800°C for 10 min gave $6\sqrt{3}$ spots originated from the graphene precursor layer. Further annealing at 1000°C for 10 min made the dilution of $6\sqrt{3}$ spots, which is strong indication of the formation of graphene on the SiC substrate [3, 5, 17]. These results are consistent with the previous reports [37].

PIAD from the sample at a specific kinetic energy is most efficiently measured using DIANA [39–41]. A two-dimensional angular distribution snapshot of a specific kinetic energy electron can be measured [25, 42–46]. The acceptance angle of the analyzer is $\pm 60^\circ$. Light was incident from the direction 45° inclined from the analyzer center. The emission angle θ dependence from 0 to 90° relative to the surface normal is measured simultaneously. A 2π steradian PIAD was obtained by scanning the sample azimuth for 360° [47, 48]. The helicity (σ_{\pm}) of monochromatized circularly-polarized soft X-ray was altered by switching the path of storage ring electrons in twin helical undulators at 0.1 Hz [49]. The photon energy resolution was better than 100 meV. The total acquisition time for a pair of 2π -steradian PIADs excited by σ_+ and σ_- helicity lights was 1 hr. All data were measured at room temperature. Electric vector was in-plane, thus core level was excited at completely s-polarized geometry. Diffraction rings and some interference patterns originated from in-plane structure become dominant. The energy window width of DIANA was set to 1 eV for spectroscopy measurements, while it was set to 40 eV for PIAD measurements, to achieve the best energy and angular resolution, respectively. All PIADs obtained with the photoelectron kinetic energy of 800 eV, and displayed in stereo projection.

2.3 Results and discussion

The chemical composition at each stage of graphitization were characterized by constant-final-state-mode two-dimensional photoelectron spectroscopy. Photoelectron kinetic energy was fixed at 800 eV, while photon energy was scanned from 800 eV to 1160 eV, so that we can detect C 1s and Si 2p core-level at the same kinetic energy. Thus the probing depth for each emission angle were kept constant for different binding energy photoelectron. Figure 2.1 shows the signal intensity ratio of C 1s over Si 2p for different annealing temperatures and emission angle ranges θ . The photoionization cross section was considered [50]. Normal and grazing emission angle spectra were sensitive to bulk and surface, respectively. The ratio did not change up to the annealing temperature of 600°C. This indicates the surface composition of the substrate was maintained below this temperature. On the other hand, at 800°C, the ratio of C 1s over Si 2p intensity at grazing angle emission was larger than that of normal emission. This implies that Si was eliminated from the SiC surface and C-rich surface was formed on the SiC substrate. The carbon overlayer thickness on the SiC surface at 1000°C annealing was estimated by following Starke and Riedl's angular-resolved XPS analysis [51]. The value was 0.34 ± 0.02 nm, which is close to the interlayer distance in graphite (0.335 nm), suggesting that the surface covered with SLG was obtained [52].

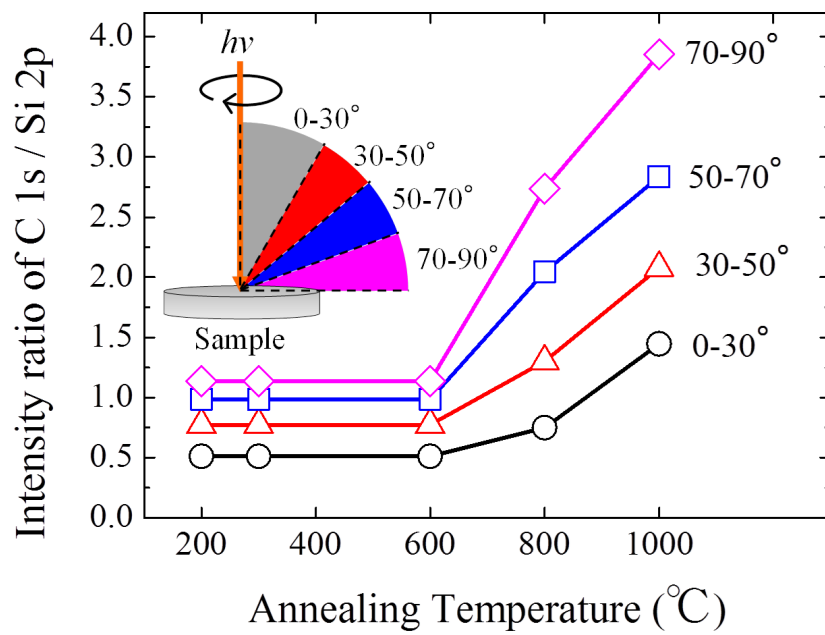


Fig. 2.1. The signal intensity ratio of C 1s over Si 2p deduced from constant-final-state-mode angle-resolved photoelectron spectra for different annealing temperatures.

Figures 2.2(a) and 2.2(b) are measured PIAD and the corresponding local structure model from hydrogen terminated SiC surface, respectively. Two PIAD images using σ_+ and σ_- helicity lights are superimposed. When excited with σ_+ helicity light, diffraction patterns rotate clockwise (red), while they rotate counterclockwise (blue) when excited with σ_- helicity light [25–27]. Red and blue arrows indicate the directions of the first neighboring Si_1 atoms and the second neighboring C_β atoms seen from the emitter C_α atom. FFP positions in the PIAD are indicated by opened marks with corresponding colors in Fig. 2.2(a). The local structure is three-fold symmetric but the observed PIAD was six-fold symmetric. This is because of the coexisting two mirrored terrace at the surface due to the stacking faults of 4H-SiC(0001) substrate. The FFP positions, diffraction patterns and their circular dichroism were basically similar to the previously measured C 1s PIAD from the 6H-SiC(0001) surface [26].

In the precursor layer PIAD shown in Fig. 2.2(c), six bright spots at vicinity of $\langle 11\bar{2}0 \rangle$ directions newly appeared in addition to the SiC bulk PIAD pattern. Three of them were marked with green opened circle. They are assigned to the FFPs emitted from the C_γ atom directly bonded with the SiC substrate to the first neighboring C_δ atoms. The FFP circular dichroism rotational shift of 2.4° correspond to the nearest C-C distance [25]. As the precursor structure grows on the SiC substrate, the substrate signal contrast appearing at around the surface normal direction in PIAD becomes smaller.

In Fig. 2.2(e), six clear DRs around the polar angle region of $55 \sim 86^\circ$, which are basically similar with that of single-crystalline graphite, were observed in addition to Fig. 2.2(c). From our previous study [27], these clear DRs at the kinetic energy of 800 eV were attributed to the second neighboring atoms from the emitter C_e atom. The opening angle of DR (28.8°)

matched with that of graphite (28.5°) within error bar. Clear circular dichroism shift at vicinity of $\langle 11\bar{2}0 \rangle$ directions due to rotational shift of DRs were observed. These characteristic structure strongly suggests the formation of flat graphene lattice having weak interaction with substrate. Moreover, the signal contrast of the SiC substrate appearing at the normal direction region in Fig. 2.2(e) became even more smaller than that of the precursor layer structure in Fig. 2.2(c).

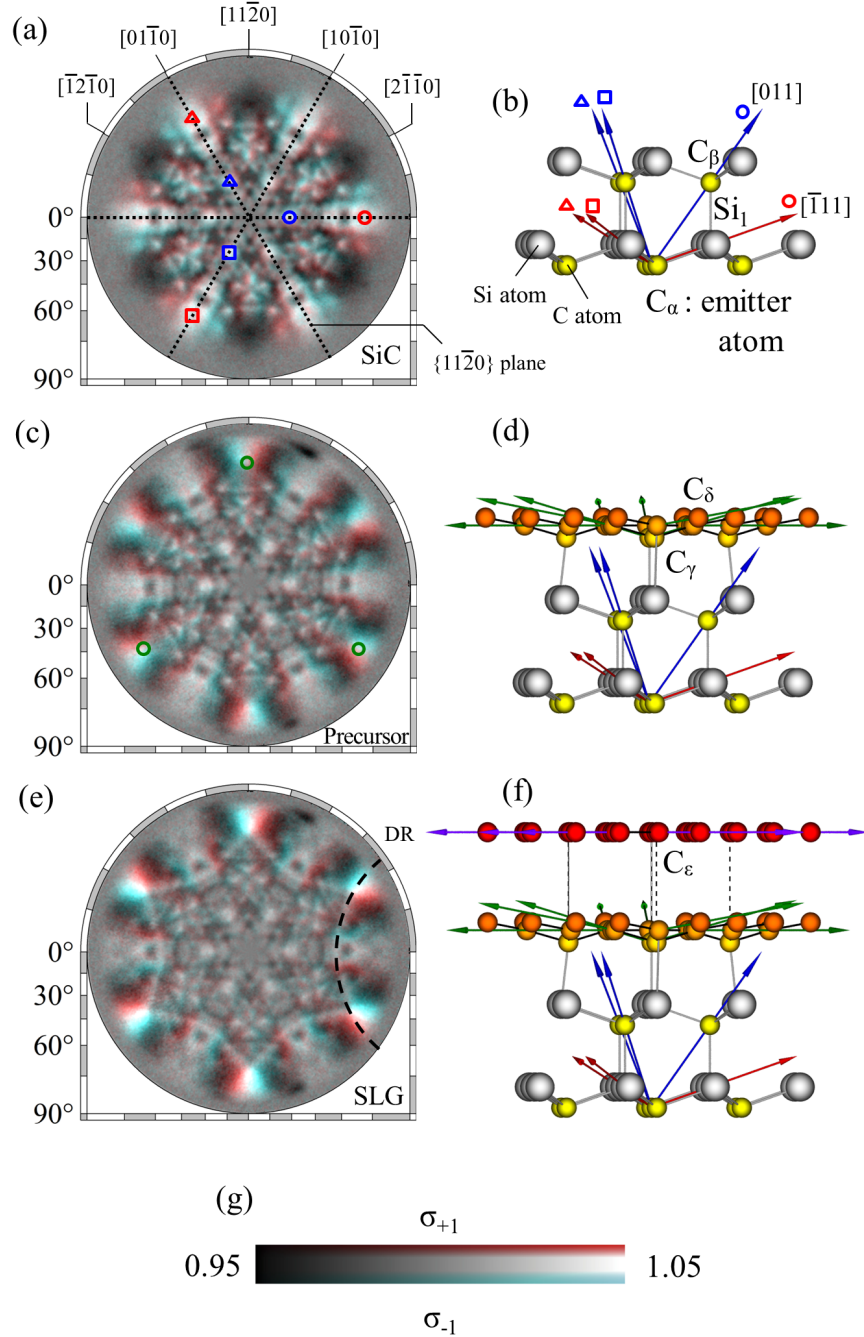


Fig. 2.2. (a) Measured 2π -steradian C 1s photoelectron intensity angular distribution (PIAD) from the 4H-SiC(0001) substrate terminated with hydrogen together and (b) structure model. Dotted lines indicate $\{11\bar{2}0\}$ planes. (c) and (d) Measured PIAD and model for $(6\sqrt{3} \times 6\sqrt{3})$ - $R30^\circ$ precursor layer. (e) and (f) Measured PIAD and model for single-layer graphene (SLG) terminated surface. Dashed arc indicates the diffraction ring (DR) originated from the scattering by the in-plane second nearest C atoms of graphene. Each PIAD was obtained with the kinetic energy of 800 eV and displayed in stereo projection. Each colored arrow indicates the direction of the forward focusing peak from each emitter atom to the surrounding atom.

The observed PIADs shown in Fig. 2.2 are the superpositions of PIADs from each photoelectron emitter site. Here we show that the PIADs from the precursor layer and SLG with buffer layer can be deduced by subtracting the SiC substrate signal intensity. The inelastic mean free path lengths of the photoelectron, λ , determined using Tanuma *et al.*'s equation were 1.93 and 1.55 nm in the SiC substrate and graphene layer, respectively [53]. The interlayer distance between the SiC bulk top and the precursor layer was assumed to be the bulk Si-C covalent bond length of $d=0.189$ nm, while graphite interlayer distance of $d=0.335$ nm was used for that between graphene and buffer layer [52]. The intensities of substrate decrease by factor of $C(\theta)$ defined in the following equation.

$$C(\theta) = \exp\left(-\frac{d}{\lambda \cos \theta}\right). \quad (5)$$

$C(0^\circ)$ of the SiC substrate are estimated to be 0.89 under the precursor layer and 0.71 under SLG and buffer layer. $C(\theta)$ decreases as the polar angle θ increases.

Figures 2.3(a) and (b) show 2π -steradian C 1s PIADs from the precursor layer and SLG together with buffer layer by subtracting the SiC substrate PIAD shown in Fig. 2.2(a) from PIADs shown in Fig. 2.2(c) and 2.2(e), respectively. The PIADs excited by σ_+ and σ_- helicity light were averaged, so that the circular dichroism effect of FFP rotation were eliminated in order to identify the exact orientation. In Fig. 1.3(a), six broad FFPs appeared in Fig. 2.2(c) can be identified more clearly. The observed FFPs were broad along the polar angle direction. This feature indicates that the vertical distribution of the surrounding atom around the emitter atom in the precursor layer. To estimate the distribution, the polar intensity profiles of the FFPs marked with bars in Fig. 2.3(a) and 2.3(b) were analyzed as shown in Fig. 2.3(c).

Note that the emission polar angle was corrected by considering refraction effect due to the difference between the vacuum level and inner potential. Therefore signal intensity at the vicinity of horizontal direction is lacking. The red solid line (A) indicates the signal intensity profile of the FFP from the precursor layer. The FFP intensity was distributed within the polar angle of $72\sim 82^\circ$ with a peak at 75° and a shoulder around 80° . These angles correspond to the hybridization bond angle for the local buckling structure which were reported in the previous studies [31]. The maximum buckling angle from the horizontal direction was determined to be 15° ($\theta=75^\circ$). Therefore, the buckling width was determined to be 0.037 nm by considering the neighboring C-C atom distance for ideal graphite value of 0.142 nm. The observed angles were smaller than that for the bulk Si-C sp^3 bond with the angle of 19.5° from the horizontal direction. The C atom intermediate rehybridization between sp^2 and sp^3 takes place to make the bond with the SiC substrate.

As shown in Fig. 2.3(b), the DR intensities from SLG marked with double dash line appeared in the PIAD. The width of double dash lines indicate the half-maximum full-width of Gaussian of the DR intensity. The DR signal intensity along the bar (C) in Fig. 2.3(b) was evaluated using the Gaussian. It was shown as black dot line (B) in Fig. 2.3(c). The profile along the bar (C) in Fig. 2.3(b) is shown with black solid line (C). This profile was larger and wider than that of (B). This indicates that the FFP intensity from buffer layer is actually coexisting with the DR signal. The FFP distribution from buffer layer was separated by subtracting (B) from (C) as indicated by blue solid line in Fig. 2.3(c). The contribution of the FFP intensity for the entire signal was 46%. This value corresponds to the attenuation degree of the FFP considering the photoelectron mean free path length. The FFP distribution from buffer layer has two component around 75° and 80° which is similar with that of the precursor

layer. This result suggests that both the precursor and buffer layers are qualitatively similar with each other. The existence of the comparable buckling structure with the precursor layer was also confirmed at the polar angle of 75° in buffer layer. Therefore, the previous structure model proposed by de Lima *et al.*, which has a flat buffer layer, was denied [31]. This is because their detection range did not include the FFPs around the horizontal direction which are the most sensitive to the local structure. The histogram in Fig. 2.3(c) indicates the polar angle distribution of the C-C bonds in buffer layer $(6\sqrt{3} \times 6\sqrt{3})\text{-}R30^\circ$ structure calculated by Sclauzero *et al* [54]. The open columns refer to buffer layer C atoms bonded with Si atom, while the solid columns refer to non-bonded C atoms. Their calculation of the buckling structure was $2 \sim 3^\circ$ smaller than our present experimentally observed distribution.

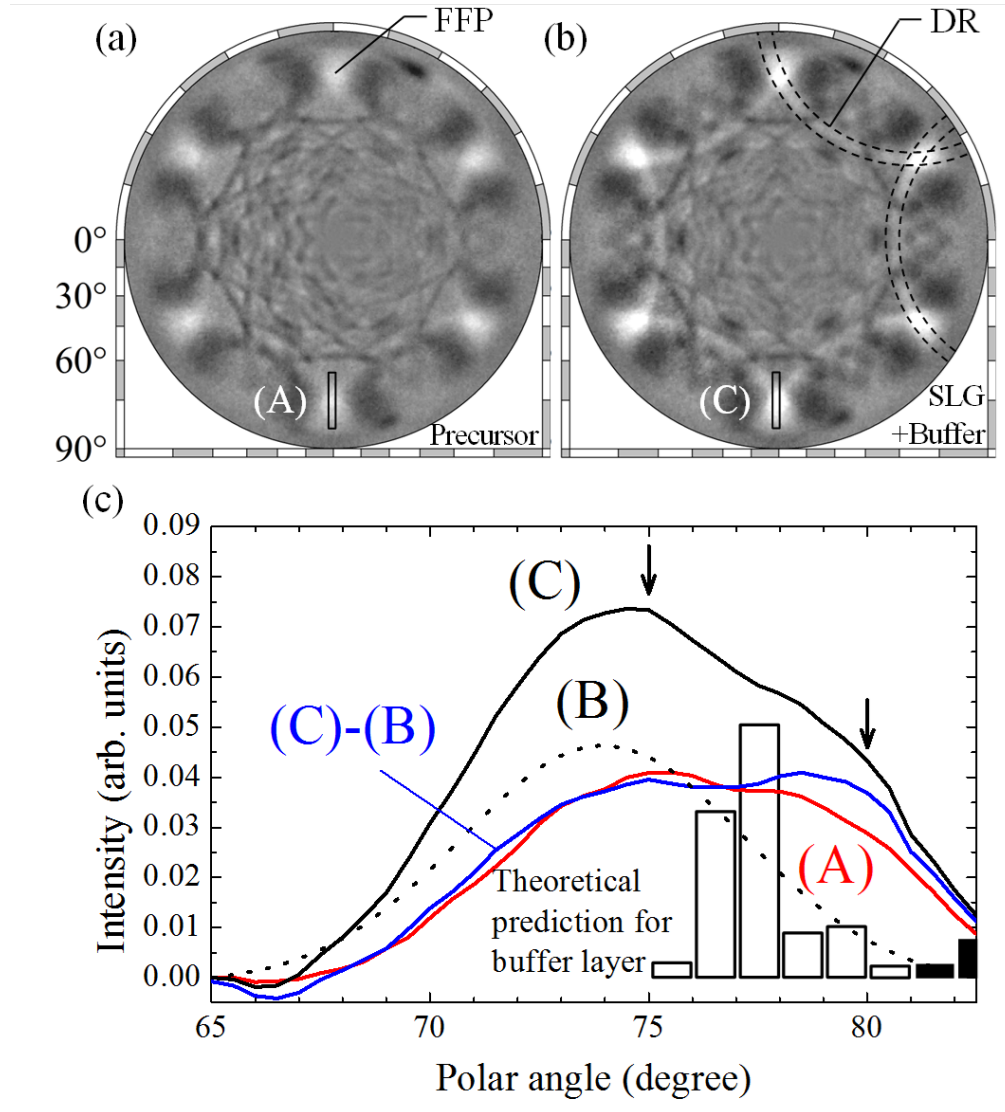


Fig. 2.3. 2π -steradian C 1s PIADs for (a) the precursor layer and (b) SLG together with buffer layer by subtracting the signal intensity from the SiC substrate. Black dashed lines indicate the half-maximum positions of DR. (c) Intensity profile of the region indicated by bars in Fig. 2.3(a) and (b) along the polar angle direction. Black and red solid lines indicate the intensity profile from the precursor layer and SLG together with buffer layer. Black dot line indicates the profile from the DR specific intensity. The histogram indicates the polar angle distribution of the C-C bonds in buffer layer $(6\sqrt{3} \times 6\sqrt{3})$ - $R30^\circ$ structure calculated by Schlauzero *et al* [54]. The open columns refer to buffer layer C atom bonded with Si atom, while the solid columns refer to non-bonded C atoms.

A scattering pattern extraction algorithm using the maximum-entropy method (SPEA-MEM), which was developed by one of the authors (T. Matsushita), was used for the reconstruction of three-dimensional atomic arrangements in the real space from the experimental PIAD in Fig. 2.3(a) and 2.3(b) [55]. PIAD data was extended to 4π -steradian by flipping the z -coordinate to fit the diffraction ring near horizontal direction [27]. Mixing operations by in-plane translational symmetry ($a=b=0.2456$ nm, $\gamma=120^\circ$) were applied among neighboring unit cells during the iterative fitting procedure for hologram reconstruction.

Figures 2.4(a) and 2.4(b) are the horizontal and vertical cross sections including the emitter atom of the reconstructed real-space atomic images from the precursor layer, respectively. Coordination was scaled by the lattice constant unit, a . Note that this image contains the total distribution of the atom seen from every emitter atom. In Fig. 2.4(a), two kinds of honeycomb lattice marked with blue and pink circles were obtained. Since two kinds of atomic sites exist within a graphite-like layer units cell, the atomic images seen from each site are superimposed. Some of the reconstructed spots marked with both blue and pink circles have strong intensities, implying that the atomic images from two different sites are overlapping at the same position. In Fig. 2.4(b), the reconstructed atomic images were observed above the emitter atom with the height range of 0.02~0.1 nm. The intensity distributions reflected the amplitude of the C-C bonds in the precursor layer. The reconstructed intensity distribution corresponds to the inter-atomic distances and directions of the precursor layer. The lowest position atoms (L) are bounded to Si atoms of the substrate as shown in Fig. 2.4(e). A pair of two top position atoms (T) with sp^2 rehybridization and having no interaction with the SiC substrate is also depicted. The reconstructed image of T atoms seen from the L atoms and from T atoms appear at different z positions. The region from $z=0.2$ nm to 0.4 nm and

the intensity contrast was enhanced by 20 times. The structure at $z=0.25$ nm correspond to the C_α - C_β atoms pair in the SiC substrate lattice, due to the reconstruction from the residual substrate signal in the background subtracted PIAD.

Figure 2.4(c) is the horizontal cross section at $z=0$ corresponding to the in-plane structure of buffer and SLG layers. As shown in Fig. 2.4(d), similar image was reconstructed at vicinity of $z=0$ in-plane structure, suggesting the existence of buckling in buffer layer similar to that of precursor layer. Furthermore, additional signals were observed at around the height of 0.335 nm. We attributed these images to SLG seen from L and T atoms in the buffer layer.

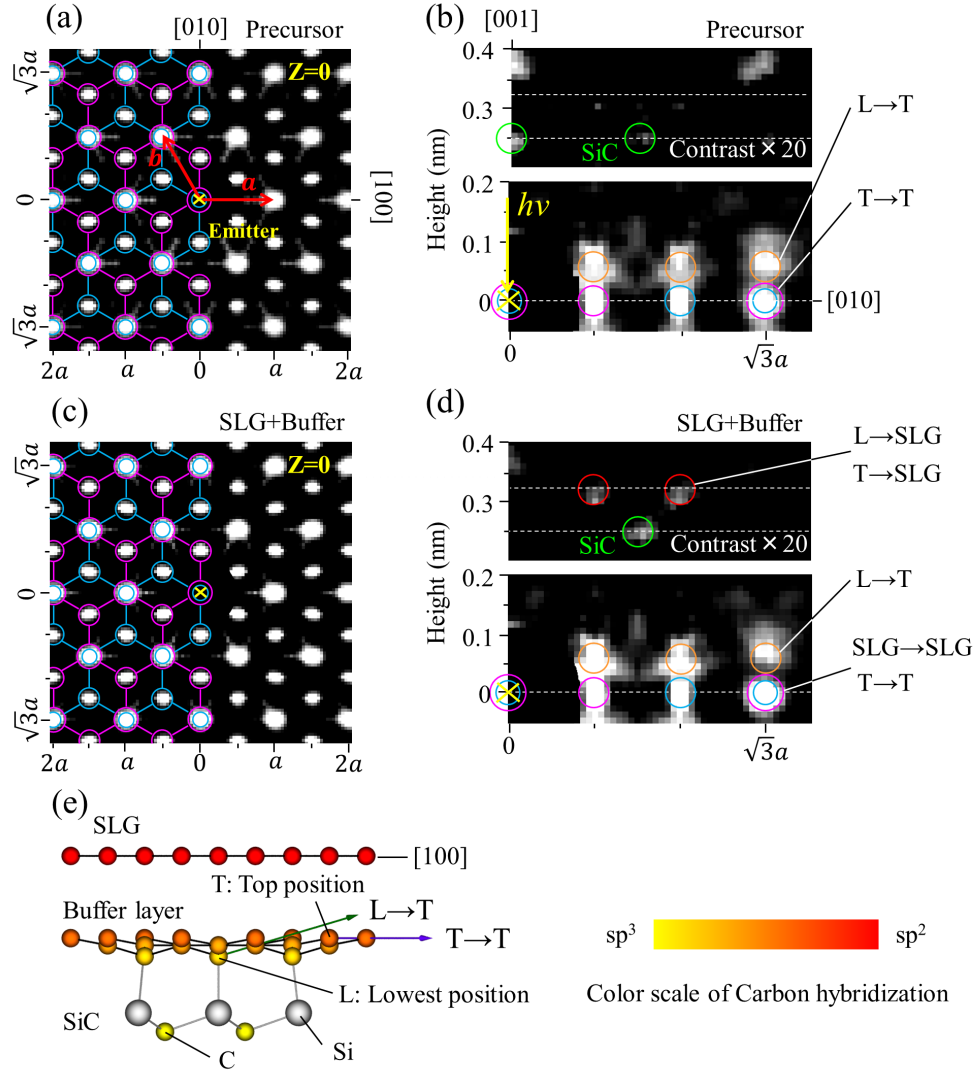


Fig. 2.4. (a) and (b) Horizontal and vertical cross sections including the emitter atom of the reconstructed real-space atomic images from the precursor layer, respectively. (c) and (d) Same as (a) and (b), but for SLG together with buffer layer. SLG region within $z = 0.2 \sim 0.4$ nm was shown separately to enhance the intensity contrast by 20 times. (e) Vertical cross section model of SLG on the SiC (0001) which has a local buckling structure in buffer layer.

To determine the stacking registry of SLG on buffer layer, the horizontal cross section image intensity of SLG at $z = 0.335 \pm 0.025$ nm seen from buffer layer atoms was integrated as shown in Fig. 2.5(a). Triangular lattice was obtained. Note that the intensity of reconstructed atomic image at the first and the third neighboring atoms are stronger than that of the center and the second neighboring atoms, while the second neighboring atomic image is strongest in the case of Fig. 2.4(a) and 2.4(c). Figure 2.5(b) is the comparison of the signal intensity at the center and the first neighboring atom in Fig. 2.5(a). The signal intensity ratio for the center and the first neighboring atom was estimated to be 2:3. The intensity distribution differs for each stacking geometry of SLG on buffer layer as shown in Fig. 2.5(c). The blue and red sphere indicate the C atom from buffer layer and SLG, respectively. In the case of *AA* stacking, two types of atomic configuration overlap at the center position, hence the center atomic image is expected to be twice more intense than that of first neighboring atomic images. On the other hand, three-fold symmetric intensity distribution is expected for *AB* stacking as well as *AC* stacking. When *AB* and *AC* stacking coexist, the signal intensity ratio for the center and the first neighboring atom will be 2:3 which matches with the present experimental result. Therefore, *AA* stacking model suggested by earlier LEED and STM analyses were denied [12, 14].

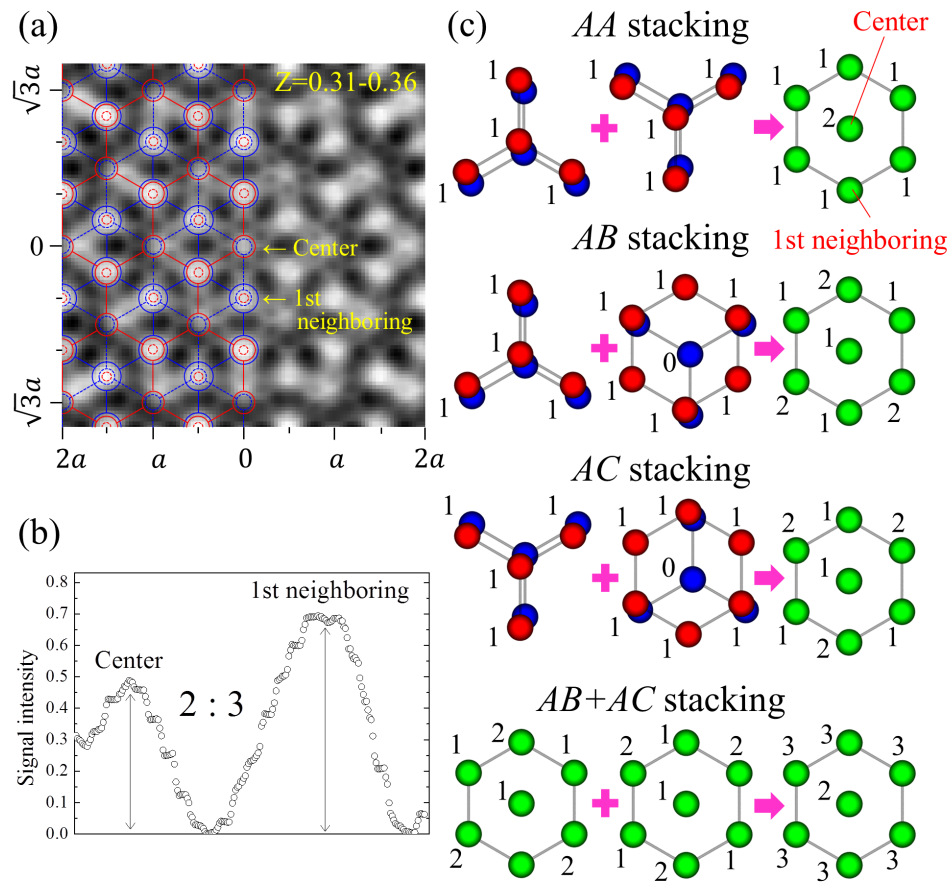


Fig. 2.5. (a) Horizontal cross section of reconstructed atomic image integrated for the height range of $z=0.31\sim 0.36$ nm for SLG. (b) The comparison of signal intensity at the center and the first neighboring atom in Fig. 5(a). (c) The schematic relation between each stacking geometry and the expected signal ratio at the center and the first neighboring atom.

From the above result, the expected structure model of graphene on $(6\sqrt{3} \times 6\sqrt{3})\text{-}R30^\circ$ -terminated 4H-SiC(0001) surface with AB stacking registry was shown in Fig. 2.6. The cross section and top view were shown in top and bottom. Basic concept was given from covalently bonded stretched graphene (CSG) model which was proposed by K.V. Emtsev *et al* [32].

The buffer layer C atoms arranged in graphene-like honeycomb lattice was placed on the top of Si adatom of non-stretched SiC substrate. The model contains 169 graphene unit cells and 108 SiC(0001) unit meshes. These C atoms have a covalent bond with the SiC substrate within several lattice match. The averaged lattice mismatch for $6\sqrt{3}$ periodicity along the $[2\bar{1}\bar{1}0]$ direction is estimated as 1.5% between six Si atoms and 13 graphite lattice units. The C atoms at the corner of $6\sqrt{3}$ and some positions were matched but the other seem to be difficult to bond with the substrate due to the mismatch above 5%. Hence, the matched atoms are expected to have graphene-like sp^2 bond without the correlation with the substrate while the mismatched atoms have the sp^3 -like covalent bond with substrate. The hybridization of C atom was shown with the color differences from yellow to red as shown in the scale of Fig. 2.4(c). To make a continuous bonding in plane, gradual relaxing from sp^2 to sp^3 was considered.

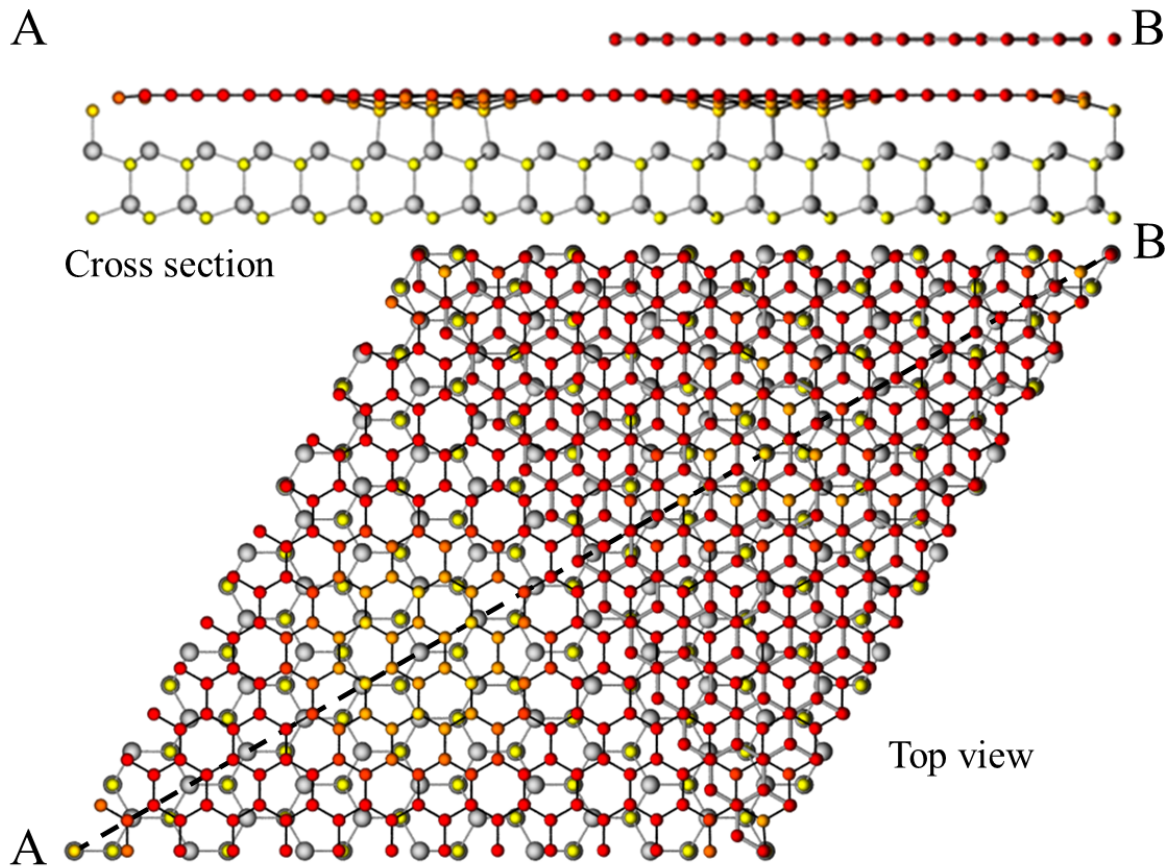


Fig. 2.6. The structure model of graphene on $(6\sqrt{3} \times 6\sqrt{3})\text{-}R30^\circ$ -terminated 4H-SiC(0001) surface with AB stacking registry. Top and bottom figures indicate the cross section and top view, respectively. White sphere indicate Si atom while the hybridization of C atom was shown with the color differences from red to yellow. The color scale was shown in Figure 1.4(c)

Taking an advantage of FFP as an excellent site selective probe, C 1s XPS spectra were disentangled [34]. Figure 2.7 is the separated C 1s XPS for graphene, buffer layer, precursor layer and SiC, respectively. The core level shifts from each termination relative to the SiC substrate were observed although the raw spectra did not show. SiC and graphene had one sharp peak at the binding energy of 285.5 and 286.5 eV, respectively. On the other hand, buffer and precursor layers showed a shoulder peak including several components. These peaks were separated into two components, SiC and sp^3 at 285.5 and 288.0 eV by Gaussian fitting. The measured core-level shifts of graphite and diamond relative to SiC were also shown with dotted and dashed lines. Each core-level shift was qualitatively agree with that of this separated spectra, indicating the direct observation of site specific electronic states were successfully achieved. The reciprocated analysis between atomic and electronic structures have been difficult for the conventional analysis but here we demonstrated that PED is ideal method for clarifying the local site analysis which relates with catalysis and device efficiency.

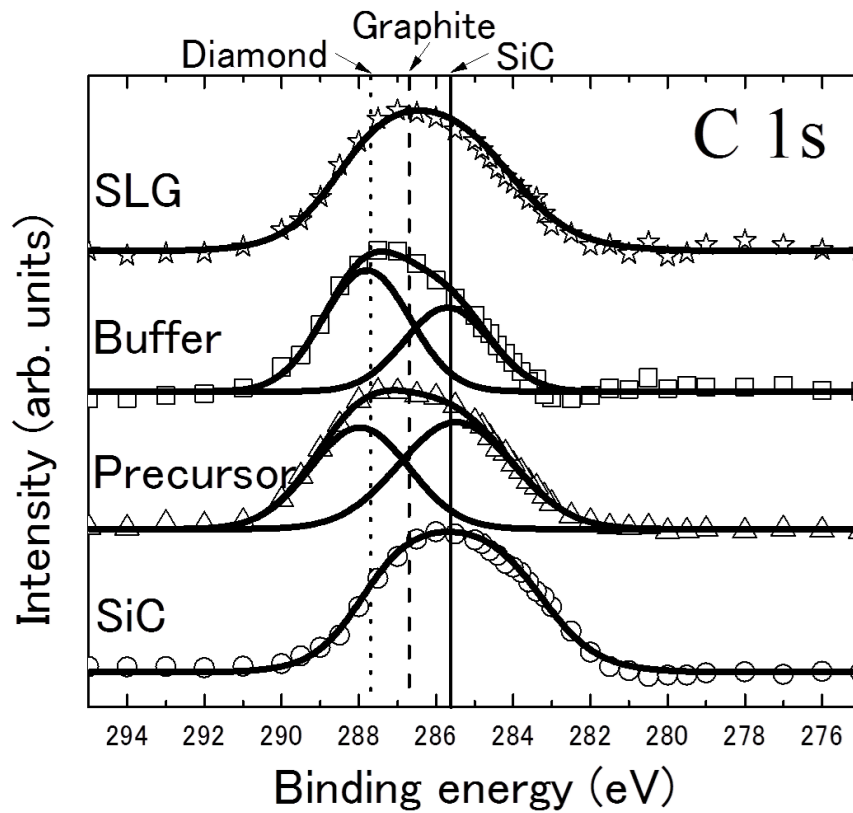


Fig. 2.7. Site specific C 1s XPS spectra from grahene, buffer layer, precursor layer and SiC. Vertical dotted and dashed lines indicate the measured C 1s core-level shifts of diamond and graphite relative to SiC.

2.4 Conclusion

In conclusion, we have characterized each stage of thermal graphitization of the 4H-SiC(0001) substrate by using PED. PIADs of the precursor layer and SLG with buffer layer were deduced by considering emission angle dependence of escape depth and subtracting the SiC substrate signal intensity. Furthermore, the local atomic configuration at the precursor layer and SLG together with buffer layer were reconstructed by photoelectron holography. The existence of the local buckling on both the precursor and buffer layers were confirmed by photoelectron FFP analyses and the reconstructed atomic images. The vertical position of SLG seen from buffer layer was observed above the emitter atom with the height of 0.335 nm. The stacking registry of SLG on buffer layer was determined to be *AB* stacking and *AA* stacking model was denied, based on the reconstructed SLG image analysis seen from buffer layer. The present comprehensive analysis of photoelectron diffraction and holography made the structure determination for local surface and interface possible directly.

References

- [1] K. S. Novoselov, A. K. Geim, S. V. Morozov, D. Jiang, Y. Zhang, S. V. Dubonos, I. V. Grigorieva and A. A. Firsov. Electric field effect in atomically thin carbon films. *Science* **306** (2004) 666–669.
- [2] L. I. Johansson, F. Owman and P. Mårtensson. High-resolution core-level study of 6H-SiC(0001). *Phys. Rev. B* **53** (1996) 13793.
- [3] X. N. Xie, H. Q. Wang, A. Wee and K. P. Loh. The evolution of 3×3 , 6×6 , $(\sqrt{3}\times\sqrt{3})R30^\circ$ and $(6\sqrt{3}\times 6\sqrt{3})R30^\circ$ superstructures on 6H-SiC(0001) surfaces studied by reflection high energy electron diffraction. *Surf. Sci.* **478** (2001) 57–71.
- [4] R. M. Tromp and J. B. Hannon. Thermodynamics and Kinetics of Graphene Growth on SiC(0001). *Phys. Rev. Lett.* **102** (2009) 106104.
- [5] I. Forbeaux, J. M. Themlin and J. M. Debever. Heteroepitaxial graphite on 6H-SiC(0001): Interface formation through conduction-band electronic structure. *Phys. Rev. B* **58** (1998) 16396.
- [6] J. Hass, J. E. Millán-Otoya, P. N. First and E. H. Conrad. Interface structure of epitaxial graphene grown on 4H-SiC(0001). *Phys. Rev. B* **78** (2008) 205424.
- [7] V. Borovikov and A. Zangwill. Step-edge instability during epitaxial growth of graphene from SiC(0001). *Phys. Rev. B* **80** (2009) 121406.
- [8] S. Y. Zhou, G. H. Gweon, A. V. Fedorov, P. N. First, W. A. De Heer, D. H. Lee,

- F. Guinea, A. H. C. Neto and A. Lanzara. Substrate-induced bandgap opening in epitaxial graphene. *Nature Mater.* **6** (2007) 770–775.
- [9] P. Mallet, F. Varchon, C. Naud, L. Magaud, C. Berger and J.-Y. Veullen. Electron states of mono- and bilayer graphene on SiC probed by STM. *Phys. Rev. B* **76** (2007) 041403.
- [10] V. W. Brar, Y. Zhang, Y. Yayon, T. Ohta, J. L. McChesney, A. Bostwick, E. Rotenberg, K. Horn and M. F. Crommie. STM of inhomogeneous electronic structure in monolayer and bilayer graphene on SiC. *Appl. Phys. Lett.* **91** (2007) 122102.
- [11] P. Lauffer, K. V. Emtsev, R. Graupner, T. Seyller, L. Ley, S. A. Reshanov and H. B. Weber. Atomic and electronic structure of few-layer graphene on SiC(0001) studied with STM/S. *Phys. Rev. B* **77** (2008) 155426.
- [12] C. Virojanadara, R. Yakimova, J. R. Osiecki, M. Syväjärvi, R. I. G. Uhrberg, L. I. Johansson and A. Zakharov. Substrate orientation: A way towards higher quality monolayer graphene growth on 6H-SiC(0001). *Surf. Sci.* **603** (2009) L87.
- [13] H. Hibino, S. Mizuno, H. Kageshima, M. Nagase and H. Yamaguchi. Stacking domains of epitaxial few-layer graphene on SiC(0001). *Phys. Rev. B* **80** (2009) 085406.
- [14] D. A. Siegel, S. Y. Zhou, F. El Gabaly, A. K. Schmid, K. F. McCarty and A. Lanzara. Stacking domains of epitaxial few-layer graphene on SiC(0001). *Phys. Rev. B* **80** (2009) 241407.
- [15] C. Riedl, C. Coletti, T. Iwasaki, A. A. Zakharov and U. Starke. Quasi-Free-Standing

- Epitaxial Graphene on SiC Obtained by Hydrogen Intercalation. *Phys. Rev. Lett.* **103** (2009) 246804.
- [16] A. Mattausch and O. Pankratov. Ab initio Study of Graphene on SiC. *Phys. Rev. Lett.* **99** (2007) 076802.
- [17] F. Varchon, R. Feng, J. Hass, X. Li, B. Ngoc Nguyen, C. Naud, P. Mallet, J.-Y. Veullen, C. Berger, E. H. Conrad and L. Magaud. Electronic Structure of Epitaxial Graphene Layers on SiC: Effect of the Substrate. *Phys. Rev. Lett.* **99** (2007) 126805.
- [18] S. Kim, J. Ihm, H. J. Choi and Y.-W. Son. Origin of Anomalous Electronic Structures of Epitaxial Graphene on SiC. *Phys. Rev. Lett.* **100** (2008) 176802.
- [19] F. Varchon, P. Mallet, J.-Y. Veullen and L. Magaud. Ripples in epitaxial graphene on the Si-terminated SiC(0001) surface. *Phys. Rev. B* **77** (2008) 235412.
- [20] G. Sciauzero and A. Pasquarello. Low-strain interface models for epitaxial graphene on SiC(0001). *Diamond and Related Materials* **23** (2012) 178.
- [21] G. M. Rutter, N. P. Guisinger, J. N. Crain, E. A. A. Jarvis, M. D. Stiles, T. Li, P. N. First and J. A. Stroscio. Imaging the interface of epitaxial graphene with silicon carbide via STM. *Phys. Rev. B* **76** (2007) 235416.
- [22] C. Riedl, U. Starke, J. Bernhardt, M. Franke and K. Heinz. Structural properties of the graphene-SiC(0001) interface as a key for the preparation of homogeneous large-terrace graphene surfaces. *Phys. Rev. B* **76** (2007) 245406.

- [23] W. Norimatsu and M. Kusunoki. Transitional structures of the interface between graphene and 6H-SiC (0001). *Chem. Phys. Lett.* **468** (2009) 52–56.
- [24] C. S. Fadley, Y. Chen, R. E. Couch, H. Daimon, R. Denecke, J. D. Denlinger, H. Gallaway, Z. Hussain, A. P. Kaduwela, Y. J. Kim, et al. Diffraction and holography with photoelectrons and fluorescent x-rays. *Prog. Surf. Sci.* **54** (1997) 341–386.
- [25] H. Daimon. Stereoscopic Microscopy of Atomic Arrangement by Circularly Polarized-Light Photoelectron Diffraction. *Phys. Rev. Lett.* **86** (2001) 2034–2037.
- [26] F. Matsui, N. Nishikayama, N. Maejima, H. Matsui, K. Goto, M. Hashimoto, T. Hatayama, T. Matsushita, Y. Kato, S. Tanaka and H. Daimon. Site-Specific Stereograph of SiC (0001) Surface by Inverse Matrix Method. *J. Phys. Soc. Jpn.* **80** (2011) 013601.
- [27] F. Matsui, T. Matsushita and H. Daimon. Photoelectron Diffraction and Holographic Reconstruction of Graphite. *J. Phys. Soc. Jpn.* **81** (2012) 114604.
- [28] W. Auwärter, T. J. Kreuzer, T. Greber and J. Osterwalder. XPD and STM investigation of hexagonal boron nitride on Ni(111). *Surf. Sci.* **429** (1999) 229–236.
- [29] S. Roth, F. Matsui, T. Greber and J. Osterwalder. Chemical Vapor Deposition and Characterization of Aligned and Incommensurate Graphene/Hexagonal Boron Nitride Heterostack on Cu(111). *Nano Lett.* **13** (2013) 2668.
- [30] F. Matsui, R. Ishii, H. Matsuda, M. Morita, S. Kitagawa, T. Matsushita, S. Koh and H. Daimon. Characterizing Edge and Stacking Structures of Exfoliated Graphene by Photoelectron Diffraction. *Jpn. J. Appl. Phys.* **52** (2013) 110110.

- [31] L. H. d. Lima, A. d. Siervo, R. Landers, G. A. Viana, A. M. B. Goncalves, R. G. Lacerda and P. Häberle. Atomic surface structure of graphene and its buffer layer on SiC(0001): A chemical-specific photoelectron diffraction approach. *Phys. Rev. B* **87** (2013) 081403.
- [32] K. V. Emtsev, F. Speck, T. Seyller, L. Ley and J. D. Riley. Interaction, growth, and ordering of epitaxial graphene on SiC(0001) surfaces: A comparative photoelectron spectroscopy study. *Phys. Rev. B* **77** (2008) 155303.
- [33] T. Langer, H. Pfnür, H. W. Schumacher and C. Tegenkamp. Graphitization process of SiC(0001) studied by EELS. *Appl. Phys. Lett.* **94** (2009) 112106.
- [34] F. Matsui, T. Matsushita, Y. Kato, M. Hashimoto, K. Inaji, F. Z. Guo and H. Daimon. Atomic-Layer Resolved Magnetic and Electronic Structure Analysis of Ni Thin Film on a Cu(001) Surface by Diffraction Spectroscopy. *Phys. Rev. Lett.* **100** (2008) 207201.
- [35] H. Hara, Y. Sano, H. Mimura, K. Arima, A. Kubota, K. Yagi, J. Murata and K. Yamauchi. Novel abrasive-free planarization of 4H-SiC(0001) using catalyst. *J. Electron. Mater.* **35** (2006) L11–L14.
- [36] T. Okamoto, Y. Sano, H. Hara, K. Arima, K. Yagi, J. Murata, H. Mimura and K. Yamauchi. Damage-Free Planarization of 2-Inch 4H-SiC Wafer Using Pt Catalyst Plate and HF Solution. In *Mater. Sci. Forum* Vol. 600 835–838. Trans Tech Publ (2009).
- [37] A. N. Hattori, T. Okamoto, S. Sadakuni, J. Murata, K. Arima, Y. Sano, K. Hattori, H. Daimon, K. Endo and K. Yamauchi. Formation of wide and atomically flat graphene layers on ultraprecision-figured 4H-SiC(0001) surfaces. *Surf. Sci.* **605** (2011) 597–605.

- [38] Y. Saitoh, H. Kimura, Y. Suzuki, T. Nakatani, T. Matsushita, T. Muro, T. Miyahara, M. Fujisawa, K. Soda, S. Ueda, et al. Performance of a very high resolution soft x-ray beamline BL25SU with a twin-helical undulator at SPring-8. *Rev. Sci. Instrum.* **71** (2000) 3254–3259.
- [39] H. Daimon. New display-type analyzer for the energy and the angular distribution of charged particles. *Rev. Sci. Instrum.* **59** (1988) 545–549.
- [40] H. Daimon and S. Ino. Improvement of the spherical mirror analyzer. *Rev. Sci. Instrum.* **61** (1990) 57–60.
- [41] M. Kotsugi, Y. Miyatake, K. Enomoto, K. Fukumoto, A. Kobayashi, T. Nakatani, Y. Saitoh, T. Matsushita, S. Imada, T. Furuhashi, et al. Construction of two-dimensional photoelectron spectrometer at SPring-8. *Nucl. Instrum. Methods Phys. Res., Sect. A* **467** (2001) 1493–1496.
- [42] F. Matsui, H. Daimon, F. Guo and T. Matsushita. Visualization of graphite atomic arrangement by stereo atomscope. *Appl. Phys. Lett.* **85** (2004) 3737–3739.
- [43] Y. Kato, F. Matsui, T. Shimizu, H. Daimon, T. Matsushita, F. Guo and T. Tsuno. Dopant-site effect in superconducting diamond (111) studied by atomic stereophotography. *Appl. Phys. Lett.* **91** (2007) 251914–251914.
- [44] F. Matsui, T. Matsushita, Y. Kato, F. Guo and H. Daimon. Site-specific orbital angular momentum analysis of graphite valence electron using photoelectron forward focusing peaks. *J. Phys. Soc. Jpn.* **76** (2007).

- [45] F. Matsui, T. Matsushita, Y. Kato, M. Hashimoto, K. Inaji, F. Guo and H. Daimon. Atomic-layer resolved magnetic and electronic structure analysis of Ni thin film on a Cu (001) surface by diffraction spectroscopy. *Phys. Rev. Lett.* **100** (2008) 207201.
- [46] F. Matsui, T. Matsushita and H. Daimon. Atomic-layer-resolved analysis of surface magnetism by diffraction spectroscopy. *J. Electron Spectrosc. Relat. Phenom.* **181** (2010) 150–153.
- [47] T. Matsushita, F. Guo, F. Matsui, Y. Kato and H. Daimon. Three-dimensional atomic-arrangement reconstruction from an Auger-electron hologram. *Phys. Rev. B* **75** (2007) 085419.
- [48] K. Inaji, F. Matsui, Y. Kato, C. Sakai, T. Narikawa, T. Matsushita, F. Guo and H. Daimon. Circular dichroism of forward focusing peaks and diffraction rings in 2π steradian Si 2p photoelectron pattern. *Appl. Surf. Sci.* **254** (2008) 7549–7552.
- [49] T. Muro, T. Nakamura, T. Matsushita, H. Kimura, T. Nakatani, T. Hirono, T. Kudo, K. Kobayashi, Y. Saitoh, M. Takeuchi, T. Hara, K. Shirasawa and H. Kitamura. Circular dichroism measurement of soft X-ray absorption using helicity modulation of helical undulator radiation. *J. Electron Spectrosc. Relat. Phenom.* **144** (2005) 1101–1103.
- [50] The data are taken from: J.J. Yeh, Atomic Calculation of Photoionization Cross-Sections and Asymmetry Parameters, Gordon and Breach Science Publishers, Langhorne, PE (USA), 1993 and from J.J. Yeh and I.Lindau, Atomic Data and Nuclear Data Tables, 32, 1-155 (1985).

- [51] U. Starke and C. Riedl. Epitaxial graphene on SiC (0001) and SiC(000 $\bar{1}$) from surface reconstructions to carbon electronics. *J. Phys.: Condens. Matter* **21** (2009) 134016.
- [52] P. Trucano and R. Chen. Structure of graphite by neutron diffraction. *Nature* **258** (1975) 136–137.
- [53] S. Tanuma, C. Powell and D. Penn. Calculations of electron inelastic mean free paths. ix. Data for 41 elemental solids over the 50 eV to 30 keV range. *Surface and Interface Analysis* **43** (2011) 689–713.
- [54] G. Sclauzero and A. Pasquarello. Carbon rehybridization at the graphene/SiC (0001) interface: Effect on stability and atomic-scale corrugation. *Phys. Rev. B* **85** (2012) 161405.
- [55] T. Matsushita, F. Z. Guo, M. Suzuki, F. Matsui, H. Daimon and K. Hayashi. Reconstruction algorithm for atomic-resolution holography using translational symmetry. *Phys. Rev. B* **78** (2008) 144111.

Chapter 3. Disentanglement of site selective X-ray absorption spectra of catalytic Ni₂P surface by photoelectron diffraction spectroscopy

Ni L_3 ($2p_{2/3}$) edge X-ray absorption spectra (XAS) of a single-crystalline Ni₂P(10 $\bar{1}$ 0) catalytic surface for hydrodesulfurization reaction were measured while collecting a series of 2π -steradian Ni-LMM Auger electron intensity angular distributions (AIADs) at each photon energy. Ni₂P includes two major Ni sites, pyramidal (Py) and tetrahedral (T), in the bulk. The AIAD patterns on the lower and higher energies in XAS, which emphasized the local atomic site information, showed different patterns by normalizing with that of the L_3 edge jump. The AIAD pattern contrast disappeared at the L_3 peak, indicating the isosbestic point of two Ni sites. The spatial distributions, the density of the state (DOS) of the Py-Ni site was more dominant than the T-Ni site near the Fermi-level, were clarified by comparing the simulated AIADs. Taking advantage of FFP as an excellent site selective probe, site selective XAS spectra were disentangled. The difference of spectra coming from the DOS near the Fermi-level was successfully observed.

3.1 Introduction

Ni₂P is a promising material for next-generation petroleum processing catalysts with high activities in hydrodesulfurization (HDS) and hydrodenitrogenation (HDN) reactions [1]. The origin of high activity is considered as the number of surface active sites come from a three dimensional Ni₂P structure while that of conventional Co-Mo or Ni-Mo sulfide catalysts have a layered MoS₂ structure with Co and Ni at the edges. Therefore, several catalytic reformings, including the increase of surface area and the interplay with the substrate, have been a curious area in Ni₂P study along with the development of a better catalyst.

To clarify the relation between the surface structure and catalytic properties, X-ray absorption fine structure (XAFS), which enables an operando-observation, has been conducted. XAFS is a powerful tool for studying the local atomic and electronic structures. Oyama *et al.* prepared several crystallite size of the Ni₂P phase with a range of 3.8-10.1 nm and found that the smaller particle size, which shows a higher catalytic activity, tended to have a higher coordination number [2]. This indicates that the DOS of the pyramidal (Py)-Ni site is more dominant than the tetrahedral (T)-Ni site on the Ni₂P surface (see Fig. 1). Time-resolved simultaneous measurements of quick-XAFS and Fourier transform infrared spectra during thiophene HDS indicated that a Ni phosphosulfide (NiPS) phase was responsible for the catalytic activity [3, 4]. Wada *et al.* reported the correlation between the change in the shoulder structure which reflected the local T-Ni site in Ni K-edge X-ray absorption near edge structure (XANES) spectra and the amount of Ni-S bonds [5]. The decreasing of the shoulder peak corresponded to a decrease in the number of T-Ni sites because a site-selective Ni-S bond formation indicates that T-Ni sites on the surface preferentially react with S [6, 7].

However, the complex Ni₂P structure with more than two Ni-P distances has been difficult to analyze. The characterization of a bimetallic NiFe phosphide catalyst, which has higher catalytic activity than commercial catalysts, probed just T-Ni site although the NiFeP catalyst consists of a Ni₂P structure with the equivalent occupancy of S- and T-Ni sites [8]. They explained that the XAFS intensity collected the shorter distance of T-Ni sites or the T-Ni termination. It is not easy to obtain the relation between the structure and catalytic activity only by XAFS and surface sensitive yield must be taken in account for catalyst surface analysis.

A photoelectron from a localized core level is an excellent element selective probe for surface structure analysis [9]. Forward focusing peaks (FFPs) appearing in the photoelectron intensity angular distribution (PIAD) indicate the directions of surrounding atoms seen from photoelectron emitter atom [10]. The atomic distance between the emitter and scatterer atoms can be deduced from the opening angles of diffraction rings (DRs) appearing around the FFP [11, 12]. Kato *et al.* clarified that the dopant site in B-diamond crystal as the superconductive material. This achievement implied that the application for the diluted material less than several % is possible [13]. Matsui *et al.* have developed a direct method for detecting the electronic and atomic structures of each atomic layer at the surface, *diffraction spectroscopy*, based on the photon energy dependence of Auger electron intensity angular distributions (AIADs).[14]. They succeeded in obtaining atomic-layer resolved x-ray absorption (XAS) for a Ni ultrathin film on Cu(001) surface. Here we have characterized the single-crystalline Ni₂P surface by a combined measurement of Auger electron yield Ni *L*-edge XAS and Ni-LMM AIAD. The local site contribution for XAS was deduced by AIAD. Disentanglement of site selective XAS was achieved by photoelectron diffraction analysis.

3.2 Experimental details

A single-crystalline $\text{Ni}_2\text{P}(10\bar{1}0)$ surface was used as a sample [15]. The $(10\bar{1}0)$ surface terminates with a Ni/P stoichiometric composition of bulk 2:1, and is suitable for studying the bulk Ni_2P chemical feature [16]. The sample was cut and mechanically polished to a mirror finishing. The sample surface was cleaned by Ar^+ sputtering at 2.5 keV (current: 1 μA , time: 30 min, Ar pressure: 1×10^{-3} Pa). It was then annealed at 350°C by repeating injection a direct current after transferring into an ultra-high vacuum (UHV) chamber with a base pressure of less than 3×10^{-8} Pa [16]. The annealing temperature was monitored by a K-type thermo-coupling directly attached to the back of the sample. The surface structure was characterized by reflection high-energy electron diffraction (RHEED). A sharp (1×1) structure coming from the clean bulk lattice was confirmed [16]. The chemical composition was checked by XPS. The C and O impurities were successfully removed after the cleaning processes.

All experiments were performed using the circularly-polarized soft x-ray beamline BL25SU at SPring-8 in Japan [17]. The sample preparation chamber was attached directly to a two-dimensional display-type spherical mirror analyzer (DIANA)[18–20], and the sample was transferred under UHV. AIAD from the sample at a specific kinetic energy was most efficiently measured using DIANA. A two-dimensional angular distribution snapshot of a specific kinetic energy electron could be measured [10, 13, 14, 21–23]. The acceptance angle of the analyzer was $\pm 60^\circ$. Light was incident from the direction of 45° inclined from the analyzer center. The emission angle θ dependence from 0 to 90° relative to the surface normal was measured simultaneously. A 2π steradian AIAD was obtained by scanning the sample azimuth for 360°

every 20° [24, 25]. The total acquisition time for 2π -steradian AIAD was 2 min. The photon energy resolution was better than 100 meV. All data was measured at room temperature. The energy window width of DIANA was set to 30 eV. All data was obtained with the most intense signal of Ni-LMM Auger electron kinetic energy at 840 eV, and displayed in azimuth equidistant projection.

3.3 Results and discussion

Figure 3.1(a) shows the crystalline structure of Ni₂P. The red and yellow spheres indicate Ni and P atoms, respectively. Ni₂P belongs to the space group $P\bar{6}_2m$ of hexagonal symmetry with lattice parameters of $a = b = 0.586$ nm and $c = 0.338$ nm. [26] In the bulk, two kinds of stoichiometric layers, namely Ni₃P and Ni₃P₂ layers, stack alternatively along the [0001] direction. Ni has two kinds of atomic sites which surrounded by a tetrahedral (T) coordinated P atoms in the Ni₃P₂ layer and that of pyramidal (Py) coordination in the Ni₃P layer. Since both T- and Py-Ni sites rotate every 120° in each layer, 6 kinds of Auger electron emitter sites are expected. The blue colored square in Fig. 3.1(a) indicates the (10 $\bar{1}$ 0) plane which was used in this study. The (10 $\bar{1}$ 0) surface shows a mirror symmetric structure with a boundary of (0001) plane.

Figure 3.1(b) shows 2 π -steradian Ni-LMM AIAD which was measured at the photon and kinetic energies of 854.3 eV and 840 eV, respectively. Each energy was set to obtain the most intense signal of Auger electron. The center of AIAD corresponds to the sample normal of the [10 $\bar{1}$ 0] direction. The AIAD showed mirror-symmetry with a boundary of the center vertical direction, indicating the (0001) plane. The AIAD was qualitatively similar to the characteristics of a Ni₂P bulk but the contribution from each Ni site was difficult to understand because the six AIADs from each emitter sites, were superimposed.

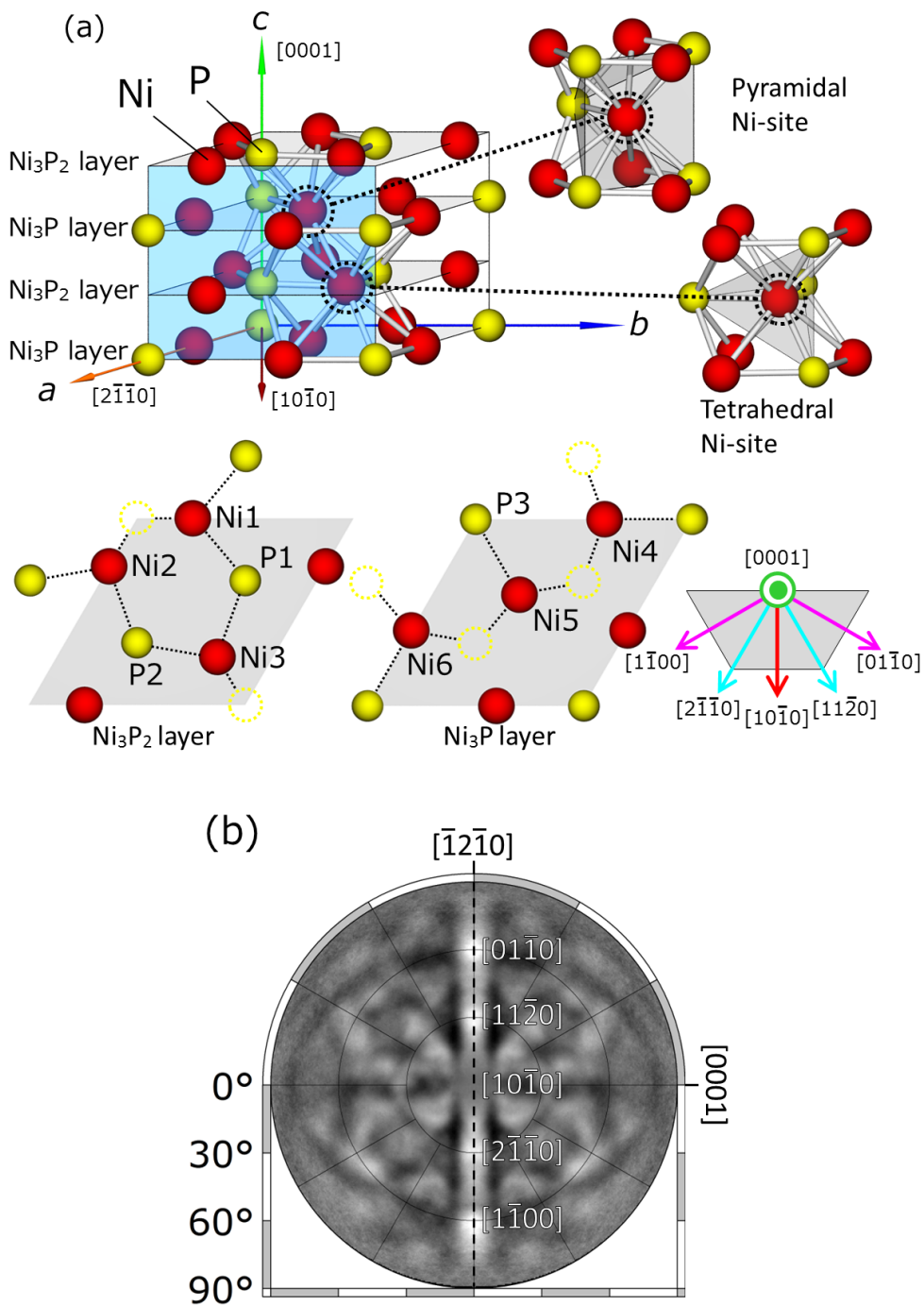


Fig. 3.1. (a) The crystalline structure of Ni_2P . Red and yellow spheres indicate Ni and P atoms, respectively. Green, orange and blue colored arrows indicate $[0001]$, $[2\bar{1}\bar{1}0]$, $[\bar{1}2\bar{1}0]$ directions. Ni_3P_2 and Ni_3P layers stack alternatively along $[0001]$ direction. The blue colored square indicates the $\{10\bar{1}0\}$ plane which was used in this study. (b) 2π -steradian Ni-LMM Auger electron intensity angular distribution (AIAD) from a $\text{Ni}_2\text{P}(10\bar{1}0)$ surface.

Figure 3.2(a) is Ni L-edge XAS spectrum from the single crystalline Ni₂P(10 $\bar{1}$ 0) surface while integrating all hemisphere angles of Ni-LMM Auger electron intensity. Two kinds of L₃ and L₂ peaks were seen due to the spin orbit interaction of 2p_{3/2} and 2p_{1/2}. The inset indicates Ni2p XPS spectrum whose the energy resolution was better than that of XAS. Each peak has perfect Gaussian dispersion, indicating that the electronic potential difference between T and Py-Ni sites were not observed.

The spectra at the bottom of Fig. 3.2(b) is XAS spectrum expanding the Ni L₃ area. Only a single peak was observed within the photon energy resolution of 0.1 eV. At the same time, the photon energy dependence of 2 π -steradian Ni-LMM AIADs were measured. The spatial distribution in the conduction band corresponded to the local atomic structures is preserved in every AIAD. However, the series of AIAD structures were not apparently changed, indicating that the superposition from all emitter sites were dominant in AIADs. The pattern contrast became obvious when the XAS intensity increased. In order to discuss the contributions from each Ni site, the superimposed components from the bulk was removed by dividing with L₃ edge jump AIAD at the photon energy of 865 eV, since it includes both Ni site information equivalently (the top fogire of Fig. 3.2(b)). The difference AIAD at the photon energy of 852 eV, which is the base line region of the XAS spectrum, showed a slight contrast-reversed presentation of Fig. 3.1(b) because raw AIAD did not show the pattern contrast. In the difference AIADs of 853.5 and 855.5 eV, different structures were clearly appeared. If the XAS spectrum was composed of only one site information, the pattern contrast would not appear. Each pattern had almost a negative relation, which is not due to excess division. The pattern contrast at the L₃ peak of 854.3 eV disappeared, implying the isosbestic point from two major Ni sites. Also, the XAS hemline region at 857 eV did not show the pattern

contrast, indicating that there is no energetic spatial distribution from either Ni sites.

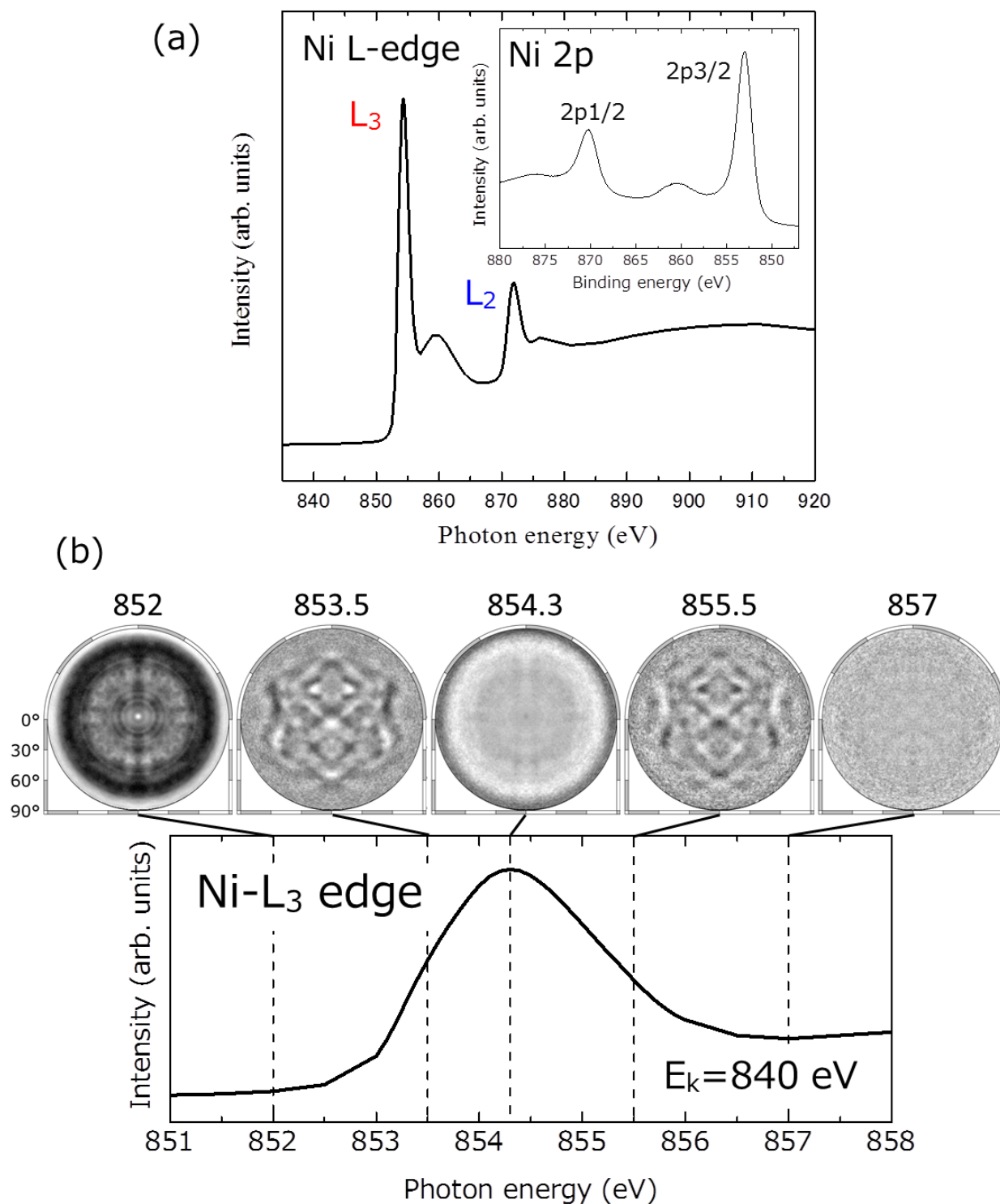


Fig. 3.2. (a) Ni L_3 edge X-ray absorption spectrum from $\text{Ni}_2\text{P}(10\bar{1}0)$ surface by integrating Ni-LMM Auger electron signal intensity. (b) (the bottom) Ni L_3 edge XAS spectra. (the top) The series of difference AIADs from a $\text{Ni}_2\text{P}(10\bar{1}0)$ surface while the photon energy was scanned from 852 to 857 eV with the kinetic energy of 840 eV. Note that the difference AIADs were obtained by dividing with that of a L_3 edge jump at the photon energy of 858 eV to emphasize the fine residual.

To identify these AIADs around 853.5 and 855.5 eV, the AIADs from Py- and T-Ni sites were simulated by the multiple scattering pattern code, *TMSP*, which was developed by T.Matsushita [27]. A sphere cluster with a radius of 7Å was used in the simulation because the best agreement was obtained in the bulk reconstruction. Figures 3.3(a) and 3.3(b) show measured AIADs at the photon energies of 853.5 and 855.5 eV after removing the pattern noise. Figures 2.3(c) and 2.3(d) show simulated AIAD after the following patter processing. The contributions of Py- and T-Ni sites for Fig. 3.3(a) and 3.3(b) were considered. The set of residual component by dividing with the L_3 edge jump is explained by the following equation:

$$P = \frac{(1 + \alpha)Py + (1 - \alpha)T}{Py + T} \quad (6)$$

where α is the factor of composition ratio from each Ni site at each AIAD, Py and T are the contributions from Py- and T-Ni sites. Here, the L_3 edge jump AIAD was assumed as $(Py + T)$ because it includes both site AIADs equivalently. This equation can be simplified as the following,

$$P = 1 + \alpha \frac{Py - T}{Py + T} \quad (7)$$

Therefore, the data processing of the simulated $(Py - T)/(Py + T)$ and $(T - Py)/(Py + T)$ will correspond to the measured AIADs which are dominating from the Py- and T-Ni sites, respectively. The pattern relation between Fig. 3.3(c) and 3.3(d) show the negative presentation which was seen in the measured result, indicating that the data processing was

actually correct. Total structures were also similar between Fig. 3.3(a) and 3.3(c) and between Fig. 3.3(b) and 3.3(d) but the most intense FFP positions, coming from the first-neighboring Ni-P bonding, that most resemble each other are shown with black and red dotted circles in Fig. 3.3. As mentioned above, the electronic distribution near the Fermi-level was found to be dominant for the local Py-Ni site.

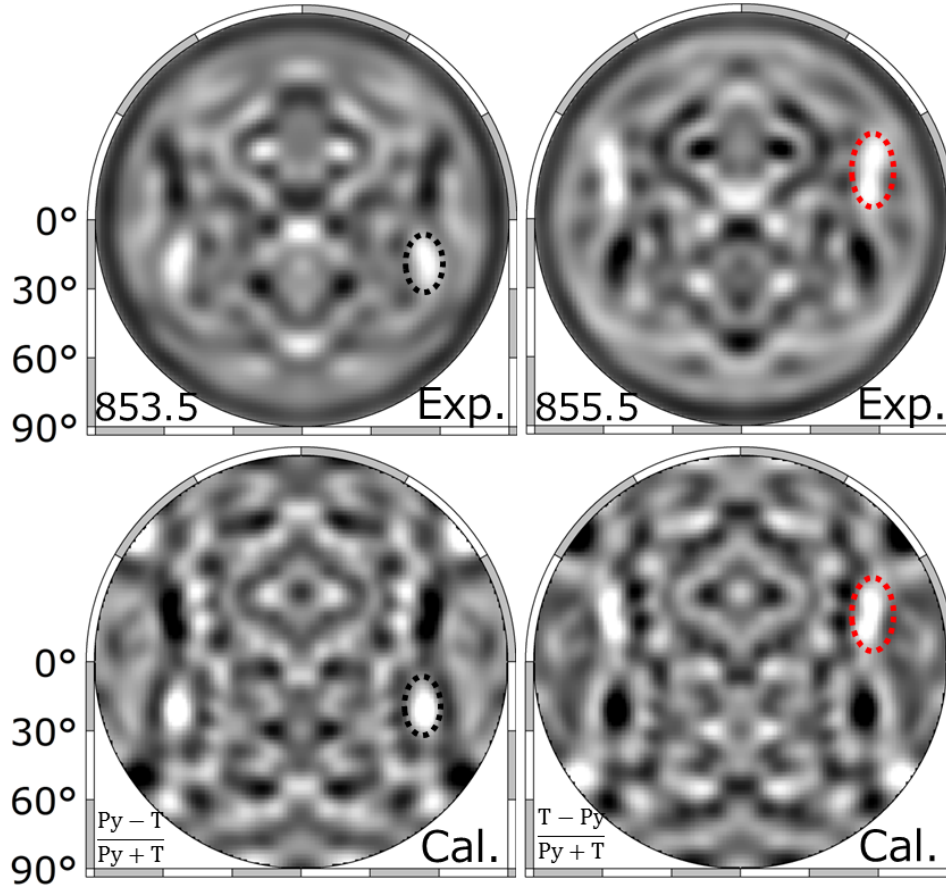


Fig. 3.3. (a), (b) The set of measured 2π -siteraidan Ni-LMM AIAD at the photon energy of 853.5 and 855.5 eV after removing pattern noise. (c)(d) The set of simulated AIADs for $(Py - T)/(Py + T)$ and $(T - Py)/(Py + T)$ pattern processes similar to Fig. 3.3(a) and 3.3(b). Black and red dotted circles indicate the FFP from the first-neighboring Ni-P bonding for each Ni site.

Taking advantage of FFP in AIAD as an excellent site-specific probe, the disentanglement of XAS into site-selective spectra was performed by means of photoelectron diffraction spectroscopy [14]. In Fig. 3.4, site selective XAS was separated by collecting the signal intensity from the FFP as mentioned above. The black and red solid lines show Py- and T-Ni site specific XAS spectra, respectively. Each peak width was similar but a slight difference less than 0.1 eV was observed, although core-level shifts of Ni 2p coming from the local structure were not observed in XPS. The depth-resolved XAS was also analyzed by integrating the polar angle intensity every 10 degrees but the differences were not observed since the contribution from the surface structure is minor (not shown). Therefore, the difference in density of state (DOS) dispersion is thought to affect the XAS spectra. Note that the summation of both site XAS (blue solid line) was consistent with the raw spectrum (green circle plots), indicating that the disentanglement of XAS was successfully achieved.

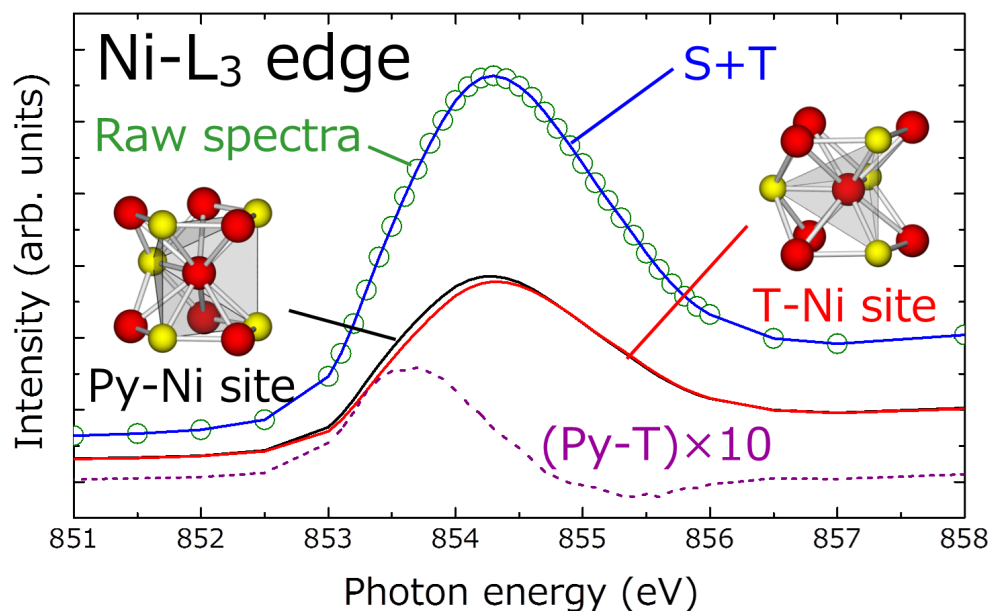


Fig. 3.4. Disentanglement of site selective Ni L_3 edge XAS spectra by integrating the FFP signal marked with black and red dotted circles in Fig. 3.3(a) and 3.3(b) for the series of Ni-LMM AIADs at each photon energy. Black and red solid lines indicate the XAS spectra for pyramidal (Py)- and quasi tetrahedral (T)-Ni site spectra. The spectra width was the same but the peak position of the Py-Ni site was slightly shifted to a lower photon energy than that of T-Ni. The blue solid line is the summation of the black and red lines. The green circle plots indicate the raw Ni L_3 edge XAS spectrum by integrating all hemisphere angles.

To clarify the differences in site selective XAS spectra, DOS calculations were performed using WIEN2k. Wave function, Argumented Plane Wave (APW) + local orbitals (lo) method, was adapted for all orbitals, 4s and 3d. 5000 kpoints was considered but the core hole was not counted because the core level shift of Ni 2p was not observed within the energy resolution of several dozen meV. Figure. 3.5(a) shows the site selective DOS for 3d, 4s and the summed orbitals. The intensity of 3d was about a dozen times as large than that of 4s near the Fermi level, indicating that the transition process from 2p to 3d is dominant in the measured XAS. The most obvious difference in 3d is that the DOS of Py-Ni site is more intense than that of T-Ni site near the Fermi-level. Figure 3.5(b) is each site specific XAS spectra by reflecting the DOS dispersion in Fig. 3.5(a). The calculated XAS showed similar dispersion with the experimentally separated XAS. Thus the disentanglement of site selective XAS was reasonable. We succeeded in detecting a site specific electronic structure which is important for distinguishing the catalytic properties at an atomic level.

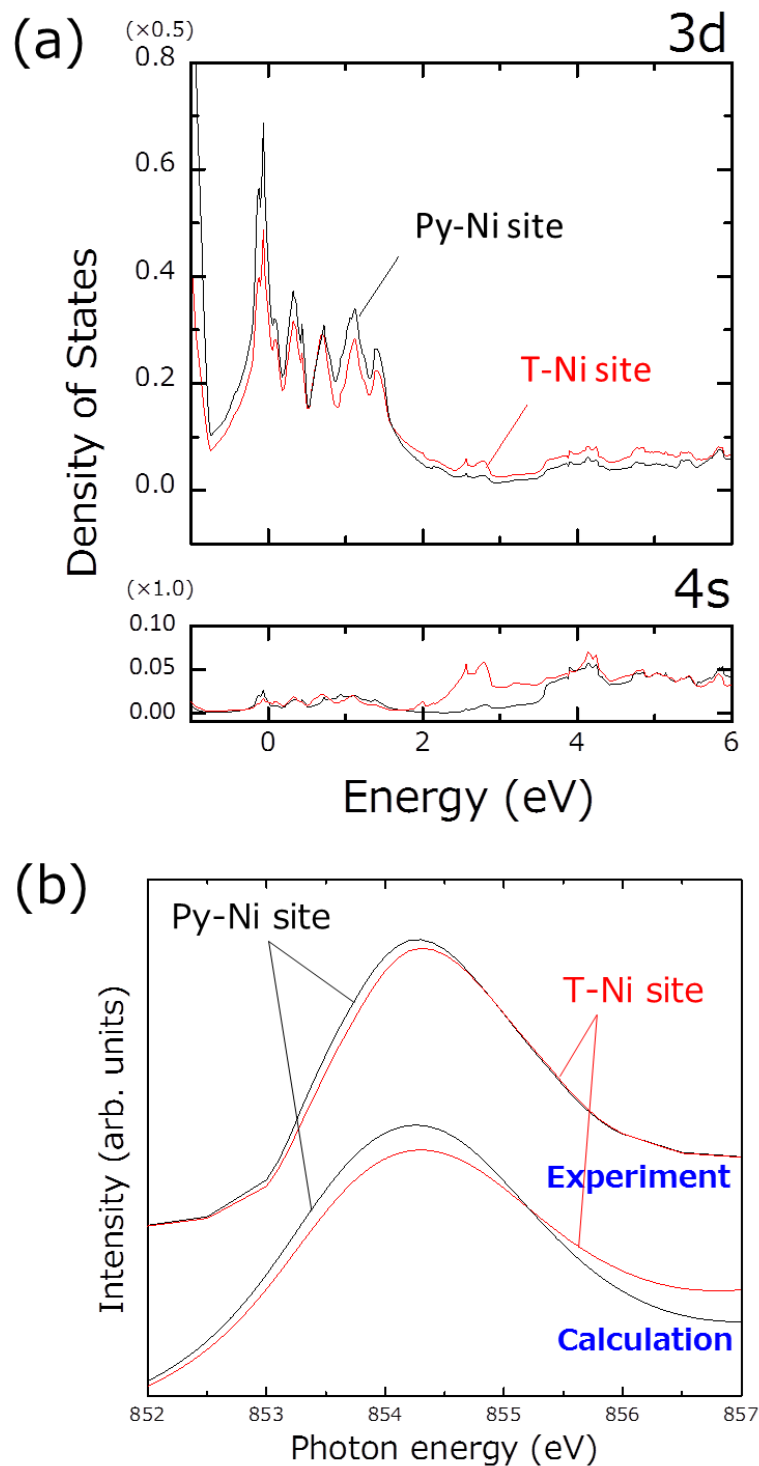


Fig. 3.5. (a) The calculated density of state for all orbitals by WIEN2k. Wave function was used for Argumented Plane Wave (APW)+local orbitals (lo) method to consider the local . 5000 kpoints was considered. The core hole was not considered because the shift in Ni 2p was observed in the fine XPS measurement. (b) The calculated XAS spectra for both pyramidal- and tetrahedral-Ni sites.

3.4 Conclusion

In conclusion, we have measured the Ni L_3 ($2p_{2/3}$) edge XAS spectrum of a $\text{Ni}_2\text{P}(10\bar{1}0)$ catalytic surface by collecting a series of Ni-LMM AIADs. The series of AIADs showed the unvaried structures for all the photon energies but the fine structure differences were observed by normalizing with that of the L_3 edge jump. On the lower and higher energies in XAS, a set of negative behavior of AIADs newly appeared. Also, the AIAD disappeared at the L_3 peak top. These facts strongly suggest that the local site contribution for the entire XAS, which corresponded to the relation between the atomic and electronic structures was successfully observed. Site selective XAS, which was collected from each Ni site characteristic FFP by means of photoelectron diffraction spectroscopy, showed that the Py-Ni site is more dominant near the Fermi-level than the T-Ni site. This analysis method has a possibility to clarify an active site at an atomic level by observing the differences before and after catalytic reactions.

References

- [1] S. T. Oyama. Novel catalysts for advanced hydroprocessing: transition metal phosphides. *J. Catal.* **216** (2003) 343–352.
- [2] S. T. Oyama and Y. K. Lee. The active site of nickel phosphide catalysts for the hydrodesulfurization of 4, 6-DMDBT. *J. Catal.* **258** (2008) 393–400.
- [3] K. K. Bando, T. Wada, T. Miyamoto, K. Miyazaki, S. Takakusagi, T. Gott, A. Yamaguchi, M. Nomura, S. Oyama and K. Asakura. Combined in situ analysis of Ni₂P/MCM-41 under hydrodesulfurization conditions—Simultaneous observation of QXAFS and FTIR—. *Journal of Physics: Conference Series* **190** (2009) 012158.
- [4] S. T. Oyama, T. Gott, K. Asakura, S. Takakusagi, K. Miyazaki, Y. Koike and K. K. Bando. In situ FTIR and XANES studies of thiophene hydrodesulfurization on Ni₂P/MCM-41. *J. Catal.* **268** (2009) 209–222.
- [5] T. Wada, K. K. Bando, T. Miyamoto, S. Takakusagi, S. T. Oyama and K. Asakura. Operando QEXAFS studies of Ni₂P during thiophene hydrodesulfurization: direct observation of Ni-S bond formation under reaction conditions. *Journal of Synchrotron Radiation* **19** (2012) 205–209.
- [6] T. Kawai, S. Sato, S. Suzuki, W. J. Chun, K. Asakura, K. K. Bando, T. Matsui, Y. Yoshimura, T. Kubota, Y. Okamoto, et al. In situ X-ray absorption fine structure studies on the structure of nickel phosphide catalyst supported on K-USY. *Chem. Lett.* **32** (2003) 956–957.

- [7] T. Wada, K. K. Bando, S. T. Oyama, T. Miyamoto, S. Takakusagi and K. Asakura. Operando Observation of Ni₂P Structural Changes during Catalytic Reaction: Effect of H₂S Pretreatment. *Chemistry Letters* **41** (2012) 1238–1240.
- [8] S. T. Oyama, Z. Haiyan, H. J. Freund, K. Asakura, R. Włodarczyk and M. Sierka. Unprecedented selectivity to the direct desulfurization (DDS) pathway in a highly active FeNi bimetallic phosphide catalyst. *J. Catal.* **285** (2012) 1–5.
- [9] C. S. Fadley, Y. Chen, R. E. Couch, H. Daimon, R. Denecke, J. D. Denlinger, H. Gallaway, Z. Hussain, A. P. Kaduwela, Y. J. Kim, et al. Diffraction and holography with photoelectrons and fluorescent X-rays. *Prog. Surf. Sci.* **54** (1997) 341–386.
- [10] H. Daimon. Stereoscopic Microscopy of Atomic Arrangement by Circularly Polarized-Light Photoelectron Diffraction. *Phys. Rev. Lett.* **86** (2001) 2034–2037.
- [11] W. Auwärter, K. T. J., T. Gerber and O. J. XPD and STM investigation of hexagonal boron nitride on Ni(111). *Surf. Sci.* **429** (1999) 229–236.
- [12] F. Matsui, T. Matsushita and H. Daimon. Photoelectron Diffraction and Holographic Reconstruction of Graphite. *J. Phys. Soc. Jpn.* **81** (2012) 114604.
- [13] Y. Kato, F. Matsui, T. Shimizu, H. Daimon, T. Matsushita, F. Z. Guo and T. Tsuno. Dopant-site effect in superconducting diamond (111) studied by atomic stereophotography. *Appl. Phys. Lett.* **91** (2007) 251914–251914.
- [14] F. Matsui, T. Matsushita, Y. Kato, M. Hashimoto, K. Inaji, F. Guo and H. Daimon. Atomic-layer resolved magnetic and electronic structure analysis of Ni thin film on a Cu (001) surface by diffraction spectroscopy. *Phys. Rev. Lett.* **100** (2008) 207201.

- [15] O. S. and N. Ohashi. Preparation of Ni₂P and Fe₂P single crystals by the floating-zone method. *J. Ceram. Soc. Japan* **121** (2013) 331–332.
- [16] D. Guo, Y. Nakagawa, H. Ariga, S. Suzuki, K. Kinoshita, T. Miyamoto, S. Takakusagi, K. Asakura, S. Otani and S. T. Oyama. STM studies on the reconstruction of the Ni₂P(10 $\bar{1}$ 0) surface. *Surf. Sci.* **604** (2010) 1347–1352.
- [17] Y. Saitoh, H. Kimura, Y. Suzuki, T. Nakatani, T. Matsushita, T. Muro, T. Miyahara, M. Fujisawa, K. Soda, S. Ueda, et al. Performance of a very high resolution soft x-ray beamline BL25SU with a twin-helical undulator at SPring-8. *Rev. Sci. Instrum.* **71** (2000) 3254–3259.
- [18] H. Daimon. New display-type analyzer for the energy and the angular distribution of charged particles. *Rev. Sci. Instrum.* **59** (1988) 545–549.
- [19] H. Daimon and S. Ino. Improvement of the spherical mirror analyzer. *Rev. Sci. Instrum.* **61** (1990) 57–60.
- [20] M. Kotsugi, Y. Miyatake, K. Enomoto, K. Fukumoto, A. Kobayashi, T. Nakatani, Y. Saitoh, T. Matsushita, S. Imada, T. Furuhashi, et al. Construction of two-dimensional photoelectron spectrometer at SPring-8. *Nucl. Instrum. Methods Phys. Res., Sect. A* **467** (2001) 1493–1496.
- [21] F. Matsui, H. Daimon, F. Guo and T. Matsushita. Visualization of graphite atomic arrangement by stereo atomscope. *Appl. Phys. Lett.* **85** (2004) 3737–3739.
- [22] F. Matsui, T. Matsushita, Y. Kato, F. Guo and H. Daimon. Site-specific orbital angular

- momentum analysis of graphite valence electron using photoelectron forward focusing peaks. *J. Phys. Soc. Jpn.* **76** (2007).
- [23] F. Matsui, T. Matsushita and H. Daimon. Atomic-layer-resolved analysis of surface magnetism by diffraction spectroscopy. *J. Electron Spectrosc. Relat. Phenom.* **181** (2010) 150–153.
- [24] T. Matsushita, F. Guo, F. Matsui, Y. Kato and H. Daimon. Three-dimensional atomic-arrangement reconstruction from an Auger-electron hologram. *Phys. Rev. B* **75** (2007) 085419.
- [25] K. Inaji, F. Matsui, Y. Kato, C. Sakai, T. Narikawa, T. Matsushita, F. Guo and H. Daimon. Circular dichroism of forward focusing peaks and diffraction rings in 2π steradian Si 2p photoelectron pattern. *Appl. Surf. Sci.* **254** (2008) 7549–7552.
- [26] S. Rundqvist. X-ray investigations of Mn_3P , Mn_2P and Ni_2P . *Acta Chem. Scand.* **16** (1962) 8–16.
- [27] T. Matsushita, F. Matsui, H. Daimon and K. Hayashi. Photoelectron holography with improved image reconstruction. *J. Electron Spectrosc. Relat. Phenom.* **178** (2010) 195–220.

Chapter 4. Surface atomic structure and catalytic property of Fe modified Ni₂P surface by photoelectron diffraction

A bimetallic FeNi phosphide catalyst, which has higher catalytic activity for a direct desulfurization reaction, was duplicated by modifying Fe on a single-crystalline Ni₂P surface. The surface and catalytic properties by installing Fe were characterized by photoelectron diffraction and spectroscopy. Element specific photoelectron intensity angular distributions (PIADs) clarified the selective displacement of Fe into the Ni site while maintaining the Ni₂P crystalline structure. The surface termination structure was reconstructed through simulation, and the result attributed the surface termination structure as a hubble B' registry. This Fe modified Ni₂P surface showed the activity for adsorbing nitrogen mono-oxide which was not observed on the clean Ni₂P surface.

4.1 Introduction

Surface properties of transitional metal phosphides (TMPs) have been attracting much attention as a new catalyst group for hydrodesulfurization (HDS) and hydrodenitrogenation (HDN) reactions. Among the TMPs studied so far, Ni₂P is known to have the highest activity. Recent activity in the Ni₂P study is revealing the catalytic behavior of a bimetallic Ni₂P modified with several kinds of metals by the ligand and ensemble effects. Oyama *et al.* reported that a bimetallic NiFe phosphide catalyst, with a Ni/Fe ratio of 1:1, shows an unprecedented selectivity of 85% for direct desulfurization whereas the Ni₂P has a less selectivity of only 12%. Their x-ray absorption fine structure (XAFS) analysis has revealed the site occupancy of Fe in the NiFe phosphide nano particle supported on SiO₂. However, the Ni₂P has a complex structure with more than two Ni-P distances with two independent Ni sites and it is difficult to obtain the precise relation between the structure and catalytic activities only by XAFS.

Surface science studies using a single crystalline surface as a model catalyst have been revealing the relation between the surface structure and catalytic properties. Previous scanning tunneling microscope (STM) [1–4] and low energy electron diffraction (LEED) [1, 2, 4–6] found the long range periodicity of inactive P atom terminations on a single-crystalline Ni₂P surface. However, the former analyses do not give element and site specific information which is important for clarifying the catalytic mechanism.

A photoelectron from a localized core level is an excellent element selective probe for surface structure analysis [7]. Forward focusing peaks (FFPs) appearing in the photoelectron intensity angular distribution (PIAD) indicate the directions of surrounding atoms seen from

the photoelectron emitter atom [8]. The atomic distance between the emitter and scatterer atoms can be deduced from the circular-dichroism shift of FFP positions [8–10] as well as from the opening angles of diffraction rings (DRs) appearing around the FFP [10, 11]. Kato *et al.* succeeded in determining the B dopant site on a diamond crystal for superconductivity, implying the application for the diluted material less than several percentages [12]. We have also achieved the disentanglement into the layer-resolved C 1s PIADs from the formation stages of graphene on 4H-SiC(0001) in chapter 1. As mentioned above, it is possible for photoelectron diffraction (PED) to clarify the site and element selective surface structure.

In this study, we have duplicated the NiFe phosphide by modifying Fe on a single crystalline Ni₂P surface. The installation site of Fe onto the Ni₂P surface was characterized by a similar approach. The use of NO chemisorption indicated the surface reactivity between the Fe-modified and clean Ni₂P surfaces.

4.2 Experimental details

A single crystalline $\text{Ni}_2\text{P}(10\bar{1}0)$ surface was used as a sample [13]. A $(10\bar{1}0)$ surface terminates with the Ni/P stoichiometric composition of bulky 2:1, is suitable for studying the bulky chemical feature. The sample was cut with a size of $0.8\times 4\times 1$ mm and mechanically polished to a mirror finishing. The sample surface was cleaned by Ar^+ sputtering at 2.5 keV (current: $1\ \mu\text{A}$, time: 30 min, Ar pressure: 1×10^{-3} Pa) and annealing at 350°C by direct current injection repeatedly after transferring into an ultra-high vacuum chamber with a base pressure of less than 3×10^{-8} Pa. The annealing temperature was monitored by a K-type thermo-coupling directly attached to the sample back. The surface structure was characterized by reflection high-energy electron diffraction (RHEED). A sharp (1×1) structure coming from the clean bulk lattice was confirmed. The chemical composition was observed by XPS. A small amount impurities come from the C and O remaining on the surface after the cleaning process, but it will not greatly affect the chemical feature.

The Fe modified Ni_2P surface was made by depositing Fe (purity: 99.9%) at room temperature onto the clean Ni_2P surface using a fixed rate evaporator. Half of the sample surface was covered with the shutter, indicating both Fe-deposited and clean Ni_2P surface areas on the same sample. Therefore, the Fe modification effect can be discussed in the same reaction condition and in a short experiment time. The chemisorption of NO dosed at 1000 Langmuir (1×10^{-3} Pa, 100 sec) on the sample surface at room temperature was used. NO is frequently used to count the surface metal sites in TM phosphide which is active during HDS reactions. Surface adsorbates coming from NO were detected by XPS.

All experiments were performed at the circularly-polarized soft x-ray beamline BL25SU

at SPring-8 in Japan. PIAD from the sample at a specific kinetic energy is most efficiently measured using a two-dimensional display-type spherical mirror analyzer (DIANA) [14–16]. The acceptance angle of the analyzer was $\pm 60^\circ$. Light was incident from the direction 45° inclined from the analyzer center. The emission angle θ dependence from 0 to 90° relative to the surface normal is measured simultaneously. A 2π steradian PIAD was obtained by scanning the sample azimuth for 360° [17, 18]. The helicity (σ_\pm) of monochromatized circularly-polarized soft X-ray was reversed by switching the path of storage ring electrons in twin helical undulators at 0.1 Hz [19]. The photon energy resolution was better than 100 meV. The total acquisition time for a pair of 2π -steradian PIADs excited by σ_+ and σ_- helicity lights was 2.5 hr. All data was measured at room temperature. The energy window width of DIANA was set to 2 eV for spectroscopy measurements, while it was set to 15 eV for PIAD measurements. This was done to avoid the signal lapping from Fe $3p$ and Ni $3p$ core-level. All PIADs were obtained with a photoelectron kinetic energy of 550 eV, and displayed in azimuth equidistant projection.

4.3 Results and discussion

Figure 4.1(a) shows the bulk Ni_2P atomic arrangement along the $[0001]$ direction [20]. Ni_2P belongs to space group $P_{\bar{6}2m}$ of hexagonal symmetry with $a=b=5.859 \text{ \AA}$ and $c=3.382 \text{ \AA}$. In the bulk Ni_2P crystal, two kinds of stoichiometric layers, namely Ni_3P and Ni_3P_2 layers stacked alternatively along the $[0001]$ direction, covalently bonded to each other. Ni has two kinds of atomic sites which are surrounded by the tetrahedral and pyramidal structure of P atoms in Ni_3P_2 and Ni_3P layers, respectively. As shown in Fig. 4.1(b), there are two possible terminations for a $(10\bar{1}0)$ surface denoted as A and B planes. Surface A is flat while surface B has a small periodic ripple, originating from the arrangement of the Ni atoms. Surface B gives two equivalent B and B' planes which are a mirror symmetry of each other. A, B and B' planes are stacked in the sequence of ABB'ABB'.

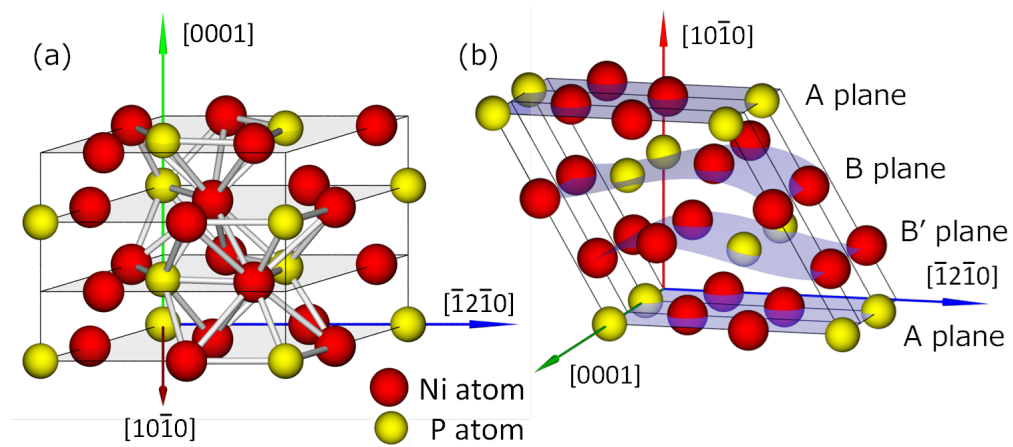


Fig. 4.1. (a) The crystalline structure of $\text{Ni}_2\text{P}(0001)$. Red and yellow spheres indicate Ni and P atoms, respectively. Green, red and blue arrows indicate $[0001]$, $[10\bar{1}0]$, $[\bar{1}2\bar{1}0]$ directions. Ni_3P_2 and Ni_3P terminations stack alternatively along the $[0001]$ direction. (b) Same with (a) but for the $(10\bar{1}0)$ surface which used in this study. Flat A plane, hubbly B and B' planes stack alternatively along the $[10\bar{1}0]$ direction. The surface terminated plane is unknown.

Figures 4.2(a), 4.2(b) and 4.2(c) show the set of P 2p, Ni 3p and Fe 3p 2π -steradian PIADs from the Fe-modified Ni₂P (10 $\bar{1}$ 0) surface, respectively. Two PIADs using σ_+ and σ_- helicity light were superimposed to eliminate the circular dichroism of the FFP rotation in order to identify the exact orientation. The target grids of azimuth and polar angle every 30° were shown in each PIAD. Note that the FFP positions, diffraction patterns and their circular dichroism from Ni 3p and P 2p PIADs were basically similar before and after Fe modification. Therefore, Fe modification did not make the crystalline structure change. In both Fig. 4.2(a) and 4.2(b), a Kikuchi-band like structure, which enhanced the bulky atomic configuration, was seen along the (0001) plane. The mirror symmetric structure was seen with the boundary of a (0001) plane. In Fig. 4.2(c), the obvious contrast, which strongly suggests the epitaxial growth of a Fe structure on a Ni₂P surface, was seen. The pattern symmetry was basically similar to that of Ni 3p and P 2p, indicating that the Fe structure followed the Ni₂P as a template. To evaluate the detail similarities for each element specific PIAD, a signal intensity profile along the (0001) plane was shown in Fig. 4.2(d). Fe and Ni profiles showed similar features at each direction, while that of P did not have intensity around the [1 $\bar{1}$ 00] and [01 $\bar{1}$ 0] directions. Therefore, the selective displacement of Fe onto a Ni site, that is, the growth of a Fe₂P thin film, was confirmed on the Ni₂P surface.

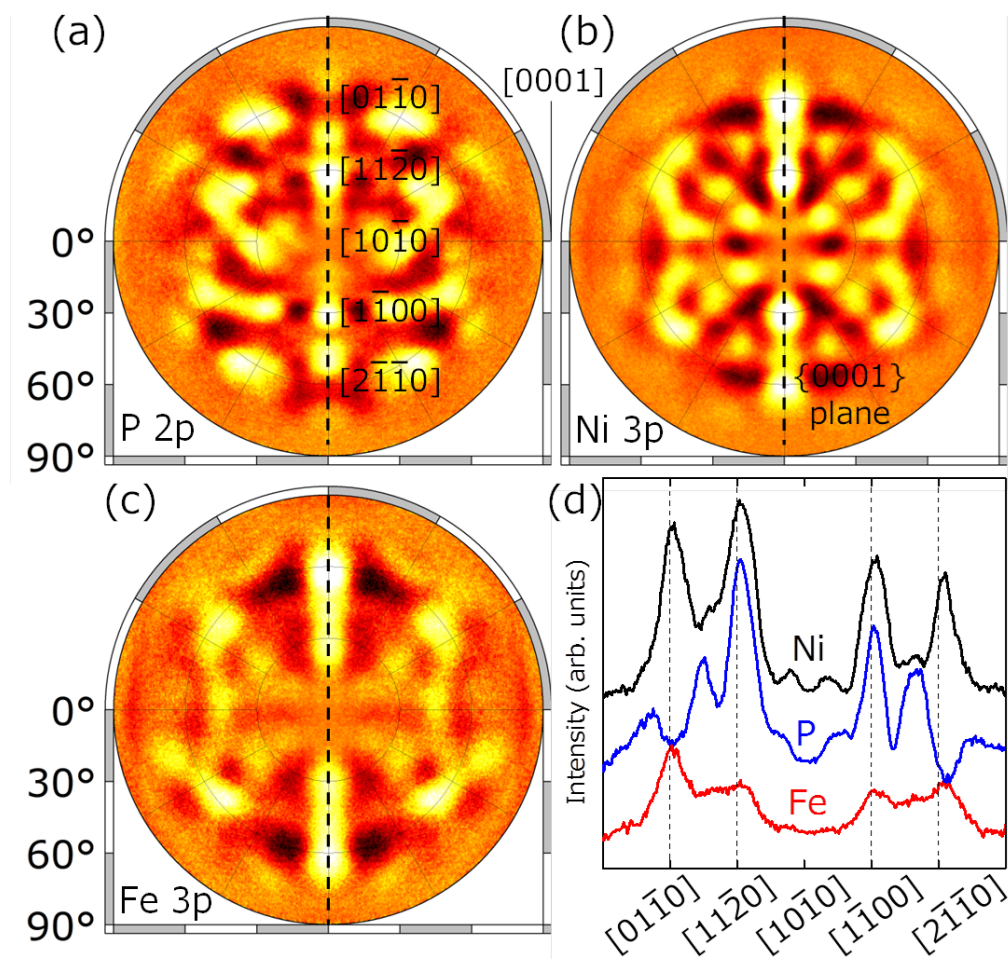


Fig. 4.2. (a), (b) and (c) The set of measured P 2p, Ni 3p and Fe 3p 2π -steradian photoelectron intensity angular distributions (PIADs) from a Fe-modified Ni_2P (10 $\bar{1}0$) surface, respectively. The vertical dotted line indicates the (0001) plane. (d) Signal intensity profile along the (0001) plane in Fig. 4.1(a), 4.1(b) and 4.1(c).

The film thickness of Fe₂P was estimated from the intensity ratio of Fe 3p versus Ni 3p in the XPS spectrum (as shown in Fig. 4.4(a)). Here, the simple structure model, a Fe₂P thin film covers all the Ni₂P surface, was assumed because the epitaxial growth of Fe₂P was confirmed by PIAD analysis. The Fe 3p/Ni 3p value of 0.24 gave a film thickness of 0.33 nm which corresponds to about 3ML of Ni₂P(10 $\bar{1}$ 0) surface structure. In this case, three kinds of stacking registry, ABB', B'AB and BB'A, were proposed in 3ML of the surface termination structure. As shown in Fig. 4.3(a), 4.3(b) and 4.3(c), the measured Fe 3p PIAD in Fig. 4.2(c) was compared with the simulated PIADs for 3 ML of each stacking registry. Every PIAD showed a similar structure to that of the bulky Ni 3p PIAD in Fig. 4.2(b) but the detail distributions were characterized by the signal intensity profile in Fig. 4.3(d). ABB' and B'AB registries had a similar distribution to that of the measured Fe 3p PIAD while BB'A had a completely different shape distribution. The inset in Fig. 4.3(d) indicates the R-factor value for each stacking registry by two-dimensional pattern of root mean square error calculations. B'AB showed the best value at 0.46 while ABB' and BB'A were 0.97 and 0.73, respectively. Therefore, the surface termination was determined as a B'AB registry.

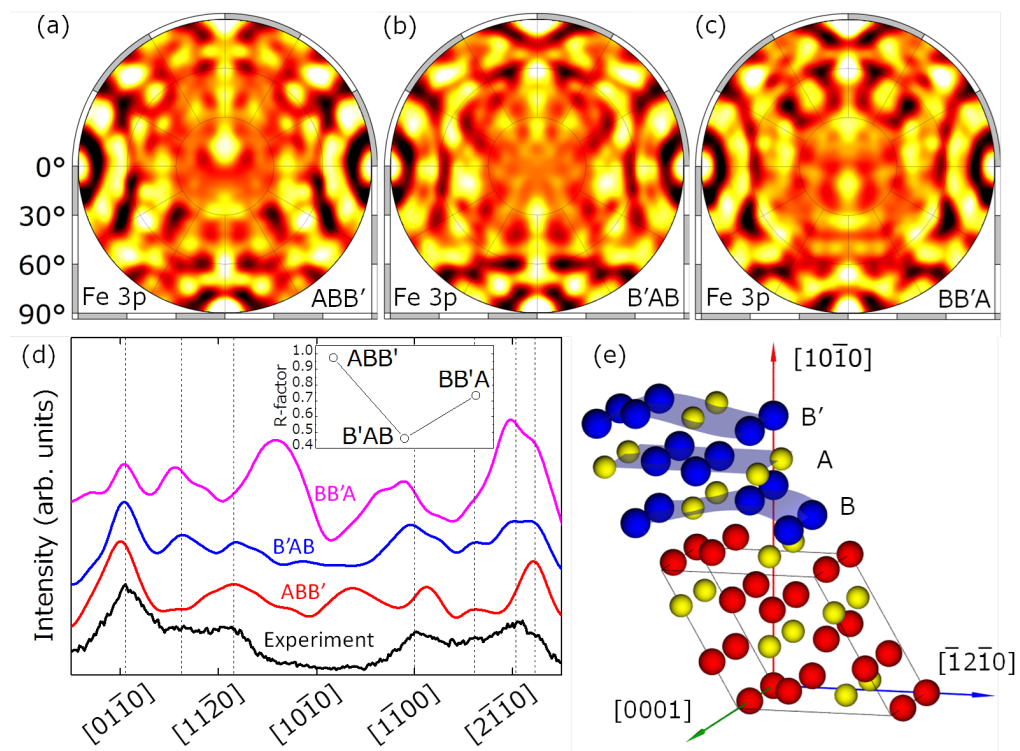


Fig. 4.3. (a), (b) and (c) The set of simulated Fe 3p 2π -steradian PIADs from the expected termination model of ABB', B'AB and BB'A registries. (d) The signal intensity profile along the (0001) plane in Fig. 4.2(d), Fig. 4.3(a), 4.3(b) and 4.3(c). The inset indicate the R-factor value for each simulated ABB', B'AB and BB'A registry. (e) The expected termination structure model of Fe_2P on the Ni_2P ($10\bar{1}0$) surface.

To evaluate the surface reactivity between the Fe-deposited and clean Ni₂P surfaces, the chemisorption of NO, which was selectively bound to the surface metal, was used. Topsøe *et al.* reported that NO adsorption is responsible for the promotion of the HDS activity [21]. Figure 4.4(a) and 4.4(b) show the wide area XPS spectra taken before and after dosing with NO on the Fe-deposited and clean Ni₂P surfaces. The obvious increasing of N 1s and O 1s intensities coming from NO molecules were confirmed on the Fe-deposited surface whereas it was not seen on the clean surface. However, the intensity of O 1s was twice as large than that of N 1s, implying that dosed NO was dissociated on the surface and the part of N was desorbed. This result insists that the Fe modification relates with the high reactivity. In Fig. 4.4(b), the detailed XPS spectra for P 2p, Ni 3p and Fe 3p are shown. In the P 2p spectrum, a slight shoulder structure assigned to the P-O bonding between the surface remained O and the terminated P was seen before dosing with NO. This shoulder structure increased after NO dosing. Thus the surface reactant with P atom is considered as O dissociated from NO molecules. On the other hand, the core-level shift and the peak shape differences were not observed in the Ni 3p spectra, implying that Ni was not reacted with NO due to the covering of Fe₂P thin film on the Ni₂P surface. Fe 3p was shifted to a higher binding energy of 0.6 eV due to the oxidation by dissociated O from NO. Because the surface component is majority in the whole amount of Fe, most of Fe was reacted with NO. As mentioned above, the active structure was determined as the epitaxial grown Fe₂P.

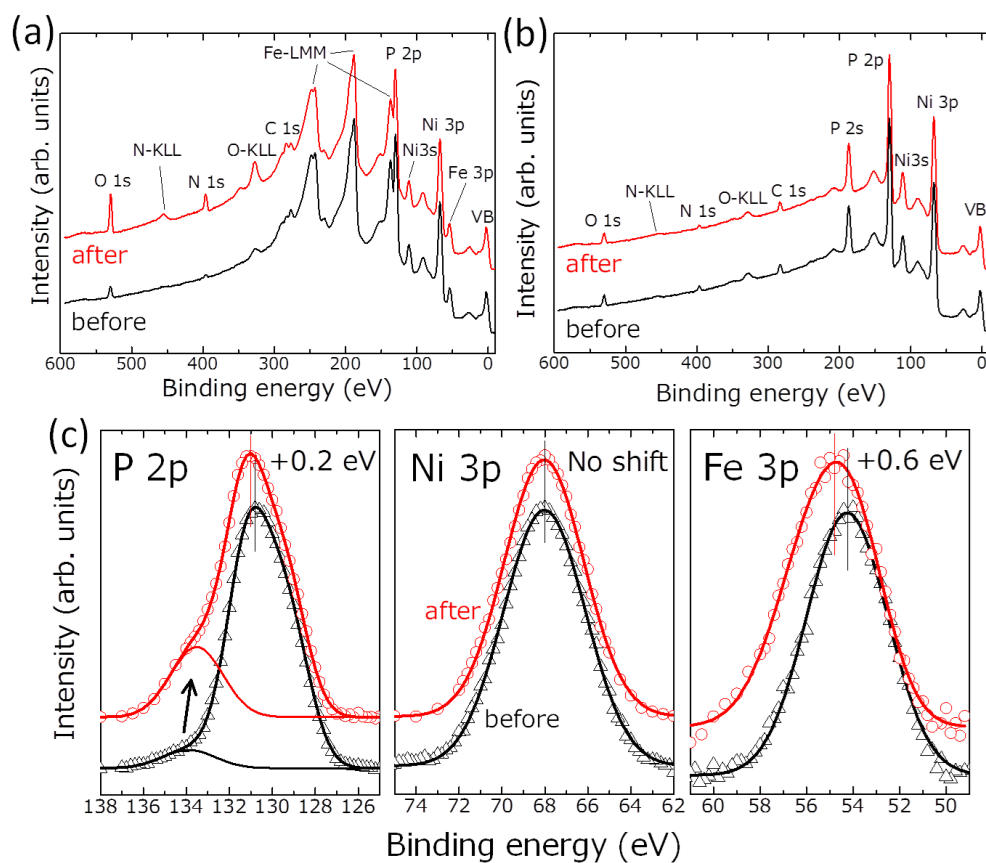


Fig. 4.4. (a) and (b) X-ray photoelectron spectroscopy (XPS) spectra before and after dosing with NO on the Fe-modified and clean Ni₂P surfaces. (c) The fine P 2p, Ni 3p and Fe 3p XPS spectra before and after dosing with NO on the Fe-modified Ni₂P surface. Black and red opened marks are the measured data points before and after dosing with NO. Solid lines are the Gauss-fitting results.

4.4 Conclusion

In conclusion, we have duplicated the higher catalytic FeNi phosphide by modifying Fe on a single-crystalline Ni₂P surface and characterized the Fe installation site onto a Ni₂P surface. Element specific PIAD clarified that Fe was selectively displaced onto the Ni site while maintaining the Ni₂P crystalline structure. The film thickness of the Fe structure was determined as 3.3Å. This corresponded to roughly 3ML by an angle-resolved XPS analysis. Among the three kinds of surface termination combinations, the simulated PIAD revealed that the (0001) plane signal intensity profile from the B'AB registry showed good agreement with the experimental distribution. The Fe-modified surface reacted with NO whereas the clear Ni₂P surface did not. The deposition of different kinds of metal made the active metal termination and was the key to improving the catalytic properties.

References

- [1] G. Moula, S. Suzuki, W. J. Chun, S. Otani, S. T. Oyama and K. Asakura. The first atomic-scale observation of a Ni₂P(0001) single crystal surface. *Chem. Lett.* **35** (2006) 90–91.
- [2] K. Kinoshita, G. H. Simon, T. König, M. Heyde, H. J. Freund, Y. Nakagawa, S. Suzuki, W. J. Chun, S. T. Oyama, S. Otani and K. Asakura. A Scanning Tunneling Microscopy Observation of ($\sqrt{3} \times \sqrt{3}$)R30° Reconstructed Ni₂P(0001). *Jpn. J. Appl. Phys.* **47** (2008) 6088.
- [3] S. Suzuki, G. M. Moula, T. Miyamoto, Y. Nakagawa, K. Kinoshita, K. Asakura, S. T. Oyama and S. Otani. Scanning tunneling microscopy and photoemission electron microscopy studies on single crystal Ni₂P surfaces. *J. Nanosci. Nanotechnol.* **9** (2009) 195–201.
- [4] D. Guo, Y. Nakagawa, H. Ariga, S. Suzuki, K. Kinoshita, T. Miyamoto, S. Takakusagi, K. Asakura, S. Otani and S. T. Oyama. STM studies on the reconstruction of the Ni₂P(10 $\bar{1}$ 0) surface. *Surf. Sci.* **604** (2010) 1347–1352.
- [5] D. Kanama, S. T. Oyama, S. Otani and D. F. Cox. Photoemission and LEED characterization of Ni₂P(0001). *Surf. Sci.* **552** (2004) 8–16.
- [6] A. B. Hernandez, H. Ariga, S. Takakusagi, K. Kinoshita, S. Suzuki, S. Otani, S. T. Oyama and K. Asakura. Dynamical LEED analysis of Ni₂P(0001)-1 \times 1: Evidence for P-covered surface structure. *Chem. Phys. Lett.* **513** (2011) 48–52.

- [7] C. S. Fadley, Y. Chen, R. E. Couch, H. Daimon, R. Denecke, J. D. Denlinger, H. Gallaway, Z. Hussain, A. P. Kaduwela, Y. J. Kim, et al. Diffraction and holography with photoelectrons and fluorescent X-rays. *Prog. Surf. Sci.* **54** (1997) 341–386.
- [8] H. Daimon. Stereoscopic Microscopy of Atomic Arrangement by Circularly Polarized-Light Photoelectron Diffraction. *Phys. Rev. Lett.* **86** (2001) 2034–2037.
- [9] F. Matsui, N. Nishikayama, N. Maejima, H. Matsui, K. Goto, M. Hashimoto, T. Hatayama, T. Matsushita, Y. Kato, S. Tanaka and H. Daimon. Site-Specific Stereograph of SiC (0001) Surface by Inverse Matrix Method. *J. Phys. Soc. Jpn.* **80** (2011) 013601.
- [10] F. Matsui, T. Matsushita and H. Daimon. Photoelectron Diffraction and Holographic Reconstruction of Graphite. *J. Phys. Soc. Jpn.* **81** (2012) 114604.
- [11] W. Auwärter, K. T. J., T. Gerber and O. J. XPD and STM investigation of hexagonal boron nitride on Ni(111). *Surf. Sci.* **429** (1999) 229–236.
- [12] Y. Kato, F. Matsui, T. Shimizu, H. Daimon, T. Matsushita, F. Z. Guo and T. Tsuno. Dopant-site effect in superconducting diamond (111) studied by atomic stereophotography. *Appl. Phys. Lett.* **91** (2007) 251914–251914.
- [13] O. Shigeki and O. Naoki. Preparation of Ni₂P and Fe₂P single crystals by the floating-zone method. *J. Ceram. Soc. Japan* **121** (2013) 331–332.
- [14] H. Daimon. New display-type analyzer for the energy and the angular distribution of charged particles. *Rev. Sci. Instrum.* **59** (1988) 545–549.

- [15] H. Daimon and S. Ino. Improvement of the spherical mirror analyzer. *Rev. Sci. Instrum.* **61** (1990) 57–60.
- [16] M. Kotsugi, Y. Miyatake, K. Enomoto, K. Fukumoto, A. Kobayashi, T. Nakatani, Y. Saitoh, T. Matsushita, S. Imada, T. Furuhashi, et al. Construction of two-dimensional photoelectron spectrometer at SPring-8. *Nucl. Instrum. Methods Phys. Res., Sect. A* **467** (2001) 1493–1496.
- [17] T. Matsushita, F. Guo, F. Matsui, Y. Kato and H. Daimon. Three-dimensional atomic-arrangement reconstruction from an Auger-electron hologram. *Phys. Rev. B* **75** (2007) 085419.
- [18] K. Inaji, F. Matsui, Y. Kato, C. Sakai, T. Narikawa, T. Matsushita, F. Guo and H. Daimon. Circular dichroism of forward focusing peaks and diffraction rings in 2π steradian Si 2p photoelectron pattern. *Appl. Surf. Sci.* **254** (2008) 7549–7552.
- [19] T. Muro, T. Nakamura, T. Matsushita, H. Kimura, T. Nakatani, T. Hirono, T. Kudo, K. Kobayashi, Y. Saitoh, M. Takeuchi, T. Hara, K. Shirasawa and H. Kitamura. Circular dichroism measurement of soft X-ray absorption using helicity modulation of helical undulator radiation. *J. Electron Spectrosc. Relat. Phenom.* **144** (2005) 1101–1103.
- [20] S. Rundqvist. X-ray investigations of Mn_3P , Mn_2P and Ni_2P . *Acta Chem. Scand.* **16** (1962) 8–16.
- [21] N. Y. Topsøe and H. Topsøe. NO chemisorption as a probe of the active precursors in Co-Mo/ Al_2O_3 catalysts. *J. Catal.* **77** (1982) 293–296.

Chapter 5. Atomic structure and catalytic activity of W-Ni₂P surface alloy by photoelectron diffraction and spectroscopy

The surface alloying is the important topics in Ni₂P study which is expected from next generation hydrodesulfurization and hydrodenitrogenation catalyst. The atomic structure and catalytic properties of a single crystalline Ni₂P surface modified with W (W-Ni₂P) was investigated by photoelectron diffraction (PED) and spectroscopy. PED is an element and site selective surface structure analysis method, and enables observation of three-dimensional atomic configurations of the surface local structure. The selective replacement of W to the Ni site in a Ni₂P crystal was clarified by PED. Chemical reactivity for NO molecules of the W-Ni₂P and the clean Ni₂P surfaces were compared. On the clean Ni₂P surface, the NO adsorption did not occur, whereas W-Ni₂P surface showed remarkable activity for NO adsorption.

5.1 Introduction

Development of new series of catalytic materials is important for the improvement of processes for the conversion of energy, the production of chemicals, and the elimination of pollutants. Removal of the sulfide and nitride content in natural petroleum feedstock is urgent issue in the refining industry [1]. The surface properties of transitional metal phosphides (TMPs) have attracted much attention as a new catalyst group for hydrodenitrogenation (HDS) and hydrodenitrogenation (HDN) reactions [2]. Among the TMPs studied so far, Ni_2P has been found to have the highest activity for HDS and HDN reactions [2]. Current studies in Ni_2P have been revealing the catalytic behavior of bimetallic Ni_2P modified with Mo [3, 4], Co [5, 6] and Fe [7–9] to explore other phosphide catalysts that can be controlled by alloying. However, these bimetallic phosphides have not shown enhanced activity until now. Here, we focused on a W modification effect, since early work showed that Ni_2P and WP have the first and the second highest HDS and HDN activities in TMPs [2]. Also, Kopyscinski *et al.* suggested that the molar ratio of Ni:W:P=1:1:2 is important for showing the high performance in HDN reaction because Ni and W compete for P and inactive W structures are formed [10]. Therefore, local atomic structure and composition analyses are necessary for clarifying the active phase of a Ni_2P surface alloy at an atomic level.

Surface science studies using a single crystalline sample have been conducted to elucidate the relation between the surface atomic structure and catalytic properties. Previous scanning tunneling microscope (STM) [11–14] and low energy electron diffraction (LEED) [11, 12, 14–16] studies observed a long range periodicity of terminated P atoms on a single crystalline Ni_2P surface. However, the former analyses do not give a three-dimensional

atomic configuration with element and site selectivity.

A photoelectron from a localized core-level is an excellent element selective probe for surface structure analysis [17]. Forward focusing peaks (FFPs) appearing in the photoelectron intensity angular distribution (PIAD) indicate the directions of surrounding atoms seen from the photoelectron emitter atom [18]. The atomic distance between the emitter and scatterer atoms can be deduced from the circular-dichroism shift of FFP position [18–20] as well as from the opening angles of diffraction rings (DRs) appearing around the FFP [20, 21]. Kato *et al.* succeeded in determining the B dopant site in a superconductive diamond crystal, and showed an ability to analyze dilute species less than two percent [22].

In this study, we have characterized a W-modified Ni₂P surface (W-Ni₂P) by PED and x-ray photoelectron spectroscopy (XPS). Element specific PIADs clarified the atomic site of W in the Ni₂P crystal. Angle-resolved XPS estimated the thickness of the W related structure and the substituted ratio of W onto the Ni site. Furthermore, the surface reactivity of both the W-modified and clean Ni₂P surfaces were evaluated by NO adsorption.

5.2 Experimental details

A single crystalline $\text{Ni}_2\text{P}(10\bar{1}0)$ surface was used as the substrate [23]. This surface has a stoichiometric composition of $\text{Ni}/\text{P}=2$ which is same as that of bulk, and was suitable for studying the bulky chemical property [14]. The sample size was $5\times 10\times 1\text{ mm}^3$. The surface was mechanically polished to a mirror finishing and was cleaned by Ar^+ sputtering at 2.5 keV (current: $1\text{ }\mu\text{A}$, time: 30 min, Ar pressure: $1\times 10^{-3}\text{ Pa}$) and annealing at 350°C by direct current injection repeatedly after transferring into an ultra-high vacuum below $3\times 10^{-8}\text{ Pa}$ [14]. The annealing temperature was monitored by a K-type thermo-couple. The surface structure was determined by reflection high-energy electron diffraction (RHEED). A sharp (1×1) structure coming from the clean surface was confirmed. The chemical composition of the sample surface was observed by XPS.

The W- Ni_2P surface was prepared by depositing W on a clean Ni_2P surface under H_2 atmosphere with a pressure of $3\times 10^{-3}\text{ Pa}$. W filament with $\phi=0.2\text{ mm}$ and length of 200 mm was heated around 2000°C by direct current injection and set less than 10 mm over the sample for 10 min. This preparation was originally intended to reduce the Ni_2P surface by dissociated atomic hydrogen. However, the unexpected W deposition was confirmed by XPS measurement (see in Fig. 4.3(a)). The W- Ni_2P surface kept the sharp (1×1) RHEED pattern, indicating that W-modified layers were epitaxially formed on the Ni_2P surface. 1000 Langmuir ($3\times 10^{-3}\text{ Pa}$, 100 sec) NO molecules were dosed at room temperature to compare the chemical reactivity between the W- Ni_2P and the clean Ni_2P surfaces. The NO adsorbate coverage on the surface was evaluated by XPS.

PIAD from the sample at a specific kinetic energy was most efficiently measured using

a two-dimensional display-type spherical mirror analyzer (DIANA) which was installed at the circularly-polarized soft x-ray beamline BL25SU at SPring-8 in Japan. [24–26] A two-dimensional angular distribution snapshot of a specific kinetic energy electron can be measured. [18, 22, 27–30] The acceptance angle of the analyzer was $\pm 60^\circ$. Light was incident from the direction 45° inclined from the analyzer center. The emission angle θ dependence from 0 to 90° relative to the surface normal is measured simultaneously. A 2π steradian PIAD was obtained by scanning of the sample azimuth for 360° . [31, 32] The helicity (σ_\pm) of monochromatized circularly-polarized soft X-ray was altered by switching the path of storage ring electrons in twin helical undulators at 0.1 Hz. [33] The total acquisition time for the pair of 2π -steradian PIADs excited by σ_+ and σ_- helicity lights was 2.5 hr. All data was measured at room temperature. The energy window width of DIANA was set to 1 eV for spectroscopy measurements, while it was set to 30 eV for PIAD measurements, to achieve the best energy and angular resolution, respectively. All PIADs were obtained with a photoelectron kinetic energy of 600 eV, and displayed in azimuth equidistant projection.

5.3 Results and discussion

Figure 5.1(a) shows the crystalline structure of Ni_2P . Ni_2P belongs to the space group $\text{P}\bar{6}_2\text{m}$ of hexagonal symmetry with $a=b=0.586$ nm and $c=0.338$ nm [34]. In the bulk, two kinds of stoichiometric layers, namely Ni_3P and Ni_3P_2 layers, stack alternatively along the $[0001]$ direction. The blue colored rectangle in Fig. 5.1(a) indicates the $\{10\bar{1}0\}$ plane which was used in this study. The $(10\bar{1}0)$ surface has a mirror symmetric structure with respect to the $\{0001\}$ plane. Ni has two kinds of atomic sites which are surrounded by tetrahedral and pyramidal P structures in the Ni_3P_2 and Ni_3P layers, respectively. Since these tetrahedral and pyramidal Ni sites rotate by 120° in each other, six kinds of photoelectron emitter sites (Ni1-6) are expected as shown in Fig. 5.1(b). P has three kinds of photoelectron emitter sites: P1 and P2 sites in Ni_3P_2 layer and P3 site in Ni_3P layer, respectively.

Figures 5.1(c) and 5.1(d) show the set of 2π -steradian Ni 3p and P 2p PIADs from the clean $\text{Ni}_2\text{P}(10\bar{1}0)$ surface. Two PIADs using σ_+ and σ_- helicity light were averaged to eliminated the circular dichroism of FFP rotation in order to identify the exact orientation of FFP. The different structures appeared in each PIAD owing to the different surrounding atomic configuration for each atomic site. The left and right horizontal directions correspond to the $[0001]$ and $[000\bar{1}]$, respectively. Mirror symmetric structure with respect to the $\{0001\}$ plane was observed. A Kikuchi-band-like feature, which originated from the bulk atomic arrangement, was observed along the projection of $\{0001\}$ plane. Each colored dots along the $\{0001\}$ plane corresponds to the direction shown in Fig. 5.1(b). In the P 2p PIAD shown in Fig. 5.1(d), the additional Kikuchi-band-like features present were not observed in Fig. 5.1(c). DR, which corresponds to the bond between the P3 atom and the first neighboring

Ni5 atom in Ni₃P layer, was observed along the $[11\bar{2}0]$ direction shown with dotted line. The opening angle of DR was distributed of $44\pm 2.2^\circ$. The interatomic distance was estimated as 0.24 ± 0.03 nm which is within error range of the ideal 0.24 nm.

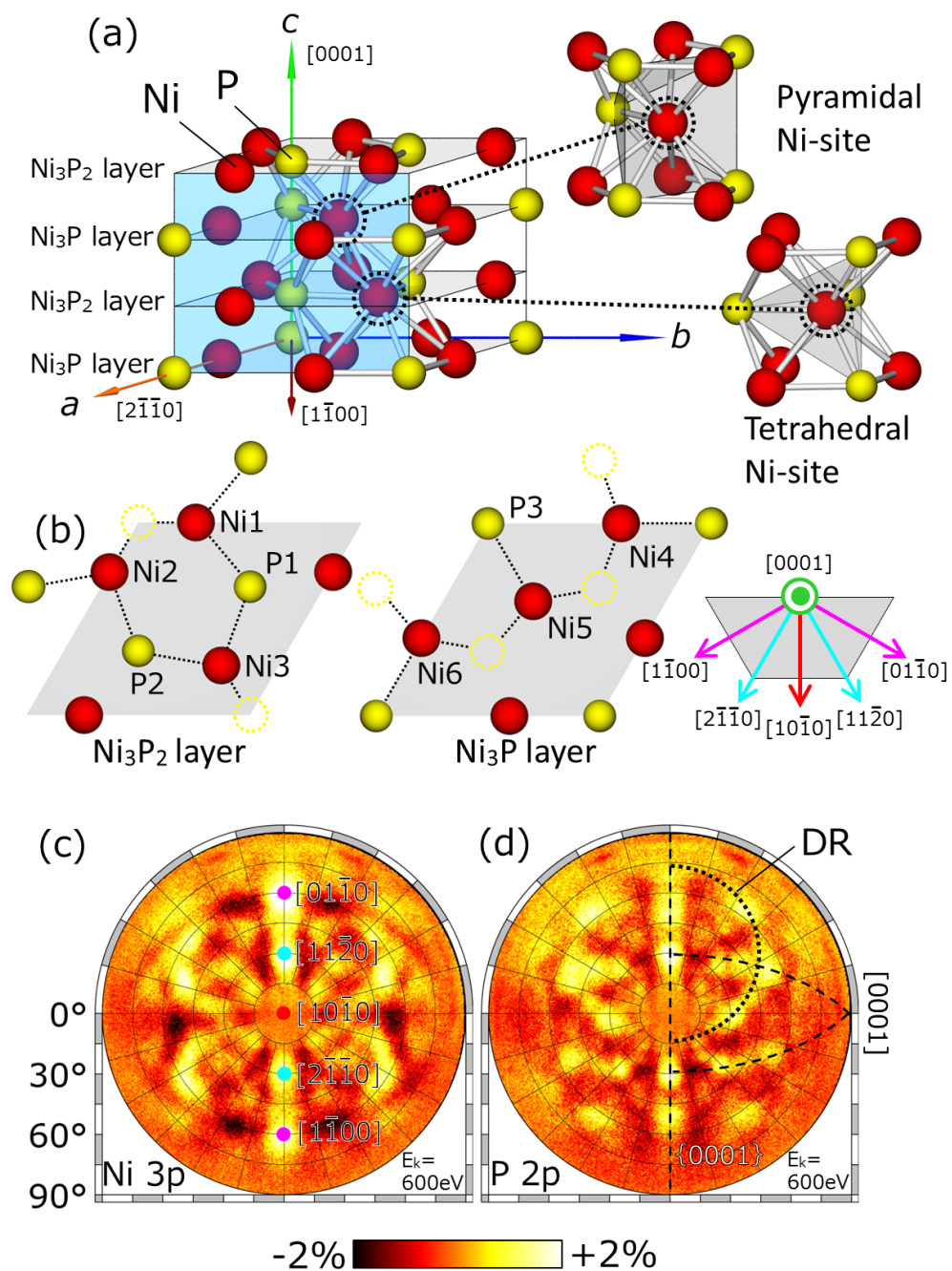


Fig. 5.1. (a) Crystalline structure of Ni_2P . Red and yellow spheres indicate Ni and P atoms, respectively. The blue colored rectangle indicates the $\{10\bar{1}0\}$ plane which was used in this study. (b) The set of atomic arrangement in Ni_3P_2 and Ni_3P layers. Yellow dotted circles indicate the out plane position of P atoms. (c) and (d) The set of 2π -steradian Ni 3p and P 2p photoelectron intensity angular distributions (PIADs) from the clean $\text{Ni}_2\text{P}(10\bar{1}0)$ surface, respectively. All PIADs were obtained with the kinetic energy of 600 eV and displayed in azimuth equidistant projection.

Then, each core-level specific PIADs from the W-Ni₂P surface was obtained. The FFP positions, diffraction patterns and their circular dichroism from Ni 3p and P 2p PIADs were basically similar before and after the W deposition (not shown). This indicates that the Ni₂P structure was not changed by the W deposition. In Fig. 5.2(a), 2 π -steradian W 4f PIAD from the W-Ni₂P surface is shown. The W 4f PIAD was similar to that of Ni 3p. The signal intensity profiles along the {0001} plane for Fig. 5.1(c), 5.1(d) and Fig. 5.2(a) are displayed in Fig. 5.2(b). The W and Ni profiles showed similar features, while that of P did not have the intensity around the [01 $\bar{1}$ 0] and [1 $\bar{1}$ 00] directions. Thus the selective substitution of W to the Ni site in the Ni₂P crystal was clarified. The destination of the substituted Ni atom is still an open question.

The chemical composition and the film thickness of W-Ni₂P were analyzed by constant-final-state-mode of a two-dimensional photoelectron spectroscopy. Photoelectron kinetic energy was fixed at 600 eV, while photon energy was scanned from 600 eV to 840 eV, so that we could detect W 4f, Ni 3p and P 2p core levels at the same kinetic energy. Thus the probing depth for each emission angle was kept constant for different binding energies. Figure 5.2(c) shows the signal intensity ratio of W 4f over Ni 3p for each emission angle from the polar angle of 2.5° to 77.5° every 5 \pm 2.5° considering the photoionization cross sections and the matrix element for f- and p-orbits [35]. The composition of W 4f versus Ni 3p in the measured XPS was shown with black colored plots. The value became higher with the emission polar angle increased. This indicates that the W structure is dominant near the surface. Here, W and Ni intensities were determined by the following equations by considering photoelectron

mean free path length λ ,

$$I_W = x \int_0^d e^{-\frac{z}{\lambda \cos \theta}} dz \quad (8)$$

$$I_{Ni} = (1 - x) \int_0^d e^{-\frac{z}{\lambda \cos \theta}} dz + \int_d^\infty e^{-\frac{z}{\lambda \cos \theta}} dz \quad (9)$$

where x and d indicate the substitution ratio of W to the Ni site and the thickness of W-Ni₂P, respectively. λ was estimated to be 1.53 nm by Tanuma *et al.*'s equation [36]. The intensity ratio of W versus Ni was expressed by the following equation,

$$I_{W/Ni} = \frac{x(e^{-\frac{d}{\lambda \cos \theta}} - 1)}{(1 - x)(e^{-\frac{d}{\lambda \cos \theta}} - 1) - e^{-\frac{d}{\lambda \cos \theta}}} \quad (10)$$

The expected model with a parameter of $x = 0.22$ and $d=1.4$ nm was shown with red colored plots in Fig. 5.2(c) About one fifth of Ni atom were replaced by W atoms at the surface layer and some diffused into subsurface region.

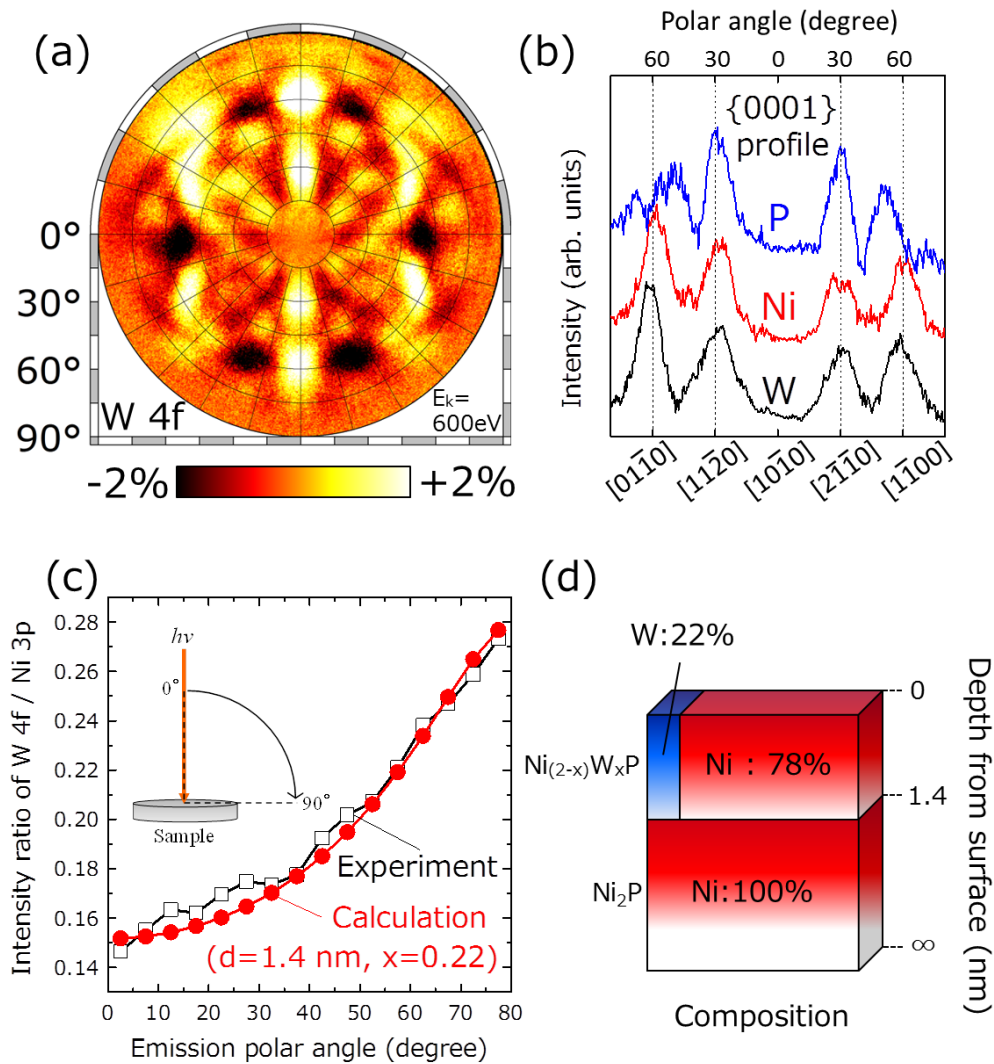


Fig. 5.2. (a) 2π -steradian W 4f PIAD from the W-modified Ni_2P ($10\bar{1}0$) surface (W- Ni_2P). (b) Signal intensity profiles along the $\{0001\}$ Kikuchi-band for the element specific PIADs in Fig. 5.1(c), 5.1(d) and 5.2(a). (c) The comparison of the signal intensity ratio of W versus Ni between the experimental and the calculation value for each emission angle. Black and red colored plots indicate the experimental and calculated values, respectively. (d) The expected model of W- Ni_2P on the Ni_2P substrate. Vertical and horizontal directions indicate the depth direction and the substituted ratio of W to the Ni site, respectively.

The chemical reactivity difference between W-Ni₂P and clean Ni₂P surfaces was studied by NO adsorption. This NO adsorption method is widely used for the study of active surface site for HDS catalyst [37]. Figure 5.3(a) shows the wide area XPS spectra taken before and after NO dosing for both surfaces. NO did not adsorb on the clean surface, while the significant increase of N 1s and O 1s core-level peaks intensities were confirmed on the W-Ni₂P surface. The signal intensity of O 1s was twice as large than that of N 1s, implying that NO gas was dissociated on the surface and a part of N was desorbed. Figure 5.3(b) shows the detail XPS spectra for W 4f, Ni 3p and P 2p core-level peaks were simple Gaussian dispersion, while W 4f had a shoulder structure shifted by 2 eV to higher binding energy due to spin orbit interaction of 4f_{7/2} and 5/2. After NO dosing, new shoulder structures appeared in the W 4f and P 2p spectra shifted by 2 and 3.5 eV to higher binding energy, respectively. This indicates that the dissociated O oxidized W and P. W-Ni₂P surface showed a possibility of high catalytic properties which was not observed on the Ni₂P surface.

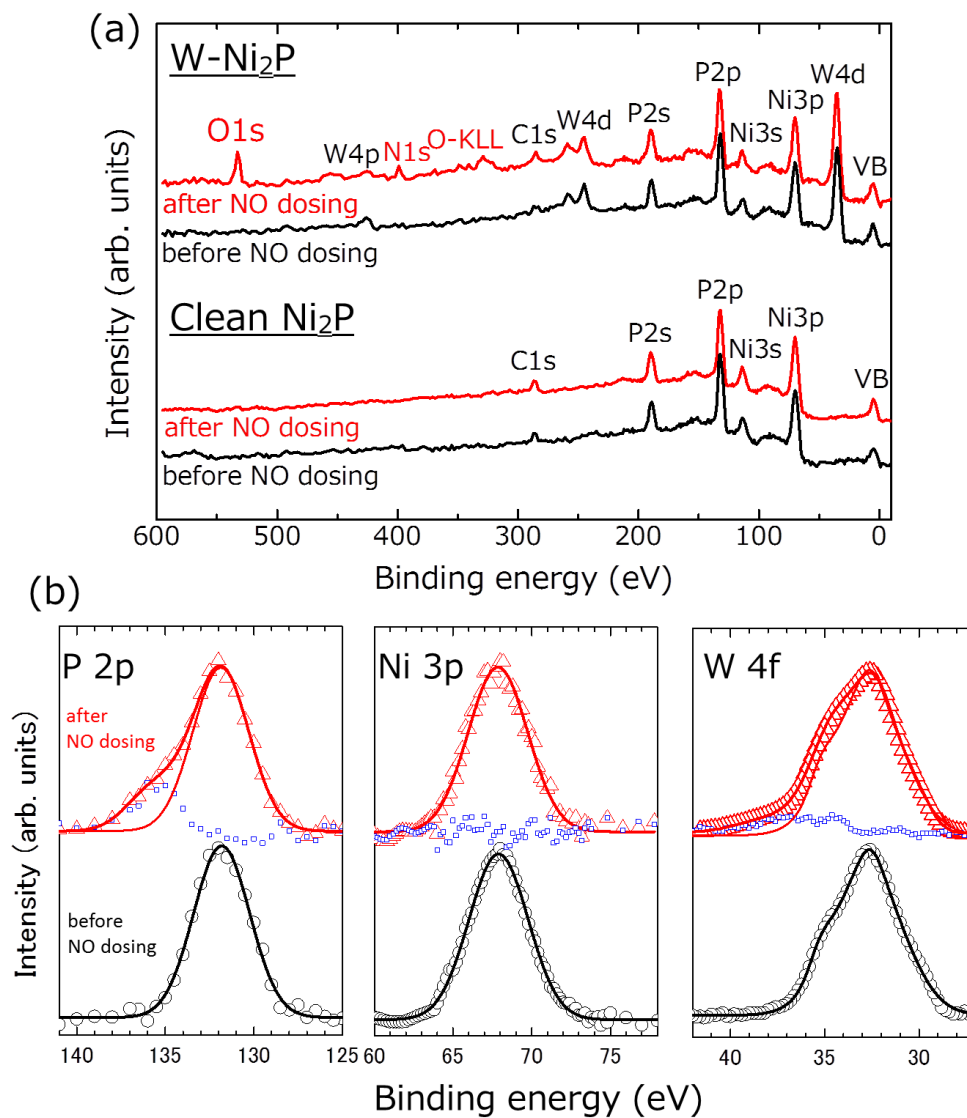


Fig. 5.3. (a) Wide area XPS spectra taken before and after 1000 Langmuir NO dosing at room temperature for the clean Ni₂P and the W-Ni₂P surfaces. (b) Detail XPS spectra for W 4f, Ni 3p and P 2p taken before and after NO dosing. The blue plots indicate the difference spectra for before and after NO dosing.

5.4 Conclusion

In conclusion, we have characterized the clean and W-modified $\text{Ni}_2\text{P}(10\bar{1}0)$ surfaces by PED. Element specific PIADs clarified the replacement of W onto the Ni site, while maintaining the Ni_2P structure. Newly observed W- Ni_2P (W/Ni=0.2) on the Ni_2P substrate showed a remarkable activity for NO adsorption which was not observed on the clean Ni_2P surface. Therefore, this surface is expected to have a new catalytic properties. PED combined with XPS was an useful analysis tool for clarifying the complex alloyed structure and the catalytic properties.

References

- [1] R. Leliveld and S. Eijsbouts. How a 70-year-old catalytic refinery process is still ever dependent on innovation. *Catal. Today* **130** (2008) 183–189.
- [2] S. T. Oyama. Novel catalysts for advanced hydroprocessing: transition metal phosphides. *J. Catal.* **216** (2003) 343–352.
- [3] J. A. Rodriguez, J. Y. Kim, J. C. Hanson, S. J. Sawhill and M. E. Bussell. Physical and chemical properties of MoP, Ni₂P, and MoNiP hydrodesulfurization catalysts: Time-resolved X-ray diffraction, density functional, and hydrodesulfurization activity studies. *J. Phys. Chem. B* **107** (2003) 6276–6285.
- [4] F. Sun, W. Wu, Z. Wu, J. Guo, Z. Wei, Y. Yang, Z. Jiang, F. Tian and C. Li. Dibenzothiophene hydrodesulfurization activity and surface sites of silica-supported MoP, Ni₂P, and NiMoP catalysts. *J. Catal.* **228** (2004) 298–310.
- [5] I. I. Abu and K. J. Smith. The effect of cobalt addition to bulk MoP and Ni₂P catalysts for the hydrodesulfurization of 4, 6-dimethyldibenzothiophene. *J. Catal.* **241** (2006) 356–366.
- [6] V. Zuzaniuk and R. Prins. Synthesis and characterization of silica-supported transition-metal phosphides as HDN catalysts. *J. Catal.* **219** (2003) 85–96.
- [7] A. F. Gaudette, A. W. Burns, J. R. Hayes, M. C. Smith, R. H. Bowker, T. Seda and M. E. Bussell. Mossbauer spectroscopy investigation and hydrodesulfurization properties of iron–nickel phosphide catalysts. *J. Catal.* **272** (2010) 18–27.

- [8] A. Cho, J. Shin, A. Takagaki, R. Kikuchi and S. T. Oyama. Ligand and Ensemble Effects in Bimetallic NiFe Phosphide Catalysts for the Hydrodeoxygenation of 2-Methyltetrahydrofuran. *Top. Catal.* **55** (2012) 969–980.
- [9] S. T. Oyama, H. Zhao, H. J. Freund, K. Asakura, R. Włodarczyk and M. Sierka. Unprecedented selectivity to the direct desulfurization (DDS) pathway in a highly active FeNi bimetallic phosphide catalyst. *J. Catal.* **285** (2012) 1–5.
- [10] J. Kopyscinski, J. Choi, L. Ding, S. Zhang, B. Ibeh and J. M. Hill. Ni promotion of WP/SiO₂ Catalysts for Pyridine Hydrodenitrogenation. *Catal. Lett.* **142** (2012) 845–853.
- [11] G. Moula, S. Suzuki, W. J. Chun, S. Otani, S. T. Oyama and K. Asakura. The first atomic-scale observation of a Ni₂P(0001) single crystal surface. *Chem. Lett.* **35** (2006) 90–91.
- [12] K. Kinoshita, G. H. Simon, T. König, M. Heyde, H. J. Freund, Y. Nakagawa, S. Suzuki, W. J. Chun, S. T. Oyama, S. Otani and K. Asakura. A Scanning Tunneling Microscopy Observation of ($\sqrt{3} \times \sqrt{3}R30^\circ$ Reconstructed Ni₂P(0001)). *Jpn. J. Appl. Phys.* **47** (2008) 6088.
- [13] S. Suzuki, G. M. Moula, T. Miyamoto, Y. Nakagawa, K. Kinoshita, K. Asakura, S. T. Oyama and S. Otani. Scanning tunneling microscopy and photoemission electron microscopy studies on single crystal Ni₂P surfaces. *J. Nanosci. Nanotechnol.* **9** (2009) 195–201.
- [14] D. Guo, Y. Nakagawa, H. Ariga, S. Suzuki, K. Kinoshita, T. Miyamoto, S. Takakusagi,

- K. Asakura, S. Otani and S. T. Oyama. STM studies on the reconstruction of the $\text{Ni}_2\text{P}(10\bar{1}0)$ surface. *Surf. Sci.* **604** (2010) 1347–1352.
- [15] D. Kanama, S. T. Oyama, S. Otani and D. F. Cox. Photoemission and LEED characterization of $\text{Ni}_2\text{P}(0001)$. *Surf. Sci.* **552** (2004) 8–16.
- [16] A. B. Hernandez, H. Ariga, S. Takakusagi, K. Kinoshita, S. Suzuki, S. Otani, S. T. Oyama and K. Asakura. Dynamical LEED analysis of $\text{Ni}_2\text{P}(0001)\text{-}1\times 1$: Evidence for P-covered surface structure. *Chem. Phys. Lett.* **513** (2011) 48–52.
- [17] C. S. Fadley, Y. Chen, R. E. Couch, H. Daimon, R. Denecke, J. D. Denlinger, H. Gallaway, Z. Hussain, A. P. Kaduwela, Y. J. Kim, et al. Diffraction and holography with photoelectrons and fluorescent X-rays. *Prog. Surf. Sci.* **54** (1997) 341–386.
- [18] H. Daimon. Stereoscopic Microscopy of Atomic Arrangement by Circularly Polarized-Light Photoelectron Diffraction. *Phys. Rev. Lett.* **86** (2001) 2034–2037.
- [19] F. Matsui, N. Nishikayama, N. Maejima, H. Matsui, K. Goto, M. Hashimoto, T. Hatayama, T. Matsushita, Y. Kato, S. Tanaka and H. Daimon. Site-Specific Stereograph of $\text{SiC}(0001)$ Surface by Inverse Matrix Method. *J. Phys. Soc. Jpn.* **80** (2011) 013601.
- [20] F. Matsui, T. Matsushita and H. Daimon. Photoelectron Diffraction and Holographic Reconstruction of Graphite. *J. Phys. Soc. Jpn.* **81** (2012) 114604.
- [21] W. Auwärter, K. T. J., T. Gerber and O. J. XPD and STM investigation of hexagonal boron nitride on $\text{Ni}(111)$. *Surf. Sci.* **429** (1999) 229–236.

- [22] Y. Kato, F. Matsui, T. Shimizu, H. Daimon, T. Matsushita, F. Z. Guo and T. Tsuno. Dopant-site effect in superconducting diamond (111) studied by atomic stereophotography. *Appl. Phys. Lett.* **91** (2007) 251914–251914.
- [23] O. Shigeki and O. Naoki. Preparation of Ni₂P and Fe₂P single crystals by the floating-zone method. *J. Ceram. Soc. Japan* **121** (2013) 331–332.
- [24] H. Daimon. New display-type analyzer for the energy and the angular distribution of charged particles. *Rev. Sci. Instrum.* **59** (1988) 545–549.
- [25] H. Daimon and S. Ino. Improvement of the spherical mirror analyzer. *Rev. Sci. Instrum.* **61** (1990) 57–60.
- [26] M. Kotsugi, Y. Miyatake, K. Enomoto, K. Fukumoto, A. Kobayashi, T. Nakatani, Y. Saitoh, T. Matsushita, S. Imada, T. Furuhashi, et al. Construction of two-dimensional photoelectron spectrometer at SPring-8. *Nucl. Instrum. Methods Phys. Res., Sect. A* **467** (2001) 1493–1496.
- [27] F. Matsui, H. Daimon, F. Guo and T. Matsushita. Visualization of graphite atomic arrangement by stereo atomscope. *Appl. Phys. Lett.* **85** (2004) 3737–3739.
- [28] F. Matsui, T. Matsushita, Y. Kato, F. Guo and H. Daimon. Site-specific orbital angular momentum analysis of graphite valence electron using photoelectron forward focusing peaks. *J. Phys. Soc. Jpn.* **76** (2007).
- [29] F. Matsui, T. Matsushita, Y. Kato, M. Hashimoto, K. Inaji, F. Z. Guo and H. Daimon. Atomic-layer resolved magnetic and electronic structure analysis of Ni thin film on a Cu (001) surface by diffraction spectroscopy. *Phys. Rev. Lett.* **100** (2008) 207201.

- [30] F. Matsui, T. Matsushita and H. Daimon. Atomic-layer-resolved analysis of surface magnetism by diffraction spectroscopy. *J. Electron Spectrosc. Relat. Phenom.* **181** (2010) 150–153.
- [31] T. Matsushita, F. Guo, F. Matsui, Y. Kato and H. Daimon. Three-dimensional atomic-arrangement reconstruction from an Auger-electron hologram. *Phys. Rev. B* **75** (2007) 085419.
- [32] K. Inaji, F. Matsui, Y. Kato, C. Sakai, T. Narikawa, T. Matsushita, F. Z. Guo and H. Daimon. Circular dichroism of forward focusing peaks and diffraction rings in 2π steradian Si 2p photoelectron pattern. *Appl. Surf. Sci.* **254** (2008) 7549–7552.
- [33] T. Muro, T. Nakamura, T. Matsushita, H. Kimura, T. Nakatani, T. Hirono, T. Kudo, K. Kobayashi, Y. Saitoh, M. Takeuchi, T. Hara, K. Shirasawa and H. Kitamura. Circular dichroism measurement of soft X-ray absorption using helicity modulation of helical undulator radiation. *J. Electron Spectrosc. Relat. Phenom.* **144** (2005) 1101–1103.
- [34] S. Rundqvist. X-ray investigations of Mn_3P , Mn_2P and Ni_2P . *Acta Chem. Scand.* **16** (1962) 8–16.
- [35] The data are taken from: J.J. Yeh, Atomic Calculation of Photoionization Cross-Sections and Asymmetry Parameters, Gordon and Breach Science Publishers, Langhorne, PE (USA), 1993 and from J.J. Yeh and I.Lindau, Atomic Data and Nuclear Data Tables, 32, 1-155 (1985).
- [36] S. Tanuma, C. Powell and D. Penn. Calculations of electron inelastic mean free paths.

IX. data for 41 elemental solids over the 50 ev to 30 kev range. *Surf. InterfaceAnal.* **43**
(2011) 689–713.

[37] N. Y. Topsøe and H. Topsøe. Characterization of the structures and active sites in sulfided Co·MoAl₂O₃ and Ni·MoAl₂O₃ catalysts by NO chemisorption. *J. Catal.* **84**
(1983) 386–401.

Chapter 6. Atomic structure analysis of catalytic polycrystalline Ni₂P surface by microscopic photoelectron diffraction

The polycrystalline Ni₂P surface made by heat decomposition was characterized by microscopic photoelectron diffraction. The orientation and structure at each crystal grain was analyzed by scanning along the sample vertical and horizontal directions. 2π -steradian Ni 3p and P 2p PIADs showed three- and four-fold symmetric structures which was not seen on the hexagonal Ni₂P structure. The photoelectron intensity ratio of Ni 3p versus P 2p showed a similar surface composition less than 5% for both single and polycrystalline Ni₂P surfaces. These knowledge strongly suggest the phase transition to unknown CaF₂-type structure. Dimethyldisulfide, (CH₃)₂S₂, was dosed on the surface to evaluate the chemical reactivity at each crystal grain. The signal intensity of S tended to higher at Ni-rich surface position.

6.1 Introduction

Ni_2P , a transition metal phosphide, is expected to be a next generation catalyst for hydrodesulfurization (HDS) reactions [1]. Ni_2P belongs to the space group $\text{P}\bar{6}_2\text{m}$ of hexagonal symmetry with $a=b=0.586$ nm and $c=0.338$ nm, in which the Ni atoms form two types of atomic sites, tetrahedral (T) and pyramidal (Py) [2]. Because the local structure at each Ni site differs, especial catalytic properties are expected.

Oyama *et al.* characterized several size of Ni_2P nano particles supported on different substrates by x-ray absorption fine structure (XAFS), which enables an in situ observation [3]. Their XAFS analysis observed the increasing of coordination numbers while the crystallite size goes down, suggesting that the surface is terminated with a Py site. The smaller particle size, which has a higher surface area, tended to show higher HDS activity. They found the relation between the surface termination with Py site and the high activity, indicating that the breaking of the bulk arrangement may be related with the catalytic properties. Although XAFS is a powerful characterization for studying the local atomic structure, the Ni_2P obtains a complex structure with more than two Ni-P distances due to the number of Ni sites. Their recent study immediately faced on the difficulty in distinguishing the local Ni site for the alloyed FeNi bimetallic phosphide, which achieved the unprecedented selectivity to the direct desulfurization pathway [4]. The precise relation between the surface structure and catalytic activities is difficult to understand only by XAFS.

Surface science studies using a single-crystalline sample as a model catalyst have been elucidating the surface structure and shedding light on the properties. Previous scanning tunneling microscope (STM) [5–8] and low energy electron diffraction (LEED) [5, 6, 8–10]

analyses observed the long range periodicity of the surface terminated atom. The Ni₂P(0001) surface had several reconstructed structures such as ($\sqrt{3}\times\sqrt{3}$)-R30°, (2/3×2/3) and (2×2) in addition to the primitive (1×1) structure [5, 6]. Another (10 $\bar{1}$ 0) surface, which has a stoichiometric composition of a bulky Ni/P=2 ratio, was found to terminate with c(2×4) and (1×1) structures [8]. They concluded that all periodicity comes from the super structure of inactive P atoms. However, not only two-dimensional atomic arrangements but also three-dimensional atomic configurations have not yet been observed. Furthermore, the catalytic behavior for the adsorption of sulfide such as thiophene, (CH₃)-Ph, is different between the real catalyst and the single-crystalline surface. Therefore, the study using a more approximated surface, *i. e.*, poly-crystalline surface must be studied.

A photoelectron from a localized core level is an excellent site and element selective probe for surface structure analysis [11]. Forward focusing peaks (FFPs) appearing in the photoelectron intensity angular distribution (PIAD) indicate the directions of surrounding atoms seen from the photoelectron emitter atom [12]. The atomic distance between the emitter and scatterer atoms can be deduced from the circular-dichroism shift of FFP position [12–14] as well as from the opening angles of diffraction rings (DRs) appearing around the FFP [14, 15]. We have observed Ni 3p and P 2p PIADs from a single-crystalline Ni₂P (10 $\bar{1}$ 0) surface in Chapter 2-4. The PIADs reflected well the Ni₂P structure, implying that photoelectron diffraction (PED) is an useful analysis tool for studying the surface structure and orientations with element selectivity. Here, the comparison of analytical characters, advantages and disadvantages for the number of poly crystalline characterization is shown in Fig 6.1. Every technique reported by now is complementary each other. In contrast, PED is an ideal and unique technique for studying the relation between crystalline orientation, structure and

chemical reactivity. The spatial distribution is depended on the size of soft x-ray (the radii of soft x-ray at BL25SU in SPring-8 is $\phi=20 \mu\text{m}$.)

In this study, we have characterized a poly-crystallized Ni_2P surface by a similar approach. The series of PIADs scanned along the sample in-plane observed the orientation distribution at each crystal grain. X-ray photoelectron spectroscopy (XPS) and the simulated PIADs clarified the unknown Ni_2P structure in a poly-crystalline phase. Furthermore, dimethyldisulfide, $(\text{CH}_3)_2\text{S}_2$, was dosed on the surface and the activity at each crystal grain was compared. The adsorption of S was confirmed which had not been observed on the single-crystalline surface.

	XRD	SEM			TEM		PEEM	LEEM	PED
	X-ray micro Laue method	Micro facet pit	EBSD	ECP	SAD	Kikuchi line method			
Spatial resolution	1 mm	10 μm	10 nm	5 μm	1 μm	several nm	10 nm	10 nm	20 μm
Crystalline structure	Δ	Δ	\circ	\circ	\circ	\circ	\times	\circ	\circ
Element selectivity	\times	\times	\times	\times	\times	\times	\circ	\times	\circ
Chemical reactivity	\times	\times	\times	\times	\times	\times	\times	\times	\circ

Fig. 6.1. The comparison of character, advantage/disadvantage for each poly crystalline characterization.

6.2 Experimental details

A single-crystalline $\text{Ni}_2\text{P}(10\bar{1}0)$ surface with a size of $5\times 10\times 1$ mm was used as the substrate [16]. The sample surface was heated by closing the W filament at 2000°C for 10 min and was decomposed onto poly-crystalline surface after transferring into an ultra-high vacuum (UHV) chamber with a base pressure of less than 3×10^{-8} Pa. A poly-crystallized procedure was taken to the air once and mechanically polished to a mirror finishing to eliminate any impurities and make the sample surface flat. The sample surface was cleaned by Ar^+ sputtering at 2.5 keV (sample current: $1\ \mu\text{A}$, time: 30 min, Ar pressure: 1×10^{-3} Pa) and annealed at 350°C by direct current injection repeatedly [8]. The annealing temperature was monitored by a K-type thermo-coupling. The surface structure was determined by reflection high-energy electron diffraction (RHEED). The superimposed patterns from different orientations were obtained and the pattern changed by scanning the sample surface, indicating that a number of orientations were realized on the surface. The chemical composition on the surface was observed by XPS. Carbon and oxygen impurity peaks were completely eliminated from the surface. Note that the intensity ratio of Ni 3p versus P 2p was not changed before or after poly-crystallization (not shown), indicating that the composition of poly-crystallized Ni_2P kept constant on the single-crystalline surface.

Dimethyldisulfide, $(\text{CH}_3)_2\text{S}_2$, was dosed 1000 Langmuir (3×10^{-3} Pa, 100 sec) at 350°C to observe the catalytic reactivity at each crystal grain. $(\text{CH}_3)_2\text{S}_2$ will be dissociated onto the substrate surface and adsorbed as methylsulfide, $\text{CH}_3\text{-S}$. The amount of surface adsorbate was determined by XPS.

PIAD from the sample at a specific kinetic energy was most efficiently measured using a

two-dimensional display-type spherical mirror analyzer (DIANA)[17–19], which is installed at circularly-polarized soft x-ray beamline BL25SU at SPring-8, in Japan. A two-dimensional angular distribution snapshot of a specific kinetic energy electron could be measured [12, 20–23]. The acceptance angle of the analyzer was $\pm 60^\circ$. Light was incident from the direction of 45° inclined from the analyzer center. Two-dimensional scanning of PIAD along the sample in-plane was measured by a 45° inclined light from the sample surface. The detecting range of PIAD was a polar angle of less than 60° . A 2π steradian PIAD was obtained by scanning the sample azimuth for 360° [24, 25]. The emission angle θ dependence from 0 to 90° relative to the surface normal was measured simultaneously. The helicity (σ_{\pm}) of monochromatized circularly-polarized soft X-ray was altered by switching the path of storage ring electrons in twin helical undulators at 0.1 Hz [26]. The photon energy resolution was better than 100 meV. The total acquisition time for a pair of 2π -steradian PIADs excited by σ_+ and σ_- helicity lights was 2.5 hr. All data was measured at room temperature. The energy window width of DIANA was set to 30 eV for PIAD measurements, to achieve the best angular resolution. All PIADs were obtained with a photoelectron kinetic energy of 600 eV, and displayed in azimuth equidistant projection.

6.3 Results and discussion

Figure 6.2 shows the series of Ni 3p PIADs by scanning the sample in-plane. The sample surface along the vertical ± 1.0 mm and horizontal ± 1.5 mm region every $200 \mu\text{m}$ step was measured. The clear pattern contrasts were seen for all PIADs, suggesting the polycrystallized procedure kept the crystalline quality. Four-, three-fold symmetric and the intermediate orientations were found at each crystal grain. The orientation degree was shown with color scale from blue to red. The black color indicates unexplained areas due to the complex pattern coming from the grain boundary and the weak contrast relating with the crystalline quality. The orientation was completely random but the grain size was above hundreds μm . This indicates that the grain size was larger than the soft x-ray diameter $\phi 300 \mu\text{m}$ at BL25SU in SPring-8 and made possible the analysis of the poly-crystalline sample by photoelectron diffraction.

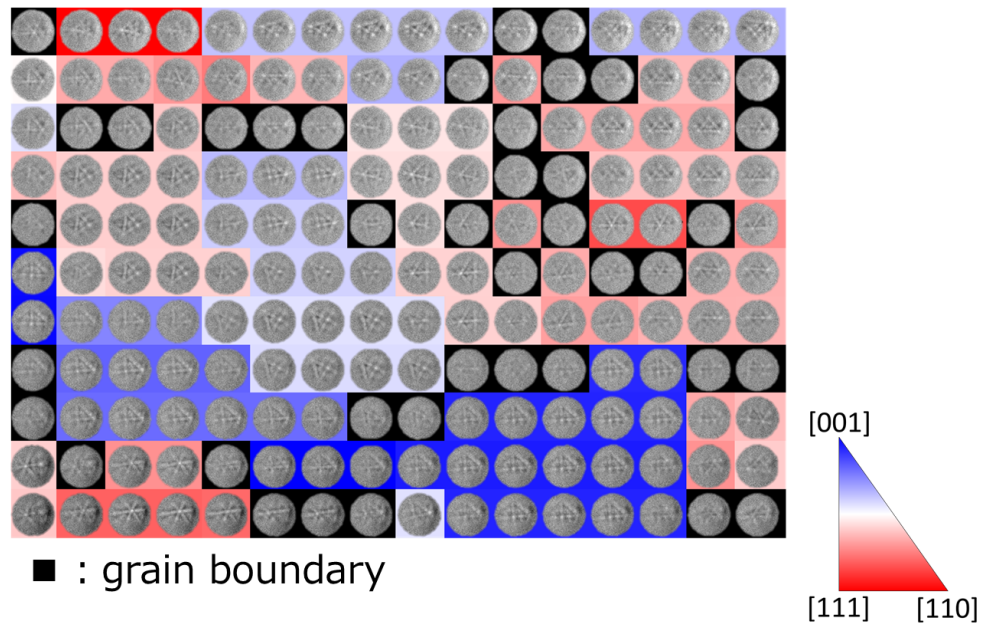


Fig. 6.2. The series of Ni 3p photoelectron intensity angular distributions (PIADs) by scanning the sample surface in-plane. The sample surface along the vertical ± 1.0 mm and horizontal ± 1.5 mm region every $200 \mu\text{m}$ step was measured. The orientation degree was shown with a color scale from blue to red corresponding to 4- and 3-fold symmetry, respectively. The black color denotes the unexplained areas due to the grain boundary and crystalline quality.

The PIAD helped to determine the crystalline structure and orientation. Surprisingly, the initial $\text{Ni}_2\text{P}(10\bar{1}0)$ surface, which only has a mirror symmetry, was found to disappear from all the sample surfaces. A three-fold symmetric structure was expected on the hexagonal (0001) surface but 4-fold symmetry was not allowed on Ni_2P crystal. To satisfy both four- and three-fold symmetric PIADs, a cubic lattice was reasonable. Also, XPS analysis suggested that the bulky composition of $\text{Ni}/\text{P}=2$ was kept constant within 5% error before and after poly-crystallization, indicating that AB_2 -type structure was expected. To satisfy both XPS and PIAD results, a CaF_2 structure, Ni and P atoms coordinated in F and Ca sites, was favorable. In a CaF_2 structure, the Ni atom is surrounded only by tetrahedral P atom structure.

In Fig. 6.3, measured 2π -steradian Ni 3p and P 2p PIADs at a typical four- and three-fold symmetric position, the simulated Ni 3p and P 2p PIADs and the corresponding structure models for the expected CaF_2 structure (111) and (001) surface, were shown. Two PIAD images using σ_+ and σ_- helicity lights were superimposed. When excited with σ_+ helicity light, diffraction patterns rotated clockwise (red), while they rotated counterclockwise (blue) when excited with σ_- helicity light. For the simulation, the multiple scattering pattern code, *TMSP*, which was developed by one of the authors (T. Matsushita) was used [27]. The radius 8\AA cluster model consisting of 84 Ni atoms and 55 P atoms was used in the simulation to imitate the experimental data. Angular resolution was determined as 4° in this measurement. The FFP positions and diffraction patterns were basically similar, indicating a the formation of a CaF_2 -type structure.

To analyze the detail structure, the circular dichroism of the photoelectron was analyzed. Daimon found the relation between the inter atomic distance from the emitter to the scatterer

atoms: R and the rotational shift of FFP: $\Delta\phi$ as the following formula:

$$\Delta\phi = \frac{m^*}{kR\sin^2\theta} \quad (11)$$

where m^* , k and θ are the effective magnetic quantum number, the wave number of photoelectron and the angle between the incident photon direction and the outgoing direction of the emitted photoelectrons, respectively. In general, m^* considers the contribution to the transition from different initial states weighted by the transition probability at a particular angle. In Fig. 6.3(a), the intense peak at $\langle 011 \rangle$ at the polar angle of 54.7° was seen and showed the circular dichroism. This signal originated from the FFP created by the second nearest Ni atom. $\Delta\phi$ of $2.41 \pm 0.05^\circ$ corresponding to the diagonal distance in a half unit length of 0.42 ± 0.01 nm was obtained. Therefore, the measured unitcell length was 0.59 ± 0.01 nm. In Fig. 6.3(d), the $\langle 001 \rangle$ FFP at the polar angle of 35.3° showed $\Delta\phi$ of $2.14 \pm 0.05^\circ$ corresponding to the unit length of 0.62 ± 0.01 nm. Each value was similar to the $\text{Ni}_2\text{P}(0001)$ unit length of 0.586 nm [2].

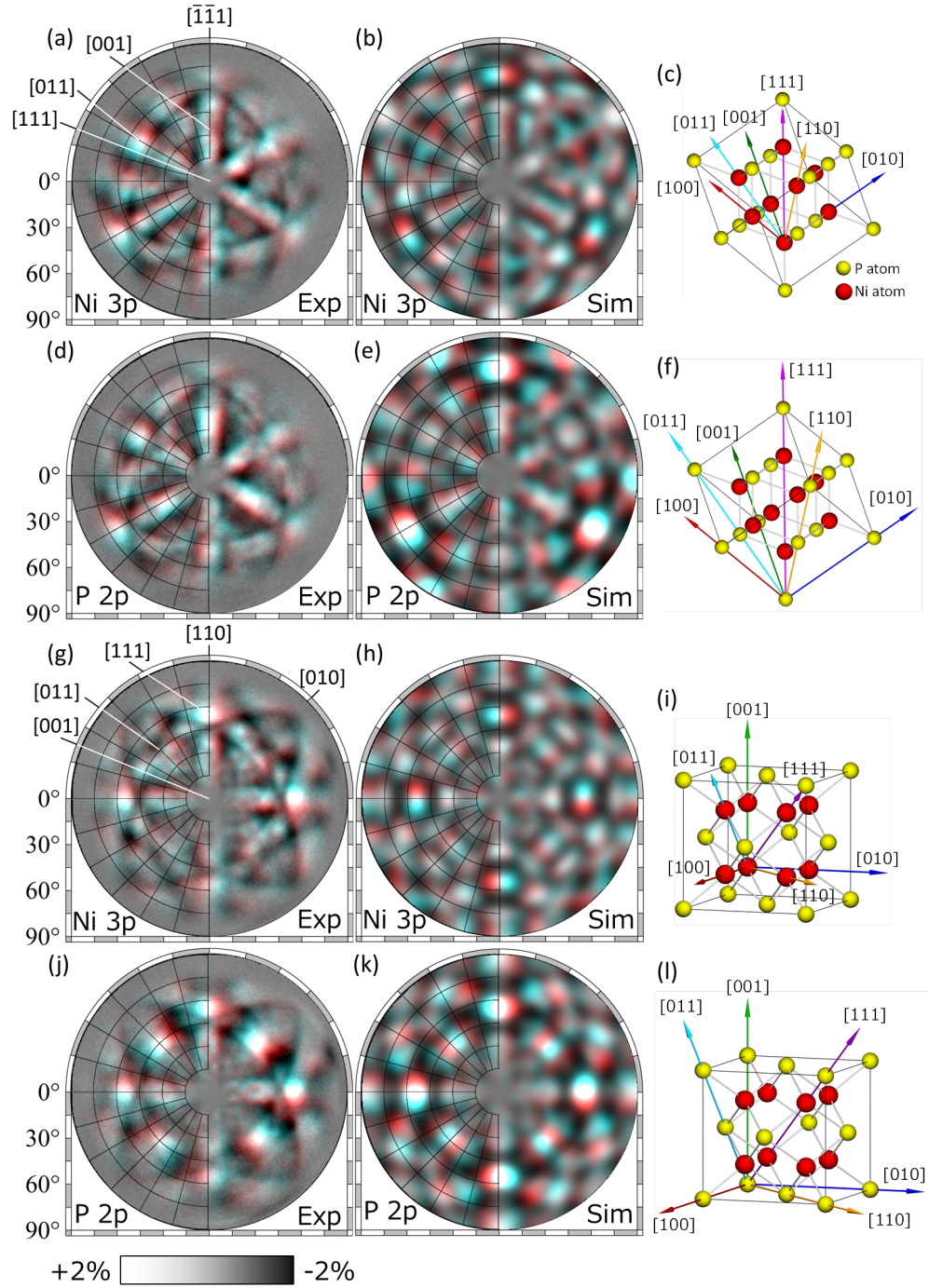


Fig. 6.3. (a), (b) and (c) Measured 2π -steradian Ni 3p PIAD at 3-fold symmetric grain, the simulated Ni 3p PIAD and the corresponding structure model for the expected CaF_2 structure (111) surface. (d), (e) and (f) Same with (a), (b) and (c) but for P 2p. (g), (h) and (i) Measured 2π -steradian Ni 3p PIAD at 4-fold symmetric grain, the simulated Ni 3p PIAD and the corresponding structure model for the expected CaF_2 structure (001) surface. (j), (k) and (l) Same with (g), (h) and (i) but for P 2p. All PIADs were obtained with a photoelectron kinetic energy of 600 eV and displayed in azimuth equidistant projection. Red and blue colors indicate the circular-dichroism shift of forward focusing peaks at each helicity light excitation.

The surface reactivity to the adsorption of sulfur at each crystal grain was studied. Figure 6.4(a) shows the comparison of XPS spectra before and after dosing with $(\text{CH}_3)_2\text{S}_2$. The increasing of S 2p peak was confirmed. The peak shifts at each core-level were not observed due to the limitation of the energy resolution: 1 eV and the active element was not determined. As shown in Fig. 6.4(b) and 6.4(c), the signal intensities integrating all emission angles from the Ni 3p and P 2p core-level at each grain are shown as a color scale. The blue and red colors indicate the weaker and stronger intensities in the sample surface in-plane. The signal intensity distribution $\pm 5\%$ was seen and did not relate with the random orientation of the sample surface as shown in Fig. 6.2. Note that the specific reactivity at grain boundary was not observed. At the sample upper side, the signal intensity of Ni 3p tended to be stronger, while that of P 2p was weaker. This result indicating the slight breaking of the surface composition. The tendency from S 2p shown in Fig. 6.4(d) was similar to that of Ni 3p. Thus S reacted at the Ni-rich surface and made the Ni-S bond. Sulfide, such as thiophene, S-Ph, have been hard to adsorb on the single-crystalline Ni_2P surface because of inactive P atoms covering the surface. However, the poly-crystallized surface achieved the lower coordination of P atoms and avoided the steric hindrance. Therefore, the difference of surface terminated atoms and the composition between the single-crystalline and poly-crystalline surface was supposed. We clarified the removal of P atoms from the surface as the key for realizing a high performance catalysis.

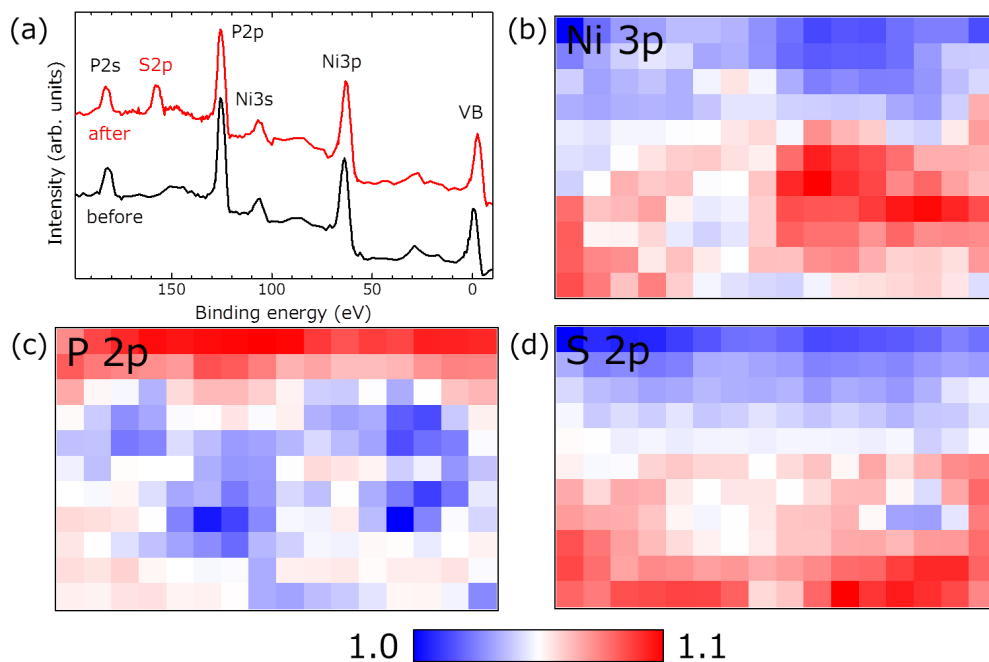


Fig. 6.4. (a) The comparison of x-ray photoelectron spectra before and after dosing with dimethyldisulfide, $(\text{CH}_3)_2\text{S}_2$. (b), (c) and (d) The color scale of $\pm 5\%$ signal intensity distribution from Ni 3p, P 2p and S 2p at each crystal grain, respectively.

6.4 Conclusion

In conclusion, the poly-crystallized Ni_2P surface made by heat decomposition was characterized by photoelectron diffraction. The microscopic analysis scanning the sample in-plane every $200\ \mu\text{m}$ obtained the orientation distribution and grain size. The single-crystalline Ni_2P structure completely disappeared after poly-crystallization and the cubic CaF_2 structure was formed on the sample surface. Furthermore, the surface reactivity with $(\text{CH}_3)_2\text{S}_2$ at each grain was measured. The amount of S adsorbate was strongly related to the surface Ni/P composition and the Ni-rich grain was active. Studies using a poly-crystalline Ni_2P surface have a possibility to clarify the difference of surface properties between the single-crystalline and the real catalyst surfaces.

References

- [1] S. T. Oyama. Novel catalysts for advanced hydroprocessing: transition metal phosphides. *J. Catal.* **216** (2003) 343–352.
- [2] S. Rundqvist. X-ray investigations of Mn_3P , Mn_2P and Ni_2P . *Acta Chem. Scand.* **16** (1962) 8–16.
- [3] S. T. Oyama and Y. K. Lee. The active site of nickel phosphide catalysts for the hydrodesulfurization of 4, 6-DMDBT. *J. Catal.* **258** (2008) 393–400.
- [4] S. T. Oyama, H. Zhao, H. J. Freund, K. Asakura, R. Włodarczyk and M. Sierka. Unprecedented selectivity to the direct desulfurization (DDS) pathway in a highly active FeNi bimetallic phosphide catalyst. *J. Catal.* **285** (2012) 1–5.
- [5] G. Moula, S. Suzuki, W. J. Chun, S. Otani, S. T. Oyama and K. Asakura. The first atomic-scale observation of a Ni_2P (0001) single crystal surface. *Chem. Lett.* **35** (2006) 90–91.
- [6] K. Kinoshita, G. H. Simon, T. König, M. Heyde, . J. Freund, Y. Nakagawa, S. Suzuki, W. J. Chun, S. T. Oyama, S. Otani and K. Asakura. A Scanning Tunneling Microscopy Observation of $(\sqrt{3} \times \sqrt{3})R30^\circ$ Reconstructed Ni_2P (0001). *Jpn. J. Appl. Phys.* **47** (2008) 6088.
- [7] S. Suzuki, G. M. Moula, T. Miyamoto, Y. Nakagawa, K. Kinoshita, K. Asakura, S. T. Oyama and S. Otani. Scanning tunneling microscopy and photoemission electron microscopy studies on single crystal Ni_2P surfaces. *J. Nanosci. Nanotechnol.* **9** (2009) 195–201.

- [8] D. Guo, Y. Nakagawa, H. Ariga, S. Suzuki, K. Kinoshita, T. Miyamoto, S. Takakusagi, K. Asakura, S. Otani and S. T. Oyama. STM studies on the reconstruction of the $\text{Ni}_2\text{P}(10\bar{1}0)$ surface. *Surf. Sci.* **604** (2010) 1347–1352.
- [9] D. Kanama, S. T. Oyama, S. Otani and D. F. Cox. Photoemission and LEED characterization of $\text{Ni}_2\text{P}(0001)$. *Surf. Sci.* **552** (2004) 8–16.
- [10] A. B. Hernandez, H. Ariga, S. Takakusagi, K. Kinoshita, S. Suzuki, S. Otani, S. T. Oyama and K. Asakura. Dynamical LEED analysis of $\text{Ni}_2\text{P}(0001)\text{-}1\times 1$: Evidence for P-covered surface structure. *Chem. Phys. Lett.* **513** (2011) 48–52.
- [11] C. S. Fadley, Y. Chen, R. E. Couch, H. Daimon, R. Denecke, J. D. Denlinger, H. Galloway, Z. Hussain, A. P. Kaduwela, Y. J. Kim, et al. Diffraction and holography with photoelectrons and fluorescent X-rays. *Prog. Surf. Sci.* **54** (1997) 341–386.
- [12] H. Daimon. Stereoscopic Microscopy of Atomic Arrangement by Circularly Polarized-Light Photoelectron Diffraction. *Phys. Rev. Lett.* **86** (2001) 2034–2037.
- [13] F. Matsui, N. Nishikayama, N. Maejima, H. Matsui, K. Goto, M. Hashimoto, T. Hatayama, T. Matsushita, Y. Kato, S. Tanaka and H. Daimon. Site-Specific Stereograph of $\text{SiC}(0001)$ Surface by Inverse Matrix Method. *J. Phys. Soc. Jpn.* **80** (2011) 013601.
- [14] F. Matsui, T. Matsushita and H. Daimon. Photoelectron Diffraction and Holographic Reconstruction of Graphite. *J. Phys. Soc. Jpn.* **81** (2012) 114604.
- [15] W. Auwärter, K. T. J., T. Gerber and O. J. XPD and STM investigation of hexagonal boron nitride on $\text{Ni}(111)$. *Surf. Sci.* **429** (1999) 229–236.

- [16] O. Shigeki and O. Naoki. Preparation of Ni_2P and Fe_2P single crystals by the floating-zone method. *J. Ceram. Soc. Japan* **121** (2013) 331–332.
- [17] H. Daimon. New display-type analyzer for the energy and the angular distribution of charged particles. *Rev. Sci. Instrum.* **59** (1988) 545–549.
- [18] H. Daimon and S. Ino. Improvement of the spherical mirror analyzer. *Rev. Sci. Instrum.* **61** (1990) 57–60.
- [19] M. Kotsugi, Y. Miyatake, K. Enomoto, K. Fukumoto, A. Kobayashi, T. Nakatani, Y. Saitoh, T. Matsushita, S. Imada, T. Furuhashi, et al. Construction of two-dimensional photoelectron spectrometer at SPring-8. *Nucl. Instrum. Methods Phys. Res., Sect. A* **467** (2001) 1493–1496.
- [20] Y. Kato, F. Matsui, T. Shimizu, H. Daimon, T. Matsushita, F. Z. Guo and T. Tsuno. Dopant-site effect in superconducting diamond (111) studied by atomic stereophotography. *Appl. Phys. Lett.* **91** (2007) 251914–251914.
- [21] F. Matsui, T. Matsushita, Y. Kato, F. Z. Guo and H. Daimon. Site-specific orbital angular momentum analysis of graphite valence electron using photoelectron forward focusing peaks. *J. Phys. Soc. Jpn.* **76** (2007).
- [22] F. Matsui, T. Matsushita, Y. Kato, M. Hashimoto, K. Inaji, F. Z. Guo and H. Daimon. Atomic-layer resolved magnetic and electronic structure analysis of Ni thin film on a C (001) surface by diffraction spectroscopy. *Phys. Rev. Lett.* **100** (2008) 207201.
- [23] F. Matsui, T. Matsushita and H. Daimon. Atomic-layer-resolved analysis of surface

- magnetism by diffraction spectroscopy. *J. Electron Spectrosc. Relat. Phenom.* **181** (2010) 150–153.
- [24] T. Matsushita, F. Z. Guo, F. Matsui, Y. Kato and H. Daimon. Three-dimensional atomic-arrangement reconstruction from an auger-electron hologram. *Phys. Rev. B* **75** (2007) 085419.
- [25] K. Inaji, F. Matsui, Y. Kato, C. Sakai, T. Narikawa, T. Matsushita, F. Z. Guo and H. Daimon. Circular dichroism of forward focusing peaks and diffraction rings in 2π steradian Si 2p photoelectron pattern. *Appl. Surf. Sci.* **254** (2008) 7549–7552.
- [26] T. Muro, T. Nakamura, T. Matsushita, H. Kimura, T. Nakatani, T. Hirono, T. Kudo, K. Kobayashi, Y. Saitoh, M. Takeuchi, T. Hara, K. Shirasawa and H. Kitamura. Circular dichroism measurement of soft X-ray absorption using helicity modulation of helical undulator radiation. *J. Electron Spectrosc. Relat. Phenom.* **144** (2005) 1101–1103.
- [27] T. Matsushita, F. Matsui, H. Daimon and K. Hayashi. Photoelectron holography with improved image reconstruction. *J. Electron Spectrosc. Relat. Phenom.* **178** (2010) 195–220.

Chapter 7. Summary

In this dissertation, I have developed the applied usage of photoelectron diffraction (PED) for catalyst characterization, holography and diffraction spectroscopy. A number of catalyst surface structure analyses depending on PED have been reported all over the world (1300 hits by searching the words, “catalyst” and “photoelectron diffraction” in Google Scholar) but its usage has been employed alone many other times. I believe that this dissertation contributed to two aspects of novelties in both PED and catalyst studies.

One aspect is that I contributed to develop the experimental and analytical routines for site selective atomic and electronic structure observations. In chapter 2, I succeeded in observing the atomic layer-resolved photoelectron intensity angular distributions (PIADs) and XPS spectra for graphene grown on the SiC substrate. Newly constructed site selective observation considering the photoelectron mean free path length was pithy idea for observing the local interface atomic structures. The reconstruction of holography clarified the primary stacking of graphene on the buffer layer to be a *AB* registry, which has been controversially discussed in graphene study. Through the experience in chapter 2, I hit on the idea for the application of PED to catalyst characterization. In chapter 3, I achieved in separating Ni L-edge X-ray absorption Spectroscopy (XAS) into the local Ni site specific information, while directly corresponds with the relation between the atomic and electronic structures. The separated XAS observed the differences of density of the state dispersion near the Fermi level. The analytical results were reasonable because the site selective XAS calculated by the first principle calculations showed the similar tendencies. This achievement is helpful for determining the local active structure on a catalyst surface. This also contributes for revealing

the catalytic mechanism at an atomic level as well as for improving the development strategy of new catalyst. Thus the advantages using PED in this dissertation were strongly appealed.

The second aspect is that I revealed the surface alloyed structure and its catalytic properties which are crucial issues in Ni_2P study. I demonstrated the replacement of substituted atom with Ni atom in the Ni_2P crystal. Thanks to my experiences and interests, the application of PED for the complex alloyed surface analysis was strongly suggested. In chapter 4, I duplicated the highly active FeNiP bimetallic catalyst by modifying Fe on the single crystalline Ni_2P . The element selective PIAD clarified the replacement of Fe with Ni site in the the Ni_2P crystal. This result has not been obtained by the other characterization methods. I also found that this Fe_2P thin film on the Ni_2P showed a remarkable activity for NO adsorption, while the clean Ni_2P did not show. Through the knowledge in chapter 4, I constructed a new W-modified Ni_2P surface (W- Ni_2P) in chapter 5. This W- Ni_2P surface showed a remarkable activity for NO adsorption, implying the discovery of an unprecedented highly active surface. On both alloyed surfaces, the amount of NO adsorbate was similar although the surface Fe was fifth times as superior than that of W. This indicates that the adsorption probability of W is fifth times as large than that of Fe. Thus our developed W- Ni_2P is expected to have a high catalytic activity. However, one interest is occurred at the same time. In this thesis, each alloying preparation methods and conditions are different, especially depositing temperature. On the W- Ni_2P surface, the deposition was done by approaching the high temperature W filament above the Ni_2P surface. The substitution may be led by high temperature due to the irradiation from W filament nearby. In contrast, the replacement of Fe with Ni atom at room temperature seems to be difficult because the energetic origin breaking the Ni-P bonding is unknown. The epitaxial growth of Fe_2P by supplying phosphorus atoms from the

bulk is suggested. Each crystal growth is open question.

I got further into the future usage of microscopic PED using the polycrystalline Ni_2P surface because the model catalyst study is frequently faced with a dilemma for the difference of the catalytic properties between the single crystalline and real catalyst surfaces. I found a new structural phase of cubic CaF_2 -type structure in the polycrystalline Ni_2P surface. I also revealed the catalytic activity at each crystal grain. Because PED is an only analysis method for revealing the relation between the crystal structure and orientation and the catalytic activity with element selectivity, this analytical achievement is one of the legitimate evolution in PED study. The selective adsorption of $\text{CH}_3\text{-S}$ was confirmed at Ni-rich position, indicating that the exposure of Ni atom may be a key for appearing the high HDS activity. The NO adsorption was not observed on single and polycrystalline surfaces in this study. This implies that both surfaces have the similar chemical properties. This study is located at between the real and model catalysts. The further discussion such as the detailed reaction conditions and the surface phase difference must be necessary.

The finding the common point in the model and real catalysts will be my life work. The analytical strategy focusing on the common point should be clarified using model catalyst at an atomic level.

Accomplishments

1 Papers

1. “Local atomic configuration of graphene, buffer layer and precursor layer on SiC(0001) by photoelectron holography”

H. Matsui, F. Matsui, N. Maejima, T. Matsushita, T. Okamoto, A. N. Hattori, Y. Sano, K. Yamauchi, and H. Daimon

Submitted to Phys. Rev. B (November 2012)

2. “Disentanglement of site selective X-ray absorption spectra of catalytic Ni₂P surface by photoelectron diffraction spectroscopy”

H. Matsui, F. Matsui, N. Maejima, T. Matsushita, H. Ariga, K. Asakura, and H. Daimon

in preparation

3. “Surface atomic structure and the catalytic property of Fe-Ni₂P surface alloy by photoelectron diffraction”

H. Matsui, F. Matsui, N. Maejima, T. Matsushita, H. Ariga, K. Asakura, and H. Daimon

in preparation

4. “Atomic structure and catalytic properties of W-Ni₂P surface alloy by photoelectron diffraction and spectroscopy”

H. Matsui, F. Matsui, N. Maejima, T. Matsushita, H. Ariga, K. Asakura, and H. Daimon

e-J. Surf. Sci. Nanotech. Vol. 12 (2014) 53-56.

5. “Atomic structure analysis of catalytic poly-crystalline Ni₂P surface by microscopic photoelectron diffraction”

H. Matsui, F. Matsui, N. Maejima, T. Matsushita, H. Ariga, K. Asakura, and H. Daimon

in preparation

2 Honors and Awards

1. Catalysis on catalyst symposium 2012

Best presentation award

“The local atomic and electronic structure analyses of $\text{Ni}_2\text{P}(10\bar{1}0)$ catalytic surface by photoelectron diffraction spectroscopy”

(2012 December)

2. The 5th SPring-8 Budding Researchers Award

“The atomic and electronic structure of $\text{Ni}_2\text{P}(10\bar{1}0)$ and related alloy surface and catalytic activity”

(2012 November)

3. International workshop on 3D atomic imaging at nano-scale active sites in materials

Best Poster Award

“Layer-resolved atomic and electronic structure analysis of graphene on 4H-SiC(0001) by photoelectron diffraction spectroscopy”

(2012 August)

4. The 108th Catalysis Society of Japan meeting

Best Presentation Award

“Local atomic and electronic structure analysis of $\text{Ni}_2\text{P}(10\bar{1}0)$ surface by two-dimensional photoelectron diffraction spectroscopy.”

(2011 September)

5. The 9th SPring-8 Users Society Microscopic-Nano Materials Science workshop

Best Poster Award

“Atomic layer resolved structure analysis of single-layer graphene on 4H-SiC(0001)”

(2010 December)

6. GIST-NAIST-NCTU International Exchange Program 2010

1st grade Presentation Award

“Layer-resolved structure analysis of graphene on 4H-SiC(0001)”

(2010 November)

7. The 19th Catalysis Society of Japan characterization lecture

West Japan executive head Award

“Site selective structure analysis by two-dimensional photoelectron diffraction spectroscopy”

(2009 November)

Acknowledgements

本研究を遂行するにあたりご指導いただいた、奈良先端科学技術大学院大学、物質創成科学研究科、凝縮系物性学研究室のスタッフの皆様に感謝申し上げます。大門寛教授には数々の研究発表、実験機会を与えていただき、私の博士課程は大変充実したものとなりました。特に国際会議には毎年のように挑戦させていただき、世界最先端の研究経験を積ませていただけたと感じています。やり残した研究課題や未熟な知識もあり、博士課程の学生として至らぬ点多々あったかと思いますが、本研究室を卒業できることに誇りを持っています。

グリーンナノシステム研究室の松井文彦准教授には、修士課程から併せて5年間、公私にわたり大変お世話になりました。思えば、自分のやってきたこと・知識は、松井先生から授けられたものばかりで、この5年間で先生から独り立ちできたとは言えませんが、この深遠なる研究の世界に引き入れ、科学者の卵として成長させて下さったことに深く感謝いたします。先生の勤勉で真面目なお姿は自分と対極にあり、背中で語る姿勢にはいつも励まされ、同時に、自分の不甲斐なさには何度も嫌気が差しました。それでも、地道に一つ一つの課題を解決していくことで、学会発表や論文投稿という形で成果を形にすることができ、言葉に代えがたい喜びを体験できました。また、2人の子供の父親として家庭を支え、獅子奮迅されるお姿には、自身の人生設計においても大きく影響を受け、結婚から出産に至るまで踏み出す勇気を与えていただきました。先生の自分を強く律し、他の模範とされる姿に強く共感しています。家庭においても研究においても立派な人間になれるよう、今後も努力していきたいと思えます。

凝縮系物性学研究室の服部賢准教授には、隔週で行われるラボミーティング、年2回の中間審査のほかに、適時、有益な就職・研究情報を与えていただき大変感謝しております。先生の的確なアドバイスを受け、本論文は問題点が明瞭になりました。また、先生の純粋な興

味から研究に向かわれる姿に感銘を受け、研究者としてあるべき姿を見せていただいたように思います。さらに、子育てにも積極的に参加されるお姿に、人生論的な教訓も多々授けていただいたと感じています。

凝縮系物性学研究室の武田（西野）さくら助教には、居室が同じだったこともあり、研究室の居心地のよい雰囲気作りだけでなく、時節繰り出される理系トークに花を咲かせていただき、大変楽しい研究生生活を送らせていただきました。また母親として、子育てと研究を両立して高いクオリティの生活を送られるお姿には、自分の苦労はまだまだと感ずることもあり、これから訪れるであろう人生の障害にも立ち向かって行ける勇気と心の余裕をいただきました。

副指導を担当していただいた有機固体素子科学研究室の中村雅一特任教授には、大学院生活の途中からですが、年2回の中間審査で大変お世話になりました。表面科学を専攻されていたことがきっかけでご指導承ることになりましたが、先生の幅広い知識と、研究室外からいただけるアドバイスはいつもの的確であり、自身の研究を見直すきっかけを与えて下さいました。また、研究生生活を通して多くの分野に挑戦されるお姿は自分にとって新鮮であり、就活活動の際には幅広い視野で人生設計を考えることができました。

スーパーバイザーを担当していただいた環境適応物質学研究室の余語克則客員教授には、大学院生活の途中ですが、年2回の中間審査で大変お世話になりました。自分の興味が触媒化学ということで、触媒研究のスペシャリストにご意見承りたくお願いしましたが、ふたを開けてみると大学時代の元指導教官と懇意で、審査の際にはいつも近い距離でお話していただきました。また、自分の研究分野の性質上、触媒研究を目指しているのにもかかわらず関連が見い出せず苦しんでいた際、触媒分野の研究者から見たご意見をいただけ、先生にご指導いただけことに大変満足しております。

共同研究をしていただいたJASRI(SPring-8)の松下智裕博士には、実験の遂行から解析ソ

フトの提供に至るまで大変ご尽力いただきました。お忙しい中、毎期のマシンタイムには必ずお顔を出してアドバイス・議論していただき、技術面だけでなく精神的にも支えていただきました。また、論文投稿の際には懇切丁寧な指導をしていただきました。博士のご尽力なしに本研究は達成されませんでした。この研究領域で研究ができてよかったと本当に思える5年間でした。

共同研究をしていただいた北海道大学、触媒化学研究センターの朝倉清高教授には、Ni₂Pの研究を始めてから、実験計画の立案から研究結果の議論に至るまで、大変お世話になりました。先生の進められる研究分野は自分の目標であることから、先生のこれまでのキャリアとご専門、人脈は理想とする研究者像です。当初、松井先生よりご紹介いただき始まった共同研究ですが、D1の時には先生の研究室に滞在して研究を進めさせていただいたり、解析結果を徹底的に議論していただき、先生のおかげで本論文が完成したと言っても過言ではありません。今後も先生と近い研究領域で活動していきたいと考えておりますので、よろしくお願いたします。

共同研究をしていただいた北海道大学、触媒化学研究センターの有賀寛子助教には、SPring-8のマシンタイムにご参加いただけただけでなく、試料計算結果の提供、北大での滞在実験に至るまで、懇切丁寧にご指導いただきました。先生に連絡をすると、いつも海外や放射光施設で実験をされており、その多忙なお仕事をこなされる技量と体力には常に驚かされました。

凝縮系物性学研究室の諸先輩方、後輩の皆さんには公私に至るまで、私の大学院生活を支えていただき、ありがとうございました。皆さんの作っていただいた研究室の雰囲気は大変居心地がよく、充実した大学院生活を送ることができました。大学院入学時は右も左も分からなかった私ですが、研究における基礎知識だけでなく、社会における共同生活を学ばせていただきました。特に同期の前島尚行君とは、同じSPring-8班で苦楽を共にできたことを誇りに思います。2人で一人前と言われ、お互い得意、不得意がありましたが、切磋琢磨し、仲

良く協力して研究生生活を送れたことは人生の宝物です。また、先輩の吉村真史博士，後藤健太郎博士，西嘉山徳之さん，同期の土橋剛士君，後輩の北川哲君，堀江理恵さん，藤田將喜君，石井良君，安田馨君，大田拓也君，橋本由介君，西川弘晃君，皆さんに助けられ，苦楽を共にして，本研究は実施されました。

私の大切な家族とお礼申し上げます。妻は私のことを最優先に，自らの人生を捧げてくれました。昼のお弁当と家に帰ってからのくつろぎは活力の源であり，楽しいことも辛いことも共有して，精神的にも肉体的にも安定した生活を送れたように思います。また，私たちの間に大切な娘を設けることができたのは人生最大の喜びであり，今後の私を支えてくれると思います。大学院生活の中でこれほど充実した生活を送ることができたことは，全て家族の協力があったためです。両親，妹，祖父母，義母，義兄，義姉には博士課程への進学を快諾いただき，また自身の進路選択に賛同いただけたことに深く感謝しています。就職がなかなか決まらず，皆さんには本当にご心配をかけましたが，今後研究者として成功できるよう邁進しますので，今後もよろしく願いいたします。

最後に，本研究は日本学術振興会特別研究員 (DC1, 課題番号：11J09374) のご支援のもと遂行されました。また SPring-8 での実験は，萌芽的研究支援 (2011B1689, 2012A1553, 2012B1680, 2013A1606) のもと行われました。ここに深く御礼申し上げます。